ՀՀ ԿՐԹՈՒԹՅԱՆ ԵՎ ԳԻՏՈՒԹՅԱՆ ՆԱԽԱՐԱՐՈՒԹՅՈՒՆ
ԵՐԵՎԱՆԻ ՊԵՏԱԿԱՆ ՀԱՄԱԼՍԱՐԱՆ

Վարդան Արայի Բաղմանյան

ՌԱԴԻՈԳԱԼԱԿՏԻԿԱՆԵՐԻ ՈՒՍՈՒՄՆԱՍԻՐՈՒԹՅՈՒՆԸ ՌԵՆՏԳԵՆՅԱՆ և ԲԱՐՁՐ ԷՆԵՐԳԻԱՆԵՐԻ γ ՏԻՐՈՒՅԹՆԵՐՈՒՄ. ՏՎՅԱԼՆԵՐԻ ՄՇԱԿՈՒՄ և ՄՈԴԵԼԱՎՈՐՈՒՄ

ԱՏԵՆԱԽՈՍՈՒԹՅՈՒՆ

Ա.03.02 - «Աստղաֆիզիկա» մասնագիտությամբ
ֆիզիկամաթեմատիկական գիտությունների
թեկնածուի գիտական աստիճանի համար

Գիտական ղեկավար՝
ֆ.մ.գ.դ., պրոֆեսոր Յու. Լ. Վարդանյան

Երևան-2018

YEREVAN STATE UNIVERSITY
FACULTY OF RADIOPHYSICS

Vardan Ara Baghmanyan

THE STUDY OF RADIOGALAXIES IN X-RAY AND γ-RAY BANDS: DATA ANALYSIS AND MODELING

DOCTORAL THESIS

A thesis submitted in fulfillment of the requirements
for the degree of Doctor of Philosophy
in
specialization 01.03.02 – "Astrophysics"

Supervisor:
Prof. Yura L. Vardanyan

Yerevan–2018

Contents

INTRODUCTION

The recent progress of technical capabilities of the ground- and satellite-based observatories have made it possible to investigate the physical processes taking place in both Galactic and extragalactic sources studying their emission in a large frequency range (multiwavelength astrophysics). Due to the large number of currently operating telescopes and their mostly publicly available data, multiwavelength astrophysics has become one of the fastest developing and most perspective fields of astrophysics.

According to broadband observations, large multiply sources of different classes have non-thermal spectra ranging from radio to high energy (HE; > 100 MeV) and very high energy (VHE; > 100 GeV) bands. These include Galactic sources such as pulsars, supernova remnants, pulsar wind nebulae and binary systems and extragalactic sources, for example Gamma-Ray Bursts (GRBs) and Active Galactic Nuclei (AGNs). From extragalactic sources GRBs are short-lived bursts of γ-ray photons, which last from a few milliseconds to several minutes, while AGNs constantly emit for a very long time, making them one of the most powerful long-lived objects of the Universe. AGNs are strong emitters in all observed energy bands being among the most studied sources. The study of AGNs quickly developed since their discovery, but tremendous progress was achieved after the recent lunch of several telescopes operating in X-ray and HE γ-ray bands, such as Swift, NuSTAR, Chandra and Fermi-LAT.

A wide range of objects is subsumed under the name of AGNs in common have a strong non-thermal emission from the core of a galaxy: although, they are characterized by different optical and radio spectral properties. The main structure of these sources are shown in Fig. 1. The central supermassive black hole is surrounded by an accretion disk, which for all AGN types emits in the optical and UV energies. This thermal radiation photoionizes the gas around the black hole and as a result broad and narrow emission lines are observed, where the broad lines are coming from a region with a size of $\sim 10^3$ Schwarzschild radius around the black hole and the narrow lines are produced from a much more extended region. The strong infrared emission of all AGNs argues for the presence of obscuring matter (torus), which is concentrated on the plane in which the

accretion occurs. The accretion disk produces highly collimated and fast outflows (jets) in opposite directions, which provide the broadband non-thermal emission and has been observed in almost all powerful radio-loud AGNs (roughly $15-20\%$ of AGNs are radio-loud, meaning they have ratios of radio (5 GHz) to optical (B-band) fluxes > 10).

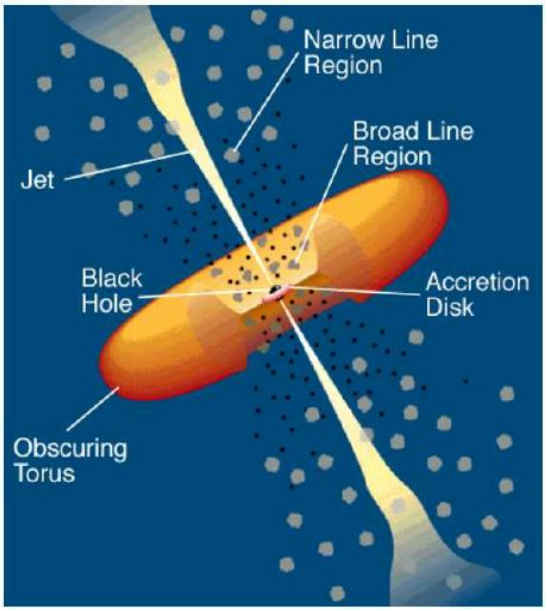

Figure 1: The main structure of AGNs [1].

The motion of the plasma in these jets can reach from middle relativistic to high relativistic apparent velocities and the emission from them has been observed across all electromagnetic spectrum: from radio to HE γ-ray bands. The observations at low energy band allowed the investigation of the jet in sub-structures and sub-parsec scales, which showed internal structures, such as knots and hot spots.

The observations at HE band (X- and γ-ray) are equally important, since the large fraction of the jet energy is released in these energy bands. Up to now, it is uncertain how the jets are formed, accelerated and confined. For example, freely expanding jets probably should have large opening angles while the observations show narrow structures, requiring confinement and collimation. The new theories should address and explain the collimation and propagation of the jets using the recent results from the multiwavelength observations.

The main unification scheme of different AGNs classes offered by [1] relies on the viewing direction or the inclination angle of the jets. For example, when the inclination angle is large to the observer, the radio loud AGN is a radiogalaxy whereas AGN with closely aligned jet is

appeared as blazar. Some other divisions of AGNs are possible in the case of jet intermediate angles, such as Compact Steep Spectrum (CSS) radio sources or Steep Spectrum Radio Quasars (SSRQ). Another important class of AGNs interesting for γ-ray observations is Narrow line Seyfert 1 (NLSy1) galaxies. These sources have only recently been detected in γ-ray band, but due to interesting structures and detected strong γ-ray emission these sources are important for studies. Also, the detection of different components (knots, hot spots, lobes, etc.) within the jets of AGNs in different bands provides a new chance to investigate the physical processes occurring in these sources.

According to the unification theories, AGNs are the same objects, but viewed from different directions. This implies that the studies of radiogalaxies, blazars or seyferts can help to understand the properties of AGNs in general. Due to the large number of currently operating telescopes, large numbers of AGNs have been observed in different energy bands opening new perspectives for their studies. For example, the theoretical modeling of AGNs broadband spectra obtained from the combination of data observed in different energy bands allows the understanding of the main acceleration and emission processes operating in AGNs. On the other hand, the studies of large numbers of the same class sources (e.g., BL Lacs, FSRQs, radio galaxies etc.) allow to find common behaviors between them, which are crucial for understanding the general physical processes in AGNs (e.g., different component formation, their evolution, etc.). Unlike, the observations in the low energy bands (radio-X-ray), the data in the high energy γ-ray band were available only after the lunch of Fermi-LAT in 2008. Thus, their analyses and interpretations are among the most actual topics in astrophysics.

In the γ-ray band after initial 4-years of Fermi LAT observations, more than 1000 AGNs of different types were detected above 100 MeV. Most of these sources were blazars although small numbers of non-blazar AGNs also were detected. This thesis is devoted to study the properties of AGNs, which show no-blazar like emission properties and being detected in the high energy γ-ray band. In total there are 27 non-blazar AGNs detected by Fermi LAT including Fanaroff-Riley Class I (FR-I), II (FR-II) and SSRQ (CSS) types. Studying the spectral properties of these sources and comparing with similar parameters of blazars

provides a chance to understand the AGNs features in the γ-ray band. In the current study, the γ-ray data observed during 2008-2015 are analyzed with corresponding spectral properties (flux, photon index, etc.) estimation, which allows to find common properties of different types of non-blazar AGNs. Then, possible spectral changes in $(0.1-100)$ GeV band are investigated by spectral analyses. In order to identify the γ-ray emitting sites, detailed temporal analyses in long and short time scales are performed. For example, if the variability can be rejected at high significance, this might be an indication that high energy γ-rays are produced from extended components (e.g., knots, lobes, etc.). Next, having the data of UV/optical, X-ray and γ-ray bands the origin of emission from some sources are investigated by estimating the model free parameters using statistical methods. Also the γ-ray emission characteristics of recently detected 5 NLSy1s are discussed, which facilitate their jet studies as their γ-ray spectra, flux, luminosity, etc. Then these results are compared with those of radio galaxies and blazars (aligned and not aligned cases). These studies are crucial for the study of non-blazar AGNs properties in the γ-ray band using the most recent available data.

The goals of the thesis are:

- Analyze Fermi-LAT data accumulated from the observations of 27 non-blazars AGNs during 2008-2015, using the binned likelihood method
- Estimate the γ-ray flux and photon index, investigate the spectra above several GeVs, search possible deviation from power-law model.
- Study the flux variability both in short and long periods using the light curves generated with normal and adaptively binned time intervals.
- Study the HE γ-ray emission from the brightest radiogalaxy in MeV/GeV band NGC 1275. Investigate flux evolution in time, identify flaring periods and estimate flux variability time scale.
- Estimate the γ-ray luminosity, photon index and flux of NLSy1 galaxies, study the acceleration and radiation processes of the electrons in their jet by modeling their multifrequency SEDs.

- Study the radiation processes in the jet of PKS 0625-35, which is one of the radiogalaxies detected in the VHE γ-ray band. Estimate the main parameters describing the jet, such as luminosity, magnetic field, total power and etc.

Scientific novelty:

- The results obtained from the Fermi-LAT data analysis accumulated during the 7 years of the observations of 26 non-blazar AGNs it was shown, that the measured faintest flux is of the order of a few times $10^{-9}\, photon\, cm^{-2}\, s^{-1}$, while the flux from bright sources exceeds $10^{-7}\, photon\, cm^{-2}\, s^{-1}$. In the $\Gamma - \mathrm{L}_{\gamma}$ plane, the luminosities of non-blazar AGNs occupy the area of $\mathrm{L}_{\gamma} = (1.12 \times 10^{41} - 7.85 \times 10^{46})\ \mathrm{erg\ s^{-1}}$ and the γ-ray photon indexes change within $1.84 - 2.86$ range.
- We showed, the γ-ray spectra of most of the sources studied here are described significantly better by a PL, while the spectra of NGC 6251, SBS 0846+513 and PMN J0948+0022 are better modeled with log-parabola and the curvature in the γ-ray spectrum of NGC 1275 can be better described using power-law with eexponential cut-off (β free). There is a hint of possible cut-off in the spectra of 3C 380, PKS 0625-35 and 1H 0323+342, though the current data does not allow us to reject the power-law model.
- Using the γ-ray light curves generated with an adaptive binning method we identified rapid and strong variability of NGC 1275, 3C 120 and three NLSy1 1H 0323+342, SBS 0846+513 and PMN J0948+0022 galaxies accompanied by changing of photon index. The variability was also detected from 3C 111, Cen A core, 3C 207, 3C 275.1, 3C 380, 4C+39.23B, PKS 1502+036 and PKS 2004-447 sources, but within longer times scales.
- Studying the HE γ-ray emission of NGC 1275, we found that source displayed prominent flaring activities in October 2015 and December 2016/January 2017 with the 3-hour peak flux above 100 MeV of $(3.48 \pm 0.87) \times 10^{-6}\, photon\, cm^{-2}\, s^{-1}$ observed on 2016 December 31 corresponding to an apparent isotropic γ-ray luminosity of $L_{\gamma} \simeq 3.84 \times 10^{45}\, erg\, s^{-1}$. The shortest γ-ray variability time scale of this source was 1.21 ± 0.22 hrs, which is unusual for radio galaxies. The observed

hour-scale variability suggests that the HE γ-ray emission is produced in a very compact emission region with $R_\gamma \leq 5.22 \times 10^{14}\,(\delta/4)\,cm$, and perhaps it is produced in a sub-parsec scale of the jet.

- Observing PKS 0625-35 radiogalaxy in optical/UV, X-ray and γ-ray bands using the data gathered with Swift UVOT/XRT ևFermi-LAT instrument during 8.7 years, we found out, the one-zone synchrotron/SSC model can reproduce the observed multiwavelength SED. Assuming the electrons are accelerated up to $E_{max} = 50\,TeV$ with a power-law index of $\alpha = 2.63 - 2.76$, the observed spectrum above TeV energies can be explained by IC scattering of synchrotron photons on the electron population producing the radio-to-X-ray emission in the jet.

Basic statements of the thesis:

1. The HE γ-ray emission properties (photon index, flux, luminosity) of non-blazar AGNs Fermi-LAT data accumulated during 7 years of observation are investigated.
2. It is shown that, in the case of NGC 1275, NGC 6251, SBS 0846+513 and PMN J0948+0022 spectra the power-law modeling can be rejected and are statically better described by log-parabola or power-law with exponential cut-off models.
3. Short time variability of γ-ray emission for NGC 1275, 1H 0323+342, SBS 0846+513 and PMN J0948+0022 sources are detected, while the variability of 3C 111, Cen A core, 3C 207, 3C 275.1, 3C 380, 4C+39.23B, PKS 1502+036 and PKS 2004-447 is within longer periods.
4. The study of γ-ray flaring periods of NGC 1275 showed, that the flux changes rapidly within 1.21 ± 0.22 hrs, when the γ-ray flux increased up to $(3.48 \pm 0.87) \times 10^{-6}\,photon\,cm^{-2}\,s^{-1}$.
5. It is shown that the broadband emission $(10^7 - 10^{27})$ Hz of PKS 0625-35 radiogalaxy can be explained within synchrotron/synchrotron self Compton scenario if the maximum energy of accelerated electrons reaches up to 50 TeV.
6. Studying the γ-ray emission from three NLSy1 sources (1H 0323+342, SBS 0846+513 and PMN J0948+0022), it is shown that the emission is characterized with short time variation implying the emission is produced within the compact regions of

the jet. The broadband modeling of the emission from these sources showed that HE γ-ray emission can be well explained by IC scattering of synchrotron photons.

The practical value:

- The results obtained from the γ-ray data analysis of a large number of non-blazar AGNs can help to understand the acceleration and radiation processes in their jets.
- NLSy1 galaxies were only recently classified as γ-ray emitters, therefore study the properties of γ-ray mission from these sources is important to understanding the physical processes in their jets responsible for broadband emission from very compact region of the jet as inferred from the variability in short time scales.
- The results obtained from the multiwavelength studies of NGC 1275 and PKS 0625-35 radiogalaxies can be used for investigation of the acceleration and the emission processes in the inner jets of radiogalaxies.

The thesis is structures as follows:

In introduction the novelty and the importance of the problems considered in the thesis are briefly discussed, presenting the previous results and emphasizing the main goals.

In chapter 1 the unification model of AGNs classification is briefly described, mainly considering the broadband properties of radiogalaxies, NLSy1 galaxies, SSRQ and CSS quasars. Also, the main radiation processes (synchrotron and inverse Compton emission), which are responsible for low and high energy emissions of AGNs, are presented. Then, the description of Swift telescopes and Fermi-LAT telescope are presented describing their technical parameters, observational methods, etc. Also, the detailed analysis of optical/UV, X-ray and Fermi-LAT data are described including multifrequency light curve and SED preparation.

In Chapter 2 the main characteristics of γ-ray emission from 27 non-blazar AGNs included in the third Fermi-LAT AGNs catalogue are investigated. The data of eleven FRI, ten FRII radiogalaxies, six SSRQs and five NLSy1s are analyzed using the new PASS 8 event selection and instrument response function. Possible spectral changes above GeV energies are

investigated with a detailed spectral analysis. The light curves generated with normal and adaptive time bins are used to study the γ-ray flux variability.

In Chapter 3 the γ-ray emission from the brightest radio galaxies in the MeV/GeV band-NGC 1275 is investigated. Using 8.7-year duration light curve of Fermi-LAT prepared with normal and adaptive binned periods, the flaring periods are identified. The detailed temporal and spectral analyses are performed for these active periods creating SEDs during and around the flares are prepared, then corresponding emission processes are discussed.

In Chapter 4 the γ-ray observation of PKS 0625-35 radiogalaxy using the Fermi-LAT data accumulated during 2008-2017 are presented. Constructing the multiwavelength light curves in the γ-ray, X-ray and UV/optical bands identifying active and steady states of X-ray radiation. Then the corresponding SEDs are prepared and modeled using Markov Monte Carlo Chain methods estimating main jet parameters (luminosity, magnetic field, etc.).

In Chapter 5 the multiwavelength emission properties of most variable NLSy1s (1H 0323+342, SBS 0846+513 and PMN J0948+0022) are discussed, using the γ-ray data from the last 8.8 years Fermi-LAT observations as well as available Swift (UVOT/XRT) data. The flares in the γ-ray band are identified and minimum variability periods are estimated. One zone synchrotron/synchrotron self-Compton leptonic radiation mechanism is applied to model the multiwavelength SEDs in quiescent and flaring states.

In Conclusion the main results obtained in the thesis are presented.

Chapter 1

1. MULTIFREQUENCY OBSERVATIONS OF AGNs AND DATA ANALYSES

1.1 The classification of AGNs: The Unified Model

The unified model of AGNs proposed by [1] is based on the optical/UV and radio properties, which connects FR-I radiogalaxies with BL Lack blazars and FR-II radiogalaxies with FSRQ quasars. Even if this is not a unique model, it can describe several important properties observed in AGNs. Mainly, AGNs classification is explained by different viewing angle of the relativistic jet, existence (or absence) of dusty structure around the accretion disc, which absorbs the broad line emission, etc. (see Fig. 1.1). Below, some properties of FR-I and FR-II radiogalaxies, SSRQs, CSSs and the γ-NLSy1s non-blazar AGNs classes are described.

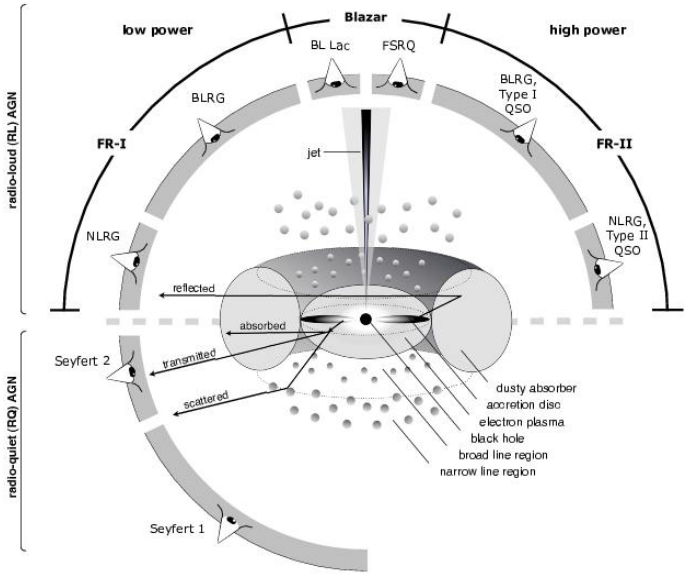

Figure 1.1: Sketch showing the structure and the main ideas of the AGNs unfied model. Credit: [2].

1.1.1 FR-I and FR-II Radiogalaxies

The radio galaxies can be grouped in two main categories based on their radio morphology and observed radio luminosity [3]. In particular, the radiation of FRIs is mainly produced from the core and gets fainter farther from it, while in the case of FR IIs the farther part of

the jet is brighter. The difference of these two sub-classes can be seen on Figure 1.2, where the sources M 84 and 3C 175 are shown. These classes are also divided by their luminosities: namely, the radio luminosity of FR-I at 178 MHz is $< 10^{41}\ erg\ s^{-1}$ while in the case of FR-II class it is larger than the mentioned limit. In the AGN unification theories FRI and FRII sources are the parent populations of BL Lacs and FSRQs [1].

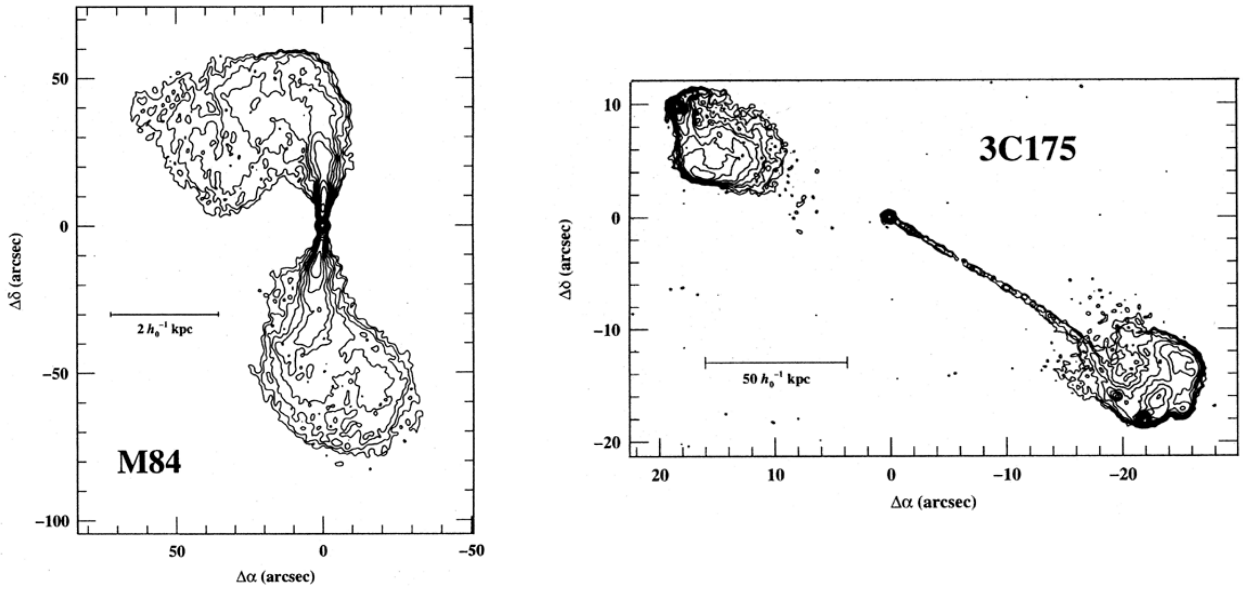

Figure 1.2: Eaxmples of the radio maps of M84 (FR I) [4] and 3C 175 (FR II) [5] galaxies obtained with Very long-baseline interferometry (VLA) at 4.9 GHz.

1.1.2 SSRQ and CSSs Quasars

CSS radio sources are characterized by the steep spectrum ($\alpha \gtrsim 0.5$, where $S \sim \nu^{-\alpha}$) in radio band and have (1-20) kpc compact scales not exceeding the size of the host galaxy [6]. The radio morphology of these sources are similar to FR II radiogalaxies, but within smaller scales. Based on the symmetric radio structure in the both side of the core and the scales, this class was divided into two sub-classes, which are compact symmetric objects (CSOs, [7]) if the physical extension is <1 kpc and medium-sized symmetric objects (MSO, [8]) for the sources with up to (15-20) kpc scale. The recent studies in radio and optical bands showed, that these sources are enough young ($\lesssim 10^5$ yr), which means that they are observed in the initial stage of their evolution [9]. SSRQs usually have lobe dominated radio emission with larger inclination angle of the jet compared to the blazars and consequently, the beaming effect of the radiation is weaker [10]. In particular, it is not clear whether the variation of

the flux is conditioned by thermal emission from the accretion disk like in the case of radio quite quasars or the variation is due to the non-thermal emission. For example, as mentioned in [11], the optical variability is most likely due to the thermal emission of the accretion disk, although the non-thermal emission from the jet as a possible reason for the variability can't be excluded. Similar to radiogalaxies, SSRQs also have high luminosities of the jets, and radiation from lobes and hot spots have been also detected in the large distances.

1.1.3 The γ − NLSy1 Galaxies

The classification of γ-NLSy1 galaxies as a new class first time was performed by [12] based on the Balmer lines widths and [OIII] forbidden lines: namely, their full width of half-maximum (FWHM) of the broad Hβ line is $< 2000\ km\ s^{-1}$, the emission of [O III] is weak([O III]/λ5007/Hβ <3), and compared to normal seyferts they also have strong Feii lines [13] and soft X-ray spectra [14], which exhibits short time variations of the flux [15]. The γ-ray emitting NLSy1s are radio loud (RL) galaxies (generally only $5-7\%$ of NLSy1s are RL) with relatively low black hole mass of $\sim(10^6-10^8)\ M_\odot$ [16] and powerful relativistic parsec scale jets resolved in VLBI images. Recently, also several NLSy1s were detected in the γ-ray band by Fermi-LAT [16, 17]. The accretion powers of these sources are comparable or above the Eddington limit [18]. The multifrequency observation showed similarities between SEDs of these sources and FSRQs [19], although there are some differencies. In particluar, the host galaxies of NLSy1s are most likely spiral galaxies (e.g.,[20]), while blazars are hosted by elliptical galaxies and compared to NLSy1s they have heavier black holes [1].

1.2 The Main Processes Responsible for AGNs Emission

1.2.1 Thermal Radiation

The thermal emission observed from the AGNs is black body emission. This radiation is described by Planck law, where $B_\nu(T)$ intensity is given by:

$$B_\nu(T) = \frac{2h\nu^3}{c^2}\frac{1}{e^{\frac{h\nu}{kT}}-1}, \tag{1.1}$$

where $h = 4.135 \times 10^{-15}\ ev\ s$ is the Planck constant, T is the temperature of the system, $k = 8.617 \times 10^{-5} ev\ K^{-1}$ is the Boltzmann constant and ν denotes the frequency of the radiation. The dependence of the intensity on the temperature is shown in Figure 1.2.

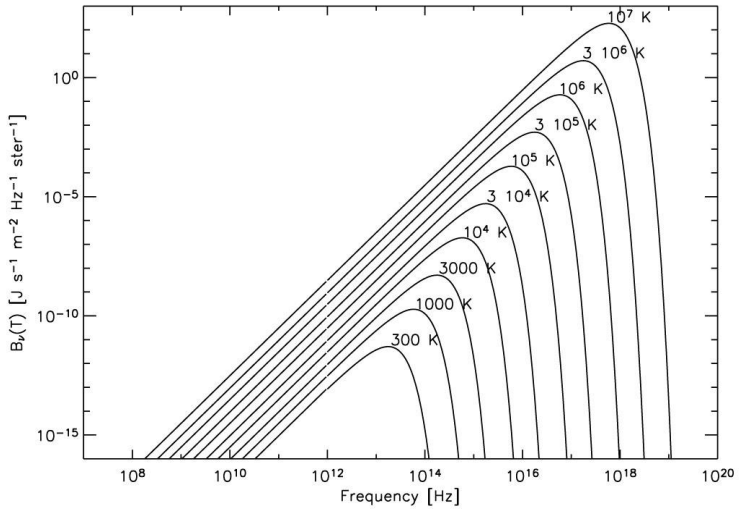

Figure 1.3: Black body radiation for different equilibrium temperatures, showing shift of the intensity into higher energies due to the increase of the temperature.

Thermal emission from AGNs is observed from the accretion disc, which peaks at optical/ultraviolet or soft X-ray bands.

1.2.2 Synchrotron Radiation

When a charged particle(s) moves in the curved paths due to the Lorentz force produced by inhomogeneous magnetic fields, it emits photons by synchrotron emission. When the magnetic field dominates over the electric field, the Lorentz force on the charged particle is

$$F_L = q \times \beta \times B, \tag{1.2}$$

where q is the particle charge, $\beta = v/c$ denotes the particle velocity and B is the magnetic field. It can be shown that the synchrotron power produced by a single electron obtained from the generalized Larmor formula is expressed as

$$P_s(\theta) = 2\sigma_T \gamma^2 \beta^2 c U_B \sin^{-2}\theta, \tag{1.3}$$

here $\sigma_T \approx 6.65 \times 10^{-25}\ cm^2$ is the Thomson cross section, θ is the angle between magnetic field line and the velocity vector called pitch angle and $U_B = B^2/8\pi$ is magnetic field energy density.

In the case of isotropically distributed pitch angles

$$P_s = (4/3)\sigma_T \gamma^2 \beta^2 c U_B, \ \ (\sin^2\theta = 2/3). \tag{1.4}$$

Using this expression, we get the synchrotron cooling time for electrons. In the case of $\beta \approx 1$ it has the following form:

$$t_{syn} = \frac{E}{P_s} = \frac{3\gamma m_e c}{4\sigma_T \gamma^2 U_B} \tag{1.5}$$

The electron radiation power per unit frequency, when the pitch angle and Lorentz factor are given, is given by [21]:

$$\frac{dN_\gamma}{dE_\gamma dt} = \frac{\sqrt{3}e^3 B}{m_e c^2 h E_\gamma} F\left(\frac{E_\gamma}{E_c}\right). \tag{1.6}$$

Here

$$F(x) = x\int_x^\infty K_{5/3}(\tau)\, d\tau, \tag{1.7}$$

where $K_{5/3}$ is the modified Bessel function and E_c is the electron characteristic energy

$$E_c = \frac{3ehB}{4\pi m_e c}\gamma^2. \tag{1.8}$$

In the astrophysical sources the synchrotron emission is produced from the population of electrons, which usually have a spectral energy distribution (SED) of $N_e(\gamma) = N_0\gamma^{-p}$. In general, the flux of synchrotron emission can be calculated by integrating the SED for all electron energies. It is given by following formula [22]:

$$f_\epsilon^{syn} = \frac{\sqrt{3}\delta_D^4 \epsilon' e^3 B}{4\pi h d_L^2}\int_1^\infty d\gamma' N_e'(\gamma') F\,(x), \tag{1.9}$$

where $\epsilon' = h\nu_s'/mc^2$ is the dimensionless emitted photon energy and d_L is source distance.

1.2.3 Inverse Compton (IC) Scattering

Inverse Compton (IC) scattering is the main mechanism responsible for the emission of the high energy component of AGNs. The electron energy lose rate of IC scattering in the Thomson regime is obtained by subtracting the initial radiation power from the scattered:

$$P_{IC} = \frac{4}{3}\sigma_T \gamma^2 \beta^2 c U_{rad}, \tag{1.10}$$

where U_{rad} is the photon field density before the scattering. Therefore, the cooling time of a single electron can be written as

$$t_{IC} = \frac{E}{P_{IC}} = \frac{3\gamma m_e c}{4\sigma_T \gamma^2 \beta^2 U_r} \tag{1.11}$$

The differential spectrum of IC scattering in the lab frame obtained by [23] is given by following equation:

$$\frac{dN_{\gamma,\epsilon}}{dt d\epsilon_s} = \frac{\pi r_0^2 c}{2\gamma^4} \frac{n(\epsilon) d\epsilon}{\epsilon^2} \left(2\epsilon_s ln \frac{\epsilon_s}{4\gamma^2 \epsilon} + \epsilon + 4\gamma^2 \epsilon - \frac{\epsilon_s^2}{2\gamma^2 \epsilon} \right) \tag{1.12}$$

where, $r_0 = 2.81794 \times 10^{-17}$ cm is classical electron radius, ϵ and ϵ_s are energies of interacting and scattered photons, respectively and $n(\epsilon)$ represents the photon density.

1.2.4 Synchrotron/Synchrotron Self-Compton (SSC) Model

This most popular and successful radiation mechanism explaining the broad band (radio to MeV/GeV) non-thermal emission of the relativistic jets is SSC model [24], where the low energy component of the spectrum is interpreted as synchrotron radiation, while the high energy component is described by IC scattering on the same population of electrons.

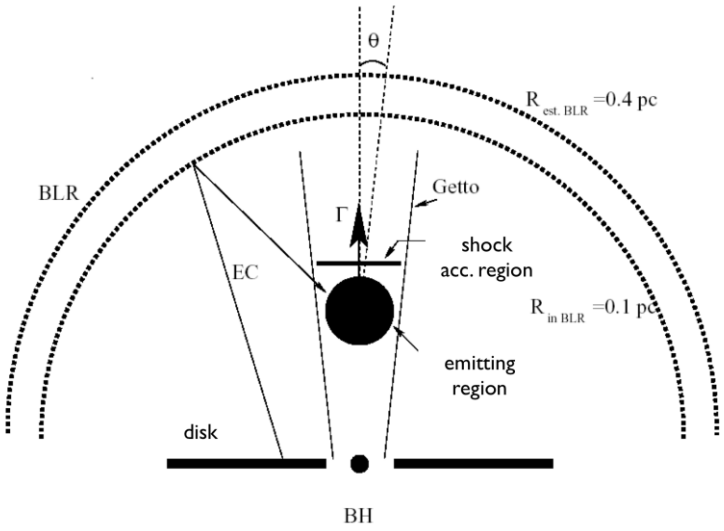

Figure 1.4: Scheme showing one zone homogeneous spherical region moving with relativistic velocity within the jet.

To compute the radiation, it is assumed, that the radiation is produced in spherical region,

where the electrons are accelerated through the first order shock or stochastic second order mechanisms. As the emitting region moves with relativistic velocities, the radiation is beamed by $\delta_D = 1/(\Gamma(1 - \beta cos\,\theta))$, which amplifies the flux (νF_ν) by δ_D^4. In general case, the observed flux of SSC is [22]

$$f_{\epsilon_s}^{SSC} = \frac{9}{16}\frac{(1+z)^2\sigma_T\epsilon_s'^2}{\pi\delta^2c^2t_{v,min}^2}\int_0^\infty d\epsilon'\frac{f_\epsilon^{syn}}{\epsilon'^3}\times\int_{\gamma'_{min}}^{\gamma'_{max}} d\gamma'\frac{N_e'(\gamma')}{\gamma'^2}F_c(q,\Gamma), \qquad (1.13)$$

where $\epsilon = h\nu/mc^2$ and $\epsilon_s' = h\nu_s'/mc^2$ are the dimensionless radiated photon energies in the observed and lab frames, respectively and $t_{v,min}$ represents the minimum variability scale of the flux in the observer frame.

1.3 The Neil Gehrels Swift Observatory and the Fermi Gamma-ray Space Telescope

Relativistic jets in AGNs are responsible for the non-thermal emission, which covers the whole electromagnetic spectrum. To understand the origin of the emission it is important to study these sources especially in optical/X-ray and γ-ray bands, since the emission in these bands are most likely produced from the single population of the electrons.

Instrument	Energy range	Observing range
Swift/UVOT	Optical/UVOT	170-650 nm
Swift/XRT	Soft X-ray	0.3 – 10 keV
Fermi/LAT	γ-ray	0.1– 300 GeV

Table 1.1: The main detectors provided the data used in this work.

In this section the detailed description of the data analysis obtained by the detectors on the board of Swift Observatory and FGST are presented (except for the instruments, which data were not used during this work). The Fermi Large Area Telescope (Fermi-LAT) is the main detector on the board of FGST operating in the HE γ-ray band since August 2008. Swift telescope was launched on 2004 with three instruments on the board (Ultraviolet/Optical

Telescope (UVOT), X-ray Telescope (XRT) and Burst Alert Telescope (BAT)). Initially, its main mission was to detect gamma-ray bursts (GRBs), but then it was also used to study AGNs. The observational energy ranges of detectors, which data are used in this thesis are listed in Table 1.1.

1.3.1 The Neil Gehrels Swift Observatory

The "Neil Gehrels Swift Observatory" space telescope caries three instruments on board providing data in the optical/UV, X-ray and γ-ray bands. The descriptions of these instruments are presented below (for more details please see [25]):

The Burst Alert Telescope (BAT). The BAT shown in Fig. 1.5 (upper right panel) is hard X-ray transient instrument with large field of view (FOV) (1.4 sr) and operates in 15-150 keV energy range. The large FOV allows 88% observation of the sky each day, detecting the photons with 64 seconds time resolution. The last all-sky survey of the BAT telescope is based on observations during 70 months, which mostly contains AGNs.

The X-Ray Telescope (XRT). The Swift/XRT (see Figure 1.5, middle panel) is CCD based telescope, which performs localization, spectroscopy and light curve monitoring. It has 110 cm^2 effective area, 18-arcsec resolution, 23.6×23.6 arcsec FOV and detects photons in 0.2-10 keV energy range. The instrument can operate in four readout modes.

Imaging mode: The charged-coupled device (CCD) of this mode is like optical CCD, but unlike Photon Counting (PC) mode, this allows photons to be piled up and no recognition on-board is performed. This mode is not useful for bright sources, due to the pile up effect, but it can precisely calculate centroid position and perform a good flux estimation.

Photodiode mode: This mode provides a reliable timing information with 0.14 ms time resolution. But unfortunately, this mode is useful only in low rates.

Windowed Timing (WT) mode: The WT mode like the previous one hase a good time resolution (2.2ms) providing a spatial 1-D dimensional imaging, where the central 8 arcmin of the FOV are restricted to 200 columns, and the energy resolution is not restricted. The example of this mode is presented in Fig. 1.6 (right panel). For bright sources this mode is

very useful, because the pile-up effect appears only above the count rate of $100\ \mathrm{count\ s^{-1}}$, which compared to count rates of AGNs is very high.

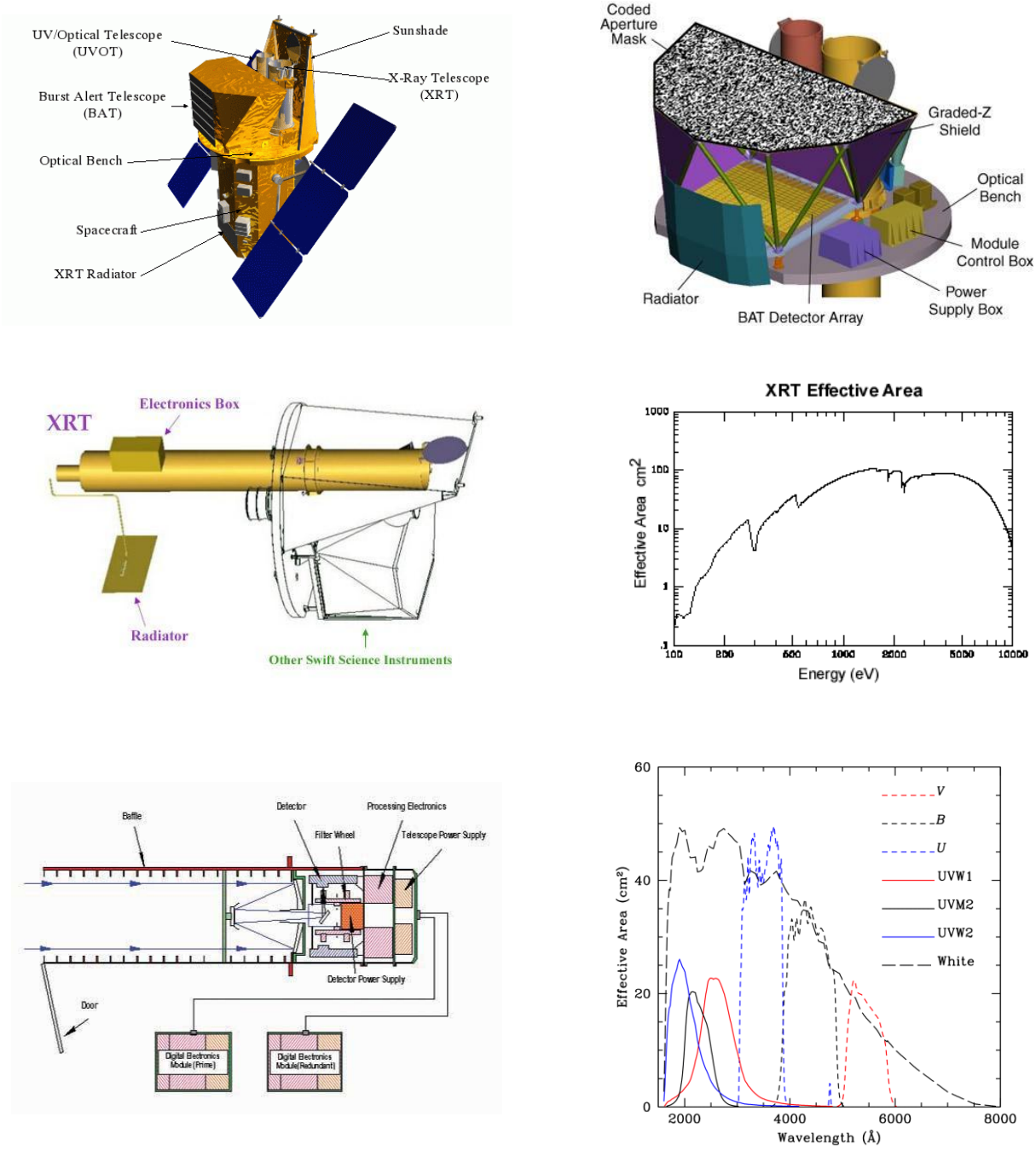

Figure 1.5: The three detectors on the board of Swift satellite (upper left panel). The burst alert (BAT) (upper right panel), the X-ray telescope (middle panel) and UV-optical telescope (bottom panel).

Photon-counting (PC) mode: The PC mode is based on the traditional frame transfer operation of X-ray CCD. Unlike the WT mode, the imaging for this mode is two

dimensional. The energy resolution is not restricted and the time resolution compared to WT mode is bad (2.5 s). This mode is useful in low rates ($< 0.5\ \mathrm{count\ s^{-1}}$), where the pile-up effect is negligible, but for higher rates we restore the PSF following the procedure described in [26].

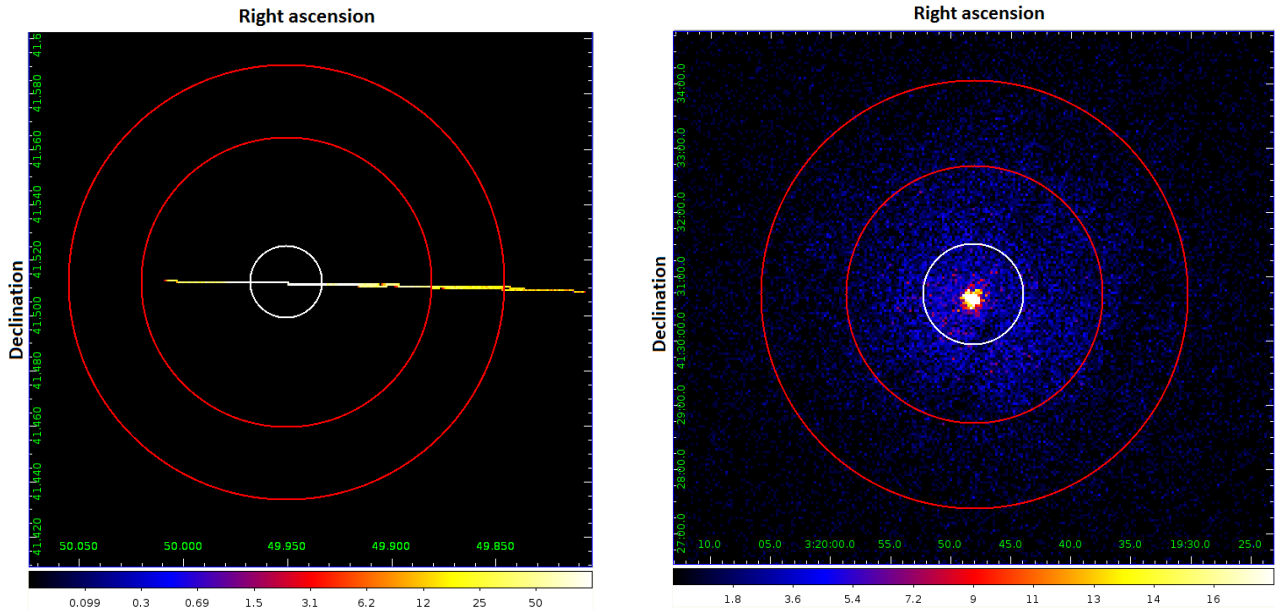

Figure 1.6: Examples of PC and WT modes with the chosen source and background regions.

The Ultraviolet/Optical Telescope (UVOT). The UVOT is a 30 cm modified Ritchey-Chretien optical/UV telescope performing optical and UV photometry in (170-650 nm) waveband using seven lenticular filters (see Figure 1.5, lower panel). The FOV of this telescope is $17' \, x \, 17'$ containing 2048×2048 pixels. Despite the poor aperture, this detector is a good addition to other detectors, providing simultaneous multifrequency data.

1.3.2 The Fermi Gamma-ray Space Telescope (FGST)

FGST telescope was launched in August 2008 carrying 2 instruments on the board: Large Area Telescope (LAT) and Gamma-ray Burst Monitor (GBM). Below we describe common technical details of these detectors and the detailed descriptions are provided in [27].

Large Area Telescope (LAT): The LAT is pair-conversion telescope sensitive to high energy γ-ray photons in the 20 MeV–300 GeV energy range (see Fig. 1.7). Every moment, it scans 20% of the sky and covers the whole sky every 3 hours. This detector consists of

calorimeter for energy measurement, 16 dual silicon particle tracking detectors and data acquisition module. The detection principle of Fermi-LAT is following: photons interact with thin tungsten layers called conversion foils and under the field of a heavy nucleus produces electron and positron pairs. Then, these pairs pass through the silicon strips detecting by calorimeter. When the charged cosmic particles passes the outer layer, called anticoincidence shield, a flash of light is produced, which allows to distinguish γ-rays from the charged particles. After the detection of photons in the calorimeter all necessary information such as direction and energy can be estimated.

The Gamma-ray Burst Monitor (GBM): The GBM γ-ray detector is used for detecting photons from the γ-ray bursts. This instrument consists of two groups of scintillators. One of them contains 12 sodium iodide (NaI) scintillators and works in low energy range (from several keV to 1 MeV). The second one is made of 2 cylindrical bismuth germanate (BGO) scintillators and works comparatively in high energy range (~150 keV to ~30 MeV).

1.4 Data Analysis: Swift UVOT/XRT and Fermi-LAT

In this thesis the Fermi-LAT and the Swift UVOT/XRT data are mostly analyzed. Below the main steps and methods of the data analyses are provided. The parameters applied here are only for demonstrative purpose and exact values will be provided in each chapter.

1.4.1 Fermi/LAT Data Analysis

Data extraction. For the analyses the last reprocessed PASS 8 publicly available photon and spacecraft (this contains information about position and pointing) data are dowloaded, which contain source position (coordinates), search radius, observation time and energy range. In the case of our studies, we mostly used the events in the energy range of (0.1-300) GeV and from the radius of 10° or 12°. The whole data reduction and analysis were performed using Fermi Sciences Tools v10r0p5 software package released on May 18, 2015 provided by Fermi collaboration.

Data reduction. As the first step, we performd appropriate cuts on the event data. Using the gtselect tool, we performe energy, time, positional and zenith angle cuts. The last cat

was done by using the maximum degree of zenith angle, which is recommended to be 90 degree and allows to minimize the effects from the photons coming from the Earth's limb, which are products of the cosmic rays and the atmosphere interaction. This tool also has some hiden parameters, such as evclass=128 and evtype=3, by which allows to select only events with high probabaility of being photons. Then, we updated good time intervals with *gtmktime* tool based on the livetime and the pointing information contained in the spacecraft file. In other words, this cut provides only those events which were registered in a normal detection regime.

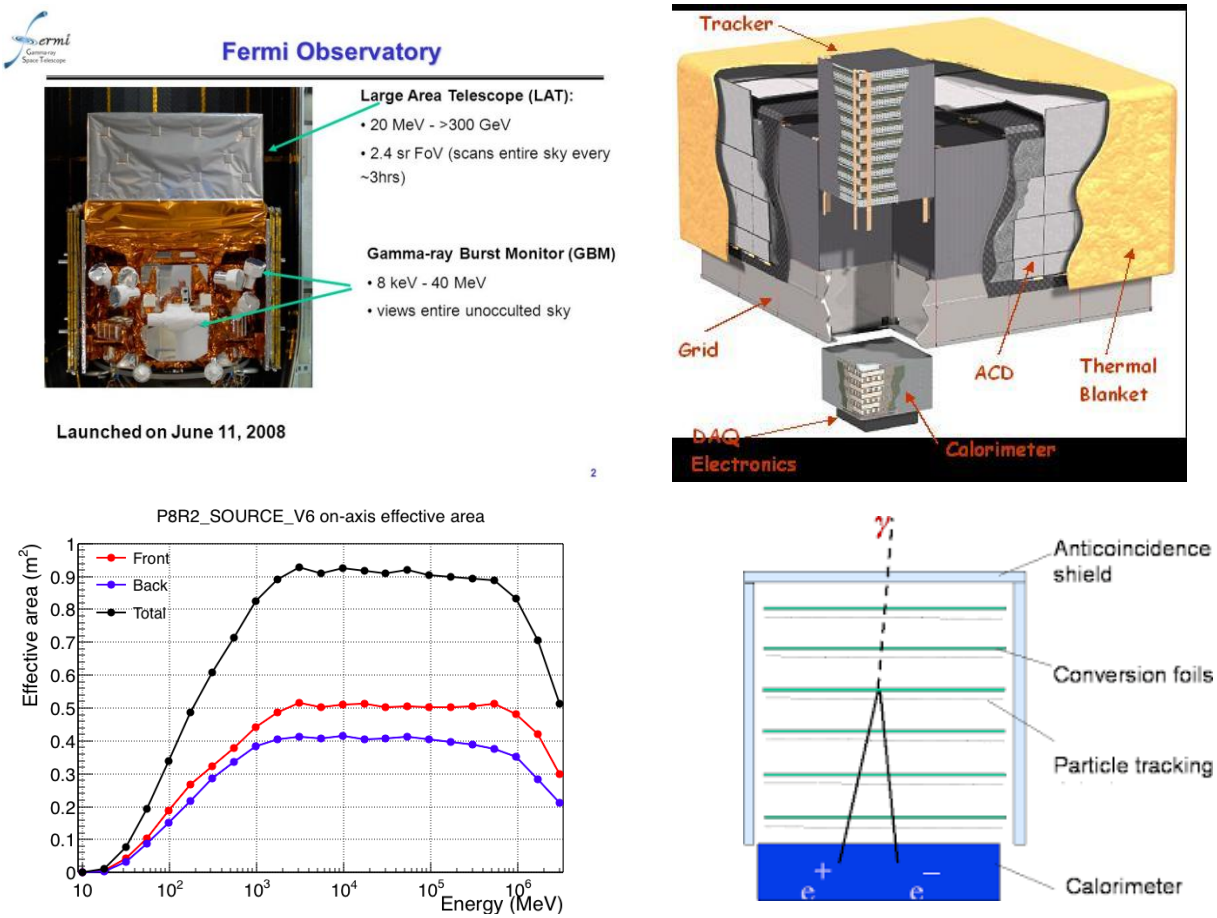

Figure 1.7: Fermi Gamma-ray Space Telescope (upper-left panel) showing two The Gamma-ray Burst Monitor (GBM) and Large Area Telescope (LAT) instruments. Upper-right panel shows the structure of LAT detector, the lower-left panel ilustrates the effective area and in the lower-right panel it is presented the photon detection procedure with LAT.

For the next step of data reduction, 3-D binned count map with *gtbin* tool was created, where two dimensions are spatial sky projected coordinates binned into $0.1° \times 0.1°$ pixels

and the third dimension is 35 equal spaced energy bins in logarithmic scale. The binning was performed in the square region which can be included in the circle centered on the source position. Then, the source model file was created based on 3FGL catalog [28], which contains point sources with their appropriate coordinates and parameters obtained from the first 4 years of Fermi-LAT observations. The model includes not only sources inside the ROI, but also from outside (e.g., 5 degree). This ensures possible contribution from the distant sources, especially in the low energy range, where the angular resolution of Fermi-LAT is larger. The model also contains Galactic duffuse emision (gll_iem_v06.fits) and extrgalactic isotropic (iso_P8R2_SOURCE_V6_v06) emission models. During the last steps of data reduction, we create live-time cube with *gtltcube* tool, which contains the dependence of the sky position and the inclination angle of Fermi-LAT. The binned exposure map was computed with *gtexpcube2* tool, where *P8R2_SOURCE_V6* response function is used. And finally, using model file and the binned files we compute count map using *gtsrcmaps* tool for checking the region selections, etc.

Spectral analysis. The spectral analysis is performed with *gtlike* tool using maximum likelihood optimization methods. The principle of this method is the maximization of likelihood function trying for various sets of parameters. As the likelihood function is non-linear, the optimization is performed with non-linear algorithms called optimizers. It is recommended to use *NEWMINUIT* optimizer, which provides the best estimation of parameters. During the optimization all parameters of the background components and the sources within the ROI are left as free parameter. The input files for this analysis are the source model, the filtered event file, the spacecraft file, the exposure map, the live-time cube and the count map. The parameters obtaind from the fitting are:

- **Spectral parameters** of the sources, which in the case of simple power-law model are the normalization and the photon index.
- **The photon numbers** (N_{pred}) is the numbers of photons predicted from the model.
- **Test Statistic (TS)** is defined as $TS = 2(logL - logL_0)$, where L and L_0 are the values of likelihood function, when the source is included or not [29]. The square root of this value is the source detection significance.

Since the model file is created using the catalogue file based on the Fermi-LAT first 4-years observation, for the longer considered period there is a possibility of detecting new source, which is not accounted in the model file. To check this, Test Statistical map is created and new sources, which have $> 5\sigma$ detection significance, are added to the model.

γ-ray spectrum. The γ-ray spectrum is created by dividing the whole 100 MeV–300 GeV energy range into equal logarithmically bins and running above described fitting procedure for every bin separately. In this case, we use the model file obtained from the whole energy range fitting, where all sources and background parameters are fixed to the best fitted values and only the normalization of the considered source is left as free parameter.

γ-ray light curve. The γ-ray light curve is prepared in two different ways: for fixed time interval and with the help of adaptive binning method. In the case of normal time binning, the total considered time is divided in equal lengths and likelihood analyses is applied again for each bin. The next method is adaptively binning method [30], where the time bin is chosen to provide constant uncertainty on the flux. This method allows us to study active periods in detail, because the time bins at flaring periods are narrower than in steady states. To provide the same uncertainty, the adaptive time bins are calculated above optimal energy. Also, in this calculations, the possible contribution from the nearby and powerful sources are also taken into account. The uncertainity level depends on statistics and can be 15% or 20% range. After obtaining the time bins, we generate the light curve calculating the flux for every time using the unbinned likelihood method. This method is good for short time bins, where the number of photons are small and there is no need to perform binning. Here we again use the model obtained from the whole time analysis. The normalization of the sources within the ROI besides the considered source are left as free parameters. The spectral indices of studied sources are fixed to the best fitted values reducing the uncertainities of the fitting parameters and. As no varability is expected from Galactic difuss and exctragalactic isotropic radiations, the nomalizations of both components are fixed.

Light curve fitting. When the flares are identified in the light curves, the flare rise and decay times are estimated by fitting with double exponential function [31]:

$$F(t) = F_c + F_0 \times \left(e^{\frac{t-t_0}{t_r}} + e^{\frac{t_0-t}{t_d}} + \right)^{-1}, \quad (1.14)$$

where t_0 roughly corresponds to peak flux time, F_0 represents the constant flux level, F_c is the amplitude of the flare and finally t_r and t_d are respectively the rise and decay time of the flare. The exact value of the time, where the flare is in its maximum state can be estimated as:

$$t_m = t_0 + \frac{T_r T_d}{T_r + T_d} ln \frac{T_d}{T_r}, \quad (1.15)$$

And the largest possible size of radiation region is calculated using the shortest value among rise and decay times from the equation:

$$R' \leq \frac{c \times \min(t_r, t_d) \times \delta}{1+z}, \quad (1.16)$$

where z is the red shift and δ is the Doppler factor.

1.4.2 Swift/XRT Data Reduction and Spectral Fitting

Data extraction and reducing. We downloaded unscreened event and housekeeping files from Swift website[1]. The event file contains the data of XRT observation, which are position, time and intensity of the given event. The information about satelite, such as voltage and CCD temeprature are stored in the housekeeping file. The event data were reprocessed using *heasoft* 6.13 with *xrtpipeline* v0.13.2 creating also the exposure map (this file is used for the correction of lost counts).

Spectral extraction and rebinning. The extraction of source and background spectra is performed with *xselect* tool in FTOOLS. First, we chose source and background regions using *ds9*, then extract the spectra for appropriate regions using *xselect*, where filtering with *filter region command* is also performed. Usually, the source region for PC mode is chosen to be circle with a radius of 20 pixels around the source radio or optical position. When pile-up effect is detected, a region with larger 30 pixel radius is used removing the inner part of the PSF[2]. The background counts are extracted from annulus around the source position with 51 pixels inner and 85 pixels outer radii. For WT mode the source

[1] http://www.swift.ac.uk/index.php
[2] http://www.swift.ac.uk/analysis/xrt/pileup.php

region is selected as 20 pixels circle, while the background region is annulus with innner 80 pixels and outer 120 pixels radii symmetrically placed about the half width of WT window, as recomended by Swift team[3]. After spectral extraction, we generate Ancillary Response Function (ARF), which include information about effective area using *xrtmkarf* command in FTOOLS, where the exposure map is also inserted to perform correction for hot columns, bad pixels, the lost counts and pile-up effect (if it is present).

Before spectral fitting, we rebin the spectrum of the source to obtain enough photons in each energy bin, using *grppha* in FTOOLS with *group min rcnts* command, where rcnts value depends on the statistic of the data. If the counts rate is high, we rebin the spectrum so that each bin contains at least 20 counts and then we use chi square method to fit. Otherwise, if the count rate is low, the data are grouped with $rcnts = 1$ value providing at least one count per bin. For this case we use cash-statistic method.

Spectral fitting. The spectral analysis is performed with Xspec v12.9.1a package using the rebinned spectral and background files, the ARF and the response matrix file (RMF). The last one contains information about the probabilities of detection of the same photon with several channels of detectors. We fit the spectrum with absorbed power-law model $A(E) = KE^{-\Gamma_X}M(E)$, where K is normalization, α is photon index $M(E) = \exp[-\eta_H \sigma(E)]$ represents the photoelectric absorption with η_H hydrogen column density and $\sigma(E)$ is the cross section. To apply this, we use $phabs \times powerlaw$ model in xspec, where the column density value is taken from [32, see Fig. 1.8] beeing fixed during the fitting procedure and for the galactic abundance we used the cross section from [33]. As a result we get galactic absorbed flux, Γ_X photon index and reduced X^2 value.

Galactic absorption correction of the X-ray flux. To obtain unabsorbed corrected flux for the fitted energy range we follow the instruction given in XSPEC v12.9.1 manual[4]. After the fit we modify the model to *phabs*cflux*pow* using *editmod* command. Then we fix the normalization factor to the fitted value, chose the energy range and refit to calculate the unabsorbed flux. This fit gives us the flux and flux error in logarithmic scales.

[3] http://www.swift.ac.uk/analysis/xrt/backscal.php
[4] https://heasarc.gsfc.nasa.gov/xanadu/xspec/XspecManual.pdf

For the construction of the spectrum we rebin the data using the *setplot rebin* command with minimum significance of 5σ. After the rebinning we extract the data and the model using *iplot* and *wdata*. Also, using *delcomp* command, we set the column density to 0 and extracted the model. The anabsorbed corrected data are calculated by:

$$F_{unabsorbed} = F_{data} \times \frac{F_{model1}}{F_{model2}}, \tag{1.17}$$

where, F_{data} are data points, $F_{model1,i}$ and $F_{model2,i}$ are respectively the models with and without column density.

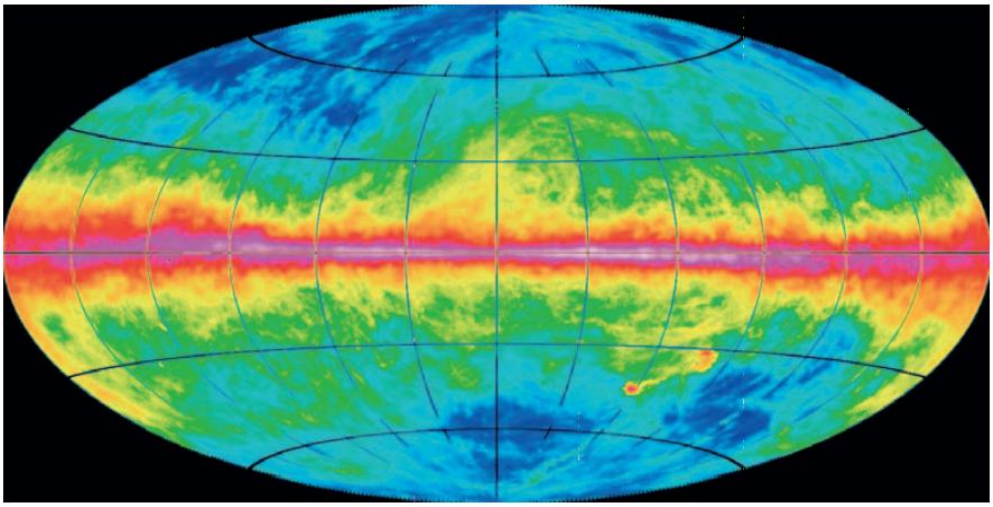

Figure 1.8: The logarithmic Aitoff projection of HI emission in the LAB dataset in $0 < N_H < 2 \times 10^{22}\ cm^{-2}$ scale integrated over the velocity range of $-400 < v < +400\ km\ s^{-1}$. Credit: [32].

1.4.3 Swift/UVOT Data Analysis and Extinction Correction

Data analysis. The UVOT data analysis is performed with HEASARC FTOOLS tools. The UVOT images are downloaded from the Swift archive, which are already pipeline processed by Swift Data Center (SDC). The source region for each filter is extracted from 5" circle around the source position, and the background region is chosen to be both annulus and circle depending on the source. Following the recommendation of UVOT team, we take annulus with inner 27.5" radius and 7.5" width, from the source free region, otherwise we change the inner (but the inner radius of the annulus can not be smaller than 15") and outer radii, so that there are no sources in it[5]. If no appropriate annulus can be found, the

[5] https://swift.gsfc.nasa.gov/analysis/threads/uvot_thread_aperture.html

events from the circular free source region beyond the 15" is selected. For each observation, we sum the multiple image extensions of the same filter to increase counts statistic. Then applying aperture photometry with *uvotsource* we calculate the magnitudes for each filter.

The Magnitude correction and conversation to flux. In order to get extinction corrected $\mathrm{M_{corrected}}$ magnitude for each optical and UV filter the A_λ extinction coefficient for each filter is calculated and then it is subtracted from the oobserved $M_{observed}$ magnitude

$$\mathrm{M_{corrected}} = \mathrm{M_{observed}} - \mathrm{A_\lambda}, \tag{1.18}$$

The selective extinction or color excess $\mathrm{E(B-V)}$ is obtained from the subtraction of observed color index $(B-V)_{observed}$ and intrinsic color index $(B-V)_{intrinsic}$:

$$\mathrm{E(B-V)} = (B-V)_{observed} - (B-V)_{intrisic}. \tag{1.19}$$

Then, the total extinction A_V can be given by:

$$A_V = R_V E(B-V), \tag{1.20}$$

where the reverse value of R_V denotes the steepnes of the extinction curve and the typical mean value is $R_V = 3.1$ [34]. The interstellar normalized extinction curve $F(\lambda)$ as a function of wavelength has the following form:

$$F(\lambda) \equiv \frac{E(\lambda-V)}{E(B-V)} = \frac{A_\lambda - A_V}{A_B - A_V}. \tag{1.21}$$

Taking into account these definations the relationship between A_λ extinction coefficient $F(\lambda)$ can be expressed as:

$$\frac{A_\lambda}{E(B-V)} = R_V + F(\lambda), \tag{1.22}$$

To get A_λ, we calculate the $A_\lambda/E(B-V)$ ratios for each filter. we take $F(\lambda)$ values from the normalized extinction curve of [34], where $R_V = 3.1$ value was used and the $E(B-V)$ values are taken from [35].

In the next step we convert the corrected magnitudes to count rate as described in [36]:

$$C = \frac{2}{5} e^{\frac{M_{zero}}{M}}, \tag{1.23}$$

where M_{zero} is photometric zero point magnitude (it corresponds to the magnitude, when $C = 1\ counts\ s^{-1}$). These values for each filter are provided in Table 1.2.

For the count rate to flux conversation we took the apappropriate latest $\mathrm{A_{cf}}$ factors from [37] for each filter and convert them into flux in the units of $erg\ cm^{-2}s^{-1}$:

Filters	λ_{eff}^{a} [Å]	M_{zero}^{b} [magnitude]	$A_\lambda/E(B-V)^{c}$	A_{cf}^{d} $[10^{-16} \times erg\ cm^{-2}s^{-1}\mathring{A}^{-1}]$
V	5402	17.89	3.11	2.613
B	4329	19.11	4.12	1.471
U	3501	18.34	4.89	1.628
W1	2591	17.44	6.47	4.209
M2	2229	16.85	9.30	8.446
W2	2033	17.38	8.80	5.976

Table 1.2: Parameters provided for extinction correction of Swift/UVOT filters.

Notes:

a) The effective wavelengths in Vega like spectrum calculated for each filter [36]

b) The zero-point magnitude.

c) These values for each filter are provided for calculation of corrected magnitude.

d) The factors for count rate to flux conversation taken from [37].

Chapter 2

2. THE FERMI-LAT OBSERVATION OF NON-BLAZAR AGNs

2.1 Introduction

The recent observations in the High Energy (HE; 100 MeV < Eγ < 100 GeV) γ-ray band show that the extragalactic γ-ray sky is dominated by the emission from different types of AGNs. The majority of detected sources are blazars (BL Lacertae objects (BL-Lacs) and Flat Spectrum Radio Quasars [FSRQs])- an extreme class of AGNs with jets forming a small angle with respect to the line of sight, which makes their emission strongly Doppler boosted [1]. Blazars are known to emit electromagnetic radiation in almost all frequencies that are currently being observed, extending from radio to very high energy (VHE; >100 GeV) γ-ray bands. Their broadband spectra are mainly dominated by the non-thermal emission from a relativistic jet pointing toward the observer. This non-thermal emission is characterized by variability in all observed energy bands with different variability time scales ranging from years down to a few minutes. The shortest variability time scales are usually observed in the HE and VHE γ-ray bands, e.g., the rapid changes of the γ-ray flux of PKS 2155-304, IC 310, PKS 1510-089, 3C 454.3, 3C 273, PKS B1222 + 216, etc. [38; 39; 40]. This implies that the emission is produced in a very compact region, which provides a unique chance to investigate the jet structure and emission from sub-parsec regions.

Besides blazars, the γ-ray emission from other types of AGNs (e.g., which do not show a clear evidence for optical blazar characteristics or have jets pointing away from the observer (non-blazar AGNs)) have been also detected. These sources were not considered as favored GeV emitters, because the non-thermal emission from their jets is less Doppler boosted. After the launch of Fermi-LAT, several non-blazar AGNs (mostly radiogalaxies) were detected already in the first year of observations [41, 42, 43, 44]. This provided a

chance to investigate also the emission from extended non-boosted regions, moderately relativistic plasmas, etc.

Analyzing the Fermi-LAT data accumulated during the first fifteen months of observations of non-blazar AGNs (including seven FRI radiogalaxies and four FRII radio sources consisting of two FRII radiogalaxies and two steep spectrum radio quasars [SSRQs]), [45] showed that their average γ-ray spectral indexes are comparable, but they are somewhat less γ-ray luminous than their parent population of BL Lacs and FSRQs. Despite the fact that a few non-blazar AGNs had been detected, which prevented extensive population studies, the observations of individual sources provided new and interesting results. Most interesting is perhaps the detection of γ-ray emission from the lobes of Centaurus A (Cen A) and Fornax A [46, 47] radiogalaxies. In the case of Cen A, the emission extends up to ≈ 3 GeV with a soft photon index of $\Gamma \simeq 2.6$ and its flux makes more than half of the total source emission [46]. Instead, the γ-ray emission from the lobes of Fornax A has a power-law photon index of $\Gamma \simeq 2.0$ and extends up to 20 GeV. It illustrates that the bipolar or quasi-symmetrical structures in the radio maps around almost all the radiogalaxies can be potential sources of γ-rays.

The γ-ray spectra of some radiogalaxies appeared with interesting features above several GeV. For example, during the γ-ray flaring activity of NGC 1275 in April-May 2009, a hysteresis behavior in the flux versus photon index plane was observed [48], when the γ-ray photon index hardened from $\Gamma \simeq 2.2$ to $\Gamma \simeq 2.0$. Next, during its major γ-ray flares of October 2015 and December 2016/January 2017, in the flux versus photon index plane the spectral evolution followed correspondingly a counter clockwise and a clockwise loop inferred from the light curve generated by an adaptive binning method [49]. Another example is the second component in the γ-ray spectrum of the Cen A core emission; at $E_b \simeq (4.00 \pm 0.09$ GeV the photon index changes from $\Gamma_1 = 2.74$ to $\Gamma_2 = 2.09$ [50].

The multiwavelength observations of two well known radiogalaxies, 3C 111 and 3C 120, which show superluminal apparent motions in their radio jets, provided some clue on the localization of the emitting region. From 2008 to 2010, 3C 111 had only occasionally been detected in the HE γ-ray band. It was bright at the end of 2008, and faint for the rest of the

time [51]. These bright periods in the γ-ray band coincide with the millimeter-optical-X-ray outburst, suggesting cospatiality of the events, which allowed to localize the γ-ray dissipative zone to be at a distance of about ~ 0.3 pc from the black hole in a compact region confined within ~ 0.1 pc [51]. Similarly, very long baseline interferometry and very long baseline array monitoring of 3C 120 reveal that its γ-ray activity is accompanied by the radio and millimeter core brightening followed by the ejection of a superluminal knot [52], where it was shown, that γ-rays are detected only when the components are moving in a direction closer to our line of sight. The analysis of γ-ray events detected during the superluminal components ejection periods shows that the γ-ray emission region is within ~ 0.13 pc from the millimeter VLBI core [52].

The origin of the γ-ray emission from non-blazar AGNs is another puzzling problem. In the case of blazar, the fast variability indicates, that the emission is produced in a compact region of the jet which narrows the range of possible emission mechanisms. For some non-blazar AGNs, their jets are less Doppler-boosted, thus the γ-ray emission from other potential sites (e.g., moderately relativistic outflows, radio lobes, accretion regions, etc.) can be detected as well, making exact theoretical modeling of the origin of emission harder. Even when the emission is most likely produced in a compact region of the jet (e.g., Cen A core [41], M 87 [42] and NGC 1275 [42]), the most popular one-zone synchrotron/synchrotron self Compton (SSC) model clearly fails to explain the observed multiwavelength properties. More complicated models, multi-zone [53] or structured jet [54, 55], based on different assumptions should be employed to explain the observed data properly. New and high-quality data are still needed to fully understand the origin of multiwavelength emission from non-blazar AGNs.

We note that the emission from some non-blazar AGNs extends up to the VHE γ-ray band, allowing detecting them by current generation of ground-based detectors. The observations of non-blazar AGNs in MeV/GeV (HE) and > GeV (VHE) bands, allowed to examine the non-thermal emission processes in the jets of AGNs which are not strongly affected by Doppler boosting. Up to now only the spectra of Cen A, M 87, NGC 1275 and PKS 0625-35 have been measured in the MeV/GeV and TeV bands. The recent simulations show that at least

eight new non-blazar AGNs will be detected by CTA at $\sim 10\sigma$ under the assumption of a straight extrapolation of the Fermi-LAT measured power-law spectra in the CTA energy range [56]. In this view, the study of the non-blazar AGNs γ-ray spectra above $\sim GeV$ is presented [57], which can be done with much improved statistics than before, since i) the Fermi-LAT data from longer periods of observation are collected and available and ii) the recent update of the event-level analysis from PASS7 to PASS8. Moreover, using longer periods, it will be possible to study the γ-ray flux variability in both long and short time scales. This is crucial for theoretical modeling and distinguishing between compact and extended emission regions. This is why these sources are considered to study in the γ-ray band.

2.2 The studied Sources

The majority of AGNs detected by Fermi-LAT are blazars, FSRQs and BL Lacs, and the number of unknown-type blazars is almost the same as that of FSRQs ($\sim$ 460) [58]. Only a very small fraction of the total sample (2%) are non-blazar AGNs, including fourteen radiogalaxies, six SSRQs, one Compact Steep-Spectrum Quasar (CSSs), five Narrow Line Seyfert 1s (NLSy1s) and five other AGNs. From this list, the other AGNs show spectral energy distribution (SEDs) typical for radio-loud compact-core objects, but data are lacking to be more specific about their classes, thus we have excluded them from our sample. Other sources have well-established classification and/or have a well evaluated optical spectrum (with clear evidence for or lack of emission lines) and some of them are also related with blazars in the unification scenario proposed for radio-loud AGNs (e.g., FRIs with BL Lacs, while FRIIs are linked with FSRQs [1]. All these objects are included in the source sample, i.e., AGNs with relativistic jets which are not blazars, and they are collectively referred as non-blazar AGNs. Even if some of these sources might have different jet properties (e.g., the jets of 3C 111 and 3C 120 with superluminal apparent motions, or the jets of some objects have a smaller but still larger viewing angle than that of blazars) they are not excluded from the sample to have a general view of the comparison of γ-ray emission characteristics of blazar and non-blazar objects.

The radiogalaxies detected in the γ-ray band so far can be sub-divided into two morphological types, FRI and FRII [3], according to their radio luminosities.

Name	3LAC	2LAC	1LAC	Type	Ph. Index
NGC 1218	J0308.6+0408	-	J0308.3+0403	FRI	2.07 ± 0.11
IC 310	J0316.6+4119	J0316.6+4119	-	FRI/BLL	1.90 ± 0.14
NGC 1275	J0319.8+4130	J0319.8+4130	J0319.7+4130	FRI	2.07 ± 0.01
1H 0323+342	J0325.2+3410	J0324.8+3408	J0325.0+3403	NLSy1	2.44 ± 0.12
4C+39.12	J0334.2+3915	-	-	FRI/BLL?	2.11 ± 0.17
TXS 0348+013	J0351.1+0128	-	-	SSRQ	2.43 ± 0.18
3C 111	J0418.5+3813	-	J0419.0+3811	FRII	2.79 ± 0.08
Pictor A	J0519.2-4542	-	-	FRII	2.49 ± 0.18
PKS 0625-35	J0627.0-3529	J0627.1-3528	J0627.3-3530	FRI/BLL	1.87 ± 0.06
4C+52.17	J0733.5+5153	-	-	AGN	1.74 ± 0.16
NGC 2484	J0758.7+3747	-	-	FRI	2.16 ± 0.16
4C+39.23B	J0824.9+3916	-	-	CSS	2.44 ± 0.10
3C 207	J0840.8+1315	J0840.7+1310	J0840.8+1310	SSRQ	2.47 ± 0.09
SBS 0846+513	J0849.9+5108	-	-	NLSy1	2.28 ± 0.04
3C 221	J0934.1+3933	-	-	SSRQ	2.28 ± 0.12
PMNJ0948+0022	J0948.8+0021	J0948.8+0020	J0949.0+0021	NLSy1	2.32 ± 0.05
PMN J1118–0413	J1118.2–0411	-	-	AGN	2.56 ± 0.08
B2 1126+37	J1129.0+3705	-	-	AGN	2.08 ± 0.13
3C 264	J1145.1+1935	-	-	FRI	1.98 ± 0.20
PKS 1203+04	J1205.4+0412	-	-	SSRQ	2.64 ± 0.16
M 87	J1230.9+1224	J1230.8+1224	J1230.8+1223	FRI	2.04 ± 0.07
3C 275.1	J1244.1+1615	-	-	SSRQ	2.43 ± 0.17
GB 1310+487	J1312.7+4828	J1312.8+4828	J1312.4+4827	AGN	2.04 ± 0.03
Cen A Core	J1325.4-4301	J1325.6-4300	J1325.6-4300	FRI	2.70 ± 0.03
Cen A Lobes	J1324.0-4330	J1324.0-4330	J1322.0-4515	FRI	2.53 ± 0.05
3C 286	J1330.5+3023	-	-	SSRQ	2.60 ± 0.16
Cen B	J1346.6-6027	J1346.6-6027	-	FRI	2.32 ± 0.01
Circinus	J1413.2?6518	-	-	Seyfert	2.43 ± 0.10
3C 303	J1442.6+5156	-	-	FRII	1.92 ± 0.18
PKS 1502+036	J1505.1+0326	J1505.1+0324	J1505.0+0328	NLSy1	2.61 ± 0.05
TXS 1613-251	J1617.3-2519	J1617.6-2526	-	AGN	2.59 ± 0.10
PKS 1617-235	J1621.1-2331	J1620.5-2320	-	AGN	2.50 ± 0.23
NGC 6251	J1630.6+8232	J1629.4+8236	J1635.4+8228	FRI	2.22 ± 0.08
3C 380	J1829.6+4844	J1829.7+4846	J1829.8+4845	SSRQ	2.37 ± 0.04
PKS 2004-447	J2007.8-4429	J2007.9-4430	J2007.9-4430	NLSy1	2.47 ± 0.09

Table 2.1: Non-blazar Misaligned AGNs included in Fermi-LAT 3LAC catalog.

An example of an FRI is the nearby radiogalaxy Cen A, and Pictor A with its peculiar jet is an example of FRII. Increasingly aligned versions of FRIIs are SSRQs, which are powerful radio sources with large-scale radio structures and which appear at intermediate angles between FRIIs and FSRQs. SSRQs are sometimes classified as CSS quasars, since most of the radio flux is emitted within galactic scales (< 10 kpc) rather than at hundreds of kilo-parsec scales [59]. Their radio structure on milliarcsecond scales is similar to the morphology of a large radio source with lobes, hot spots and jets; because of this similarity and the observed high radio power, these sources are thought to be the precursors of large radiogalaxies observed at the early stage of their expansion [10]. In the third catalog of AGNs detected by Fermi-LAT, only 4C +39.23B has been classified as a CSS quasar although SSRQs 3C 286 and 3C 380 also have characteristics similar to CSSs.

Recently, NLSy1s have also been classified as γ-ray emitters [18]. NLSy1s are AGNs with optical spectral properties similar to those of Seyfert 1 galaxies, except for having narrow Balmer lines and strong optical FeII lines [13]. NLSy1s exhibit strong X-ray variability, steep X-ray spectra, relatively high luminosity, and a substantial soft X-ray excess [60]. These characteristics point to systems with a central black hole having smaller mass ($10^6 - 10^8\ \mathrm{M}_\odot$) and higher accretion rates (close to or above the Eddington limit). Up to now it is not clear whether or not the jets of NLSy1s make a small angle to the observer's line of sight, however, they are very bright and interesting γ-ray emitters. Including them in our sample allows us to compare their γ-ray spectra, flux, luminosity, etc. with those of radiogalaxies and blazars (aligned and not aligned cases) which facilitates their jet studies. The considered sources are presented in Table 2.1 taken from 3LAC AGNs catalog [58] and below some details about all individual sources are presented.

2.2.1 FR-I and FR-II Radiogalaxies

Centaurus A (Cen A): This massive eliptical radiogalaxy (otherwise NGC 5128), is classified as FR-I radiogalaxy being the closest AGN to us ($d_L = 3.7\ Mpc$, [61]). In the radio band this source has $10'$ angular size [62], which is equivalent to ~ 0.6 Mpc physical extention. This source consists of two giant lobes in the outer part, while the central region contains a

supermassive black hole with $5.5 \times 10^7 M_\odot$ mass, powering a relativistic jet with $70°$ inclination angle [63]. Due to its near distance, this source has been frequently observed from radio to VHE γ-rays (e.g., [64]). Cen A was the first AGN, where the γ-ray emission from the the radio lobes were detected using Fermi-LAT data accumulated in the initial 300 days of observation. The emission from the core of this source was detected also in VHE γ-ray band with High Energy Stereoscopic System (H.E.S.S.) [65]. The broadband emission from the Cen A core up to several GeV was successfully explained by simple single zone SSC model, suggesting that the electrons were produced in the inner part of the jet, although it was not possible to include the non-simultaneous HESS data during the modeling [46]. However, the analyses of longer Fermi-LAT accumulated data showed that above 4.00 ± 0.09 GeV the γ-ray spectrum becomes harder, when the photon index changes from Γ=2.74±0.03 to Γ=2.09±0.20 indicating, that there is a second high energy emission component. In order to explain this component, the non-thermal processes in the magnetosphere of the black hole [65], multiple SSC components (i.e., [53]), γ-ray pair-cascades in the the torus at $\sim 10^3\ R_S$ (Schwarzschild radius) (e.g., [66]) and other scenarios were discussed. The high energy γ-ray emission from the lobes can be explained as inverse Compton (IC) up-scattering of microwave background (CMB) photons [46].

3c 264: This source also known as B 1142+198 is classified as FR-I and considered as one of the luminous galaxies in the Abell 1367 cluster with z = 0.0217 [67]. In the radio band, in its kilo parsec structure a nucleus with a jet in the northeast direction extending up to 28" (11.5 kpc) [68] were observed. Also, an evidence of the counterjet in the southwest direction was observed [69]. Besides, the radio and optical bands, this source was detected in X and γ-ray bands, making the jet of this source a candidate for deep multifrequency study.

3C 120: This broad line radiogalaxy, with z=0.033, is a powerful emitter almost in all bands. The radio morphology is similar to FR-I class, although superluminal components from the kpc-scale jet, with $\gtrsim 10°$ inclination angle, have been detected [70]. Most likely, the emission in the X-ray band is mainly produced from the accretion disc, as very high X-ray luminosity has been observed, which follows from the fact that this source has been detected in the γ-ray band by Fermi-LAT after the first 15 months observation [45]. It is

interesting that the radio and millimeters brightening events are correlated with γ-ray events [52]. Similar coincidence has been also observed between the dips in the X-ray bands and the superluminal components ejection observed in radio band [71]. This allowed to conclude the accretion disc and jet relation in this source. As shown in [72], within a year and half-year time binning, this source is almost undetectable in the first six years of Fermi-LAT observation and then significantly increases, showing variability in long time scales. A γ-ray variability within short time scales (days and sub-days) was also observed as reported in [54]. The γ-ray emission in steady state can be explained by SSC mechanism [72], whereas for the flaring states more complex spin-layer model was used [54]. This source is interesting for large scale jet emission studies, since it has several bright knots in the jet, which were resolved with Chandra telescope.

NGC 2484: This FR-I class radiogalaxy also known as B2 0755+37 is located in Abell S740 galaxy cluster with z=0.0413. It has a jet in the North-West and South-East directions forming lobes. First one is imbedded in the South-East lobe, while the second jet is compressed in the beginning and becomes wider in the farther part from the core [73]. Its jet has a radio polarization at the level of 5%, while the inner region and external region of the lobes are highly polarized up to 25% and 35%, respectively [74]. This source has been detected in the γ-ray band after the four years of Fermi-LAT observations (3LAC, [58]) with 4.56σ detection significance.

Centaurus B: This radio-loud radiogalaxy is a comparably nearby ($d_L = 56\,Mpc$, [75]) with $\simeq 24'$ angular size, which corresponds to approximately 380 kpc linear size for the source distance. It is very bright in the radio band [76], but the proximity to the Galactic plane and inaccessibility from the northern hemisphere has not alowed to study this radiogalaxy better. The observation of this source in the radio band was performed using the data of Australia Telescope Compact Array (ATCA) (4.80 and 8.64 GHz) and Molonglo Observatory Synthesis Telescope (MOST) (843 MHz) [76], which revealed jets and diffuse lobes around the core. The radio classification of this source is a bit tricky, as the edge of the northeastern lobe is sharper similar to FR II radiogalaxies [77], while the bright jet and diffuse lobes obviously have the morphology of FR I class. Also, the radio luminosity of this

radiogalaxy at 1.4 GHz is $L_{1.4\,GHz} = 5 \times 10^{41} erg\, s^{-1}$, which lies close to the division of the FR I/FR II limit. Accordingly this source has intermediate classification between FR I and FR II sources. The X-ray diffuse emission from the lobes first time was detected by [78] with the Advanced Satellite for Cosmology and Astrophysics (ASCA), while the radio core has been already detected in the earlier observations. The main South-Wast jet was also resolved in the X-ray band using Chandra [79] and XMM-Newton [80] telescopes. Cen B was included in the both 2LAC [81] and 3LAC [58] catalogs of Fermi-LAT showing no evidence of extended emission in γ-ray band [82].

M87: This massive FR I elliptical radiogalaxy with $\simeq (3-6) \times 10^9 M_\odot$ central black hole mass [83] is located in the Virgo cluster and has the second nearest distance ($d_L \approx 16.4$, [84]) among the Fermi-LAT detected AGNs. The one sided jet of this radiogalaxy with $\sim 30"$ scale [85] has $10^\circ - 25^\circ$ incilantion angle and shows $(4-6)c$ superluminal motion in the optical band [86]. Due to the unusual nuclear activity, the bright jet knot and the nucleus have been observed in all wavebands being the first radiogalaxy detected in VHE ($> 200GeV$) γ-ray band with High-Energy-Gamma-Ray Astronomy (HEGRA) telescope [87]. Additional observations with other TeV telescopes such as HESS, VERITAS, MAGIC have been also performed, showing short time variability. Interestingly, that the core of this source is variable in X-ray and TeV bands in day-scales, suggesting, that VHE energy radiation is coming from the inner part of the jet [88]. In the case of the HST-1 knot, the X-ray onbservations from 2000 to 2016 showed flux decrease in the last few years [88]. The broadband emission from the jet knots were enterpreted with several models, such as synchrotron radiation from electrons or IC scattering of synchrotron or CMB photons by electrons and etc. (e.g. [89, 90]). The detection of M87 with Fermi-LAT telescope first time was reported in [42] with a power-law spectral index of $\Gamma = 2.26 \pm 0.13$. The broadband emission of the core inlcuding VHE data can be explained by one-zone SSC model. Interestingly, that despite the short time variability in the X and TeV bands, no evidence of variability in HE γ-ray radiation has been detected [42].

NGC 6251: This is nearby ($d_L = 106$ Mpc, [91]) giant elliptical radiogalaxy with supermassive black hole in center with mass of $\simeq (4-8) \times 10^8 M_\odot$. The radio jet with 3

Mpc linear size [92] has $\lesssim 40^{\circ}$ viweing angle [93]. This radiogalaxy is classified as FR I due to the jet radio luminosity and the radio morphology, although there is also a hint of FR II classification, taking into account the radio structure of the whole galaxy [94]. The radio jet can be divided into four parts: the bright inner, the weak central, the outer and the weak intensity regions located at the dicatances from the core of $\lesssim 120"$, $\sim (120" - 180")$, ~(180" – 270") and $\gtrsim 270"$, respectively. The X-ray radiation has been detected not only from the nucleus and knots but also from the radio lobes, which has ~ 2.1 Mpc extent being larger than the outer lobes of Centaurus A. In this case, the X-ray emission has been explained by IC scattering of CMB photons from the electrons [95]. The γ-ray radiation from this source first time was reported in the first Fermi-LAT AGN catalog (1LAC, [96]). As shown in [97], where the lobes were excuded as the possible γ-ray sources, the broadband emission was modeled with one-zone synchrotron/SSC and structured jet models [98].

NGC 1218: This source also known as 3C 78 is S0/a radiogalaxy with FR I class radio morphology [99] and has z=029 [100]. The observation in the radio band with the Multi-Element Radio Linked Interferometer Network (MERLIN) and VLA showed one-sided jet with ~ 1 kpc scale [101]. The radio jet with inclination angle between $\approx (30^{\circ} - 40^{\circ})$ was also detected in optical band by Hubble Space Telescope (HST) with the same extention as in radio band [102]. The X-ray emission observed by BeppoSAX staellite has been explained as thermal radiation with the non-thermal contribution from the radio/optical jet [103]. The detection in γ-ray band first time was reported in [44] with $\sim 6\sigma$ detection significance and then it was included in all three Fermi-LAT AGNs catalogs.

TXS 0331+3915: This FR I class radiogalaxy with $z = 0.02$ [104] has been observed in radio band with Very Large Array (VLA) observatory at 5 GHz showing one-sided parsec scale jet [105] with $\lesssim 45^{\circ}$ viewing angle [106]. Besides the Fanaroff-Riley radio classification, it has been also classified as a low-power compact (LPC) radiogalaxy [106]. The source was detected in the γ-ray band with the detection significance of 5.02σ after the four years of Fermi-LAT observation [58].

3C 111: This powerful broad line radiogalaxy at z=0.049 [107] has FRII class radio morphology characterized by a bright core and one-sided jet, which has 78 kpc projection

size [93], a viewing angle of 18° [108] and contains many knots and northern hot spot as showed the observation with the Very Long Baseline Array (VLBA) [93]. There is also a possibility of the counter jet conditioned by the radio lobe opposite to the mentioned jet [93]. The observation with VLBA radio telescope revealed several structures, which are compact nucleus, recollimated shocks, interaction regions between the jet, the surrounding environment and many superluminal components within the jet, which reach up to $\sim 6c$ [109]. Eight radio knots were also detected in near-IR/optical and X-ray bands, respectively with Hubble Space Telescope (HST) and Chandra telescope, including the northern and southern hot sports. This source was included in the first 1LAC Fermi-LAT AGNs catalog [96], being excluded in the second AGN catalog [81] and then was included in the 3LAC AGNs catalog [58].

Pictor A: This is FR II radiogalaxy at z=0.035 [110] classified as BLRG based on the optical properties [111]. The jet of Pictor A has about 100 kpc linear size and $\lesssim 45^\circ$ viwewing angle. The radio jet of this source first time was detected using VLA telescope [110]. It showed one sided very weak jet, without any evidence of counter jet, while the lobes and the core are relatively bright. These lobes were resolved in radio band showing complex radio sub structure called hot spots [112] being observed along with the jet in the optical and X-ray bands (e.g. [113, 114]). The optical observations performed with HST showed 4 knots along the jet located in 32" 43" 106" and 112" from the core [114], which later were resolved also in the X-ray band with Chandra instrument. Initially, the detection of this source in the γ-ray band was reported in [115] with marginal $\sim 5.8\sigma$ significance based on three years accumulated data and then were included in the 3LAC AGNs catalog [58].

2.2.2 SSRQs and CSSs Quasars

3C 207: This SSRQ at z=0.684 has lobe dominated morphology [116] beeing classified as FR II radiogalaxy. Along the one-sided jet there are bright kpc-Mpc knots located in 9.95 kpc (knot-A), 32.66 kpc (knot-B) and 46.15 kpc (knot-C) distances from the core and a western lobe in the edge of the jet . These spatial regions were also detected in X-ray band by Chandra telescope, while in the optical band only the inner knot was detected with HST

[117] and also weak X-ray flux was observed by Chandra telescope. This source was included in all three Fermi-LAT AGNs catalogs with relatively steady flux, thus the possible contribution from the knots can't be excluded.

3C 275.1: This bright SSRQ at $z = 0.55$ is surounded by elliptical nebulosity. The radio observation showed a bright core and a one-sided jet in the northwest direction [118] with a $\sim 11^{\circ}$ viweing angle [119]. Another observation of VLA also detected a lobe in the edge of the mentioned jet and a faint lobe in the opposite side, without a sign of the counter jet [120]. The HST [121] and Chandra [122] telescopes also detected a hot spot in the northest lobe, which was undetectable in the radio band. This source has been included in all three Fermi-LAT AGNs catalogs.

3C 380: This SSRQ quasar initially was classified as CSS by [123] based on the early observations, where the size of this source was suggest to be less than 20 kpc. This source at z=0.692 has been observed many times in radio band with VLBA (e.g., [124]) exhibiting one-sided parsec scale jet with two knots, which was detected also in the optical band with HST telescope (e.g., [125]). As shown in [126] these radio knots are located at ~ 0.7 and ~ 1.0 arcsec from the core. This source was already detected in the γ-ray band using data accumulated during the first 11 months of observation and then was included in all Fermi-LAT AGNs catalogues.

PKS 1203+04: The VLBI observation of this SSRQ quasar showed "X" shaped structure, which contains a long curved jet and two pairs of lobes located in the opposite site of the main direction of the source [127]. One possible explanation of this structure is the change of the jet direction due to the precession of the central engine [128]. The source was included in the 3LAC [58] AGNs catalog of Fermi-LAT with detection significance of 5σ having a double association with 3FGL J1205.4+0412.

3C 286: This bright source at z = 0.849 [129] classified as CSS quasar [8] is characterized by high radio polarization. The projected radio structure is 700 pc in the southwest direction [130] contiaining a bright core (also detected in optical band with HST [131], a pc scale jet with viewing angle of 48° and two lobes in the the east and southwest directions

located at $0.7"$ and $2.6"$ from the core, respectively [132]. Interestingly, there are two compact regions in the inner part with similar emission capabilities as showed by VLBI observations [130], which were not resolved in the optical band. This is a hint of the counterjet in the direction of $\sim 90°$. Besides the radio core the HST telescope also detected a faint region in the eastern part, which is most likely associated with the mentioned Easter radio lobe [131]. This source is known with its highly radio polarization [133], which is especially noticeable at the inner part of the jet [134], with polarization of $\sim 10\,\%$. In the γ-ray band this source is relatively weak being included only in 3LAC AGNs catalog of Fermi-LAT with 5.2σ detection significance [58].

4C+39.23B: Among the misaligned AGNs from the 3LAC catalog of Fermi-LAT [58], this quasar at z = 1.21 [135] is the second CSS class source being detected with 9.2σ significance [136].

2.2.3 γ-NLSy1 Galaxies

PKS 1502+036: This RL-NLSy1 at z=0.409 has a black hole with the mass of $4.5 \times 10^7 M_\odot$ [20]. This source is characterized by $FWHM\,(H\beta) = (1082 \pm 113)\,km\,s^{-1}$, $[OIII]/H\beta \sim 1.1$, a strong bump in FeII emission line and has relatively high value of radio loudness ($RL = 1549$ defined as the ratio between the flux densities at 1.4 GHz and 4400 Å [137]. This source was also included in the sample of high frequency peaked (HFP) AGNs due to the radio spectrum peak above 5 GHz [138]. A core-jet structure with pc-scale was resolved by VLBI at 15 GHz [139]. In the γ-ray band this source was included only in the 3LAC catalog [58].

PKS 2004-447: Another RL-NLSy1 galaxy detected by Fermi-LAT in 2009 [18] at z=0.24 [140] has a black hole mass of $5 \times 10^6 M_\odot$ estimated by Hβ line [141]. The optical properties are similar to those of NLSy1s with $FWHM\,(H\beta) = 1447\,km\,s^{-1}$ and $[OIII]/H\beta = 1.6$, while the FeII line is weak ($EWFe\,II \leq 10$ Å) [141]. The radio structure resolved by VLBI at 8.4 GHz exhibited a typical one-sided jet core structure. The radio loudness of this source is high enough and changes dependent on the optical flux $RL = f_{4.85\,GHz}/f_{optical} > 1700$ [141]. The properties of the rest three NLSy1 sources are presented in Chapter 5.

2.3 The Analysis of Fermi-LAT Data

Data analyses: The data preparation and analyses were performed as described in section 1.4.1, here only main parameters are provided. Mainly, the data set used here was collected during the first 7 years of Fermi-LAT operation, from August 4 2008 to August 4 2015.
The photons from a circular region with a radius of 10° around each source under consideration were used, except for 3C 207, M87, PKS 1502+036, PKS 2004-447 and 1H 0323+342, around which a region with a radius of 12° was used for a better representation of the ROI. By selecting different radii of the ROI we ensure that the selected ROI is an accurate representation of the observation. The model file for each source is created using the Fermi-LAT third source catalog [28] (3FGL) where all sources falling between ROI and $ROI + 5^\circ$ region are included in it. The normalization of background models as well as fluxes and spectral indexes of the sources within ROI are left as free parameters in the analysis while for the sources outside ROI, the spectral slopes and normalizations were fixed to the values given in the 3FGL catalog.

Spectral analysis: In order to find the best matches between spectral models and events, the binned likelihood analysis is performed with *gtlike* tool as described in section 1.4.1. The detection significance of each source is quantitatively estimated using the Test Statistics (TS) defined in section 1.4.1. The spectra of the considered sources are modeled with a Power-Law (PL) model in the form of

$$\frac{dN}{dE} = N_0 \left(\frac{E_\gamma}{E_0}\right)^{-\Gamma} \tag{2.1}$$

where the normalization N_0 and γ-ray photon index Γ are considered as free parameters.

If deviation from the power-law model is found, then a more complex power-law with exponential cut-off model in the form of

$$\frac{dN}{dE} = N_0 \left(\frac{E_\gamma}{E_0}\right)^{-\Gamma} Exp\left(-\left(\frac{E_\gamma}{E_0}\right)^{-\beta}\right) \tag{2.2}$$

is used, where N_0, Γ and E_c are free parameters. First we fix the value of $\beta = 1$, then consider it also as a free parameter. Since the log-parabolic spectral shape gave a better

modeling for the spectra of some blazars [142], we consider also the log-parabola model in the form of

$$\frac{dN}{dE} = N_0 \left(\frac{E_\gamma}{E_0}\right)^{-\alpha-\beta \log(E_\gamma/E_b)}, \quad (2.3)$$

where N_0, α and β are free parameters. Different models are compared using a log likelihood ratio test: the TS is twice the difference in the log likelihoods and its probability distribution can be approximated by a $\chi 2$ distribution.

The spectra of each source are calculated by separately running *gtlike* for smaller energy intervals equal in logarithmic space. In each bin the flux is estimated by fitting the power-law model with the spectral slope fixed at the value obtained by the fit in the entire energy range and the bins only with $TS \geq 4$ were considered. Using the data accumulated for longer time than used in 3FGL can result in new γ-ray sources in the ROI, which are not properly accounted for in the model files. In order to probe for additional sources, a TS significance map on a square grid with $0.1^\circ \times 0.1^\circ$ spacing that covers the entire ROI is created using the best-fit model. If there were excess hot-spots with $TS > 25$ we sequentially added a new point source with a conventional spectral definition (PL) and performed binned likelihood analysis with *gtlike*.

Temporal analysis: The γ-ray light curves are calculated by repeating the same analysis for shorter time periods as presented in section 1.4.1. The power-law slope of each source being analyzed is first fixed and then allowed to vary in the fit. Since no variability is expected for the underlying background diffuse emission, we fixed their parameters to the average values obtained in the 7-year analysis.

The minimal time interval used for light curves calculation has been chosen so that the period when the source has been detected by Fermi-LAT corresponds to the large fraction of the total bins, considering the periods when $TS > 4$. For some sources, pure statistics did not allow to investigate the variability in shorter than six-month bins while for bright sources the light curves with denser time sampling are considered. In order to identify whether the γ-ray emission is variable or not, we construct a variability index from the value of the likelihood in the null hypothesis that the source flux is constant across the considered

period, and the value under the alternate hypothesis that the source is variable [143]. If the null hypothesis is correct the variability index is distributed as $\chi 2$ with N–1 degrees of freedom where N is the number of bins used in the light curves. The source is considered variable when the variability index is equal or greater than the threshold value of 99% confidence level in a $\chi 2$ distribution with $N-1$ degrees of freedom (e.g., 115.88 and 16.81 for the light curves with a month and a year time-scales, respectively). This is a commonly accepted methodology used to identify variable sources in the Fermi-LAT catalogs (e.g. [44, 143, 28]. In order to check again the results, possible variation is also investigated using a simple χ2 test following [31].

At regular (fixed) time binning, using long bins will smooth out the fast variations during bright periods, and on the contrary, using short bins might result in many upper limits during the low-activity periods which prevents variability studies. Thus we also generate light curves with the help of the adaptive binning method [30]. Although this method has been developed for blazar studies, it can be applied to radiogalaxies as well. In the adaptive binning method, the bin width is adjusted by requiring a constant relative flux uncertainty, which produces longer time intervals during lower flux levels and narrower bins, when the source is in a high state (see also section 1.4.1 for more details). This method allows getting maximum possible information about the flux variation.

In the adaptive binning method, the light curves are with constant uncertainties of the fluxes in each time bin. In principle, the flux can be calculated above any energy, but above the optimum energy of E_{opt}, the accumulation periods necessary to fulfill the required conditions (e.g., uncertainty) are the shortest relative to other choices of energy. E_{opt} depends on the signal/background ratio and is calculated using the power-law slope (Γ) and the flux obtained in the 0.1-300 GeV interval (see the appendix of [30]). For each source, adaptive binning light curves with 15% and 20% uncertainties are generated.

2.4 The Results of the Analysis

Of the 27 non-blazar AGNs studied here, 26 are detected with $TS > 25$. The only exception is TXS 0348+013 which appeared with $TS \simeq 14$. The results from the current data analysis

are summarized in Table 2.2. For each source, the class, distance, γ-ray photon index (Γ), flux (F_γ) and luminosity (L_γ), the detection significance ($\sigma = \sqrt{TS}$) and the energy of the highest energy events with their detection times are presented. Our results have been verified by i) carrying out analyses by two different ways: first by a standard procedure as suggested by the Fermi-LAT collaboration and then by using the *Fermipy* python package, and ii) by comparing the results with the previously reported ones (from 3FGL).

The results presented here are consistent with those reported in [58], but with reduced uncertainties and a higher detection significance. The majority of the sources have been detected with $\geq 10\sigma$ which allowed to perform spectral studies above 1 GeV as well. NGC 1275 was detected with the highest detection significance of 267.4σ while 3C 303 and NGC 2484 are still detected at the threshold limit with 5.2σ and 5.6σ, respectively, because these sources were mostly undetected by Fermi-LAT during the considered period.

From Table 2.2, the γ-ray photon index of non-blazar AGNs varies from $\Gamma = 1.84$ to 2.86. The hardest photon indexes of $\Gamma \simeq 1.84 \pm 0.17$ and $\Gamma \simeq 1.89 \pm 0.04$ have been found for TXS 0331+3915 and PKS 0625-35, respectively, while the softest spectrum is observed for 1H 0323+342, $\Gamma \simeq 2.86 \pm 0.04$. Interestingly, 3C 264, NGC 1275, M87, NGC 1218 and 3C 303 have been detected with $\Gamma \simeq 2.0 - 2.1$, which corresponds to a nearly flat spectrum in the νF_ν $(erg\ s^{-1})$ representation. The brightest sources, Cen A and NGC 1275, have a flux of $\geq 10^{-7}\ photon\ cm^{-2}s^{-1}$ and the faintest source 3C 303- $(1.44 \pm 0.75) \times 10^{-9}\ photon\ cm^{-2}s^{-1}$.

Among FRIs, PKS 0625-35 ($d_L \approx 243.7$ Mpc) is the most distant source detected so far, while the other FRIs are mostly at $d_L \leq 200$ Mpc. Except for Cen A and NGC 1275, which are bright due to their proximity, as the flux of FRIs is relatively weak (a few times exceeding the Fermi-LAT sensitivity of $\approx 1.9 \times 10^{-10}\ photon\ cm^{-2}s^{-1}$ at 10 GeV), it is not expected to detect FRIs, that are much farther than those currently being observed. On the contrary, the luminous FRIIs, SSRQs (CSS) and NLSy1s are detected at much larger distances - $z > 0.1$. For instance, the most distant non-blazar AGNs detected in the γ-ray band are 3C 286 and 4C +39.23B at $z = 0.85$ and $z = 1.21$, respectively. If the observed luminosities are typical for FRIIs, SSRQs (CSS) and NLSy1s, in principle more distant

sources can be still detected (e.g., the γ-ray emission from 4C +39.23B still would be detected by Fermi-LAT even if the source is at $z \simeq 1.84$). NLSy1s detected in the γ-ray band are at $z \simeq (0.2 - 0.6)$ (except the nearby 1H 0323+342 at $z = 0.061$), which is not surprising, considering their powerful jets.

The results presented in Table 2.2 are shown in Fig. 1, the left panel of which shows the γ-ray photon index (Γ) versus flux ($F_\gamma[> 100\, MeV]$) estimated from the power-law fit. It is evident, that the considered sources have different properties as they are well separated in the $\Gamma - F_\gamma$ plane. For example, FRIs have a harder γ-ray photon index with the mean value of $\Gamma m \simeq 2.22$ and a γ-ray flux ranging from $\simeq 1.5 \times 10^{-9}\ photon\, cm^{-2} s^{-1}$ to $\simeq 3.6 \times 10^{-8}\ photon\, cm^{-2} s^{-1}$. Among FRIs, only Cen A and NGC 1275 are showing systematically different properties. In case of Cen A, the photon index and the flux are mostly defined by the low energy component (see the next section), but when using those of the second component ($\Gamma = 2.31 \pm 0.1$ and $(9.16 \pm 0.68) \times 10^{-10}\ photon\, cm^{-2} s^{-1}$), it fits well in the common properties of FRIs. NGC 1275 is a unique and particularly bright radio galaxy, so it is not a surprise that it demonstrates quite different properties. The FRIIs/SSRQs have rather similar properties and occupy a narrow area on the $\Gamma - F_\gamma$ diagram: the γ-ray photon index is $(2.3 - 2.7)$ with the mean being $\Gamma_m \simeq 2.58$ and a flux of $(0.9 - 4) \times 10^{-8}\ photon\, cm^{-2} s^{-1}$. Only 3C 303 with $\Gamma = 2.04 \pm 0.19$ is out of the mentioned area, showing properties more characteristic of FRIs. Despite using the data having been accumulated for seven years, this source is detected only with 5.2σ, causing large uncertainties in the parameter estimation. For NLSy1s $\Gamma > 2.3$ which is more similar to FRIIs/SSRQs albeit their γ-ray flux is shifted to $\geq 10^{-7}\ photon\, cm^{-2} s^{-1}$ .Worth of mentioning is the bright source PMN J0948+0022 which, being located at a distance of 3.4 Gpc, appears with the same flux as does the nearby Cen A (3.8 Mpc) but its luminosity is $\sim 7 \times 10^5$ times higher.

Even if the non-blazar AGNs considered here may have different jet properties (e.g., jet viewing angle, superluminal apparent motion etc.), it is interesting to compare their γ-ray photon index and luminosity with those of blazars. The right panel of Fig. 1 shows the γ-ray photon index versus luminosity of non-blazar AGNs and of those BL Lacs and FSRQs which

are included in the third catalog of AGNs detected by Fermi-LAT [58]. The γ-ray luminosity is estimated from the measured flux by

$$L_\gamma = 4\pi d_L^2 \, E_{max} \left(\frac{(E_{min}/E_{max})^{2-\Gamma}}{(E_{min}/E_{max})^{1-\Gamma}} \right) \times F_\gamma(> 100\ MeV),\ (E_{min} = 100\ MeV,\ E_{max} = 300\ GeV). \qquad (2.4)$$

The luminosity distance (d_L) is calculated by adopting the standard cosmological parameters of $H_0 = 70\ km\, s^{-1}\, Mpc^{-1}$, $\Omega_m = 0.27$ and $\Omega_\Lambda = 0.73$.

The previous studies of non-blazar AGNs reveal that in the $\Gamma - L_\gamma$ plane FRIs and FRIIs occupy different regions as do BL Lacs and FSRQs [45]. In case of blazars, it has been already shown that there is a well-defined boundary between BL Lacs and FSRQs.

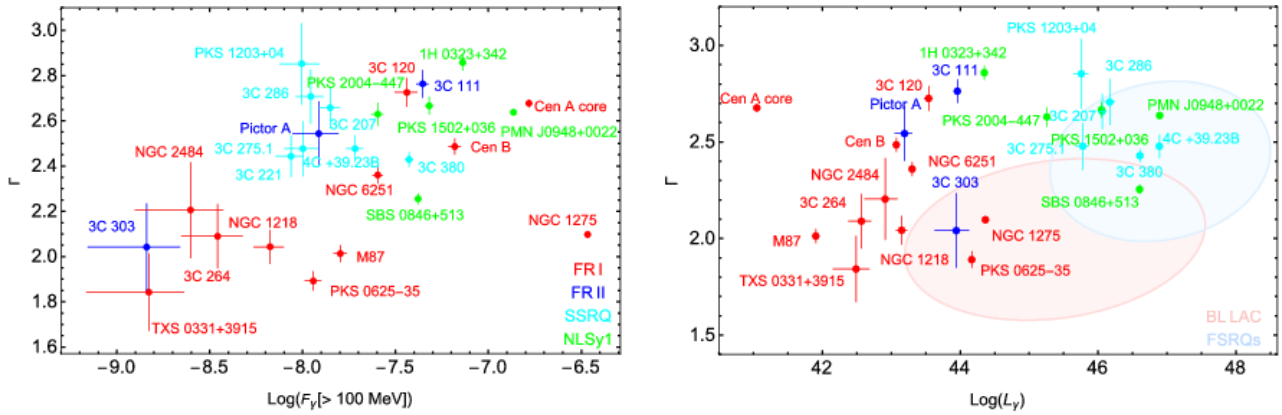

Figure 2.1: (Left Panel): The flux (E > 100 MeV) versus photon spectral index of FRIs, FRIIs, SSRQs and NLSy1s. (Right Panel): Photon spectral index vs. γ-ray luminosity of the considered sources as compared with similar properties of blazars (light blue ellipse for FSRQs and light red for BL Lacs). In both plots FRIs, FRIIs, SSRQs and NLSy1s are shown with red, blue, cyan and green colors, respectively.

BL Lacs appear with $\Gamma < 2.2$ and $L_\gamma < 10^{47}\ erg\ s^{-1}$, whereas FSRQs with $\Gamma > 2.2$ and $L_\gamma > 10^{47}\ erg\ s^{-1}$; the two blazar subclasses overlap at intermediate values of both spectral index and luminosity [144]. It has been suggested that this division is of a pure physical origin, i.e. in BL Lacs the jet propagates in a medium where the external radiation field is absent or very weak, so that the electrons are cooling less but can be accelerated to VHEs, so that low luminosity and a harder electron/photon index are expected. In FSRQs, the emitting electrons will efficiently cool down and reach only moderate energies, therefore

they will appear as luminous sources, but with a soft γ-ray photon index. Interestingly, similar division is noticeable also for FRIs and FRIIs, albeit shifted to lower luminosities (Fig. 1, right panel; the blazars have higher luminosity due to Doppler boosting). The γ-ray luminosity of most of FRIs is $L_\gamma \leq 3 \times 10^{44}\, erg\, s^{-1}$, and the photon index $\Gamma \leq 2.3$. Likewise, for FRIIs $L_\gamma \geq 3 \times 10^{44}\, erg\, s^{-1}$, and $\Gamma > 2.3$. SSRQs and NLSy1s occupy the area beyond $\Gamma > 2.3$ and $L_\gamma > 10^{45}\, erg\, s^{-1}$, and are clearly separated from FRIs and FRIIs, except for 1H 0323+342, the nearest NLSy1 having been detected so far in the γ-ray band, which has a lower luminosity of $L_\gamma < 10^{45}\, erg\, s^{-1}$. The difference of γ-ray luminosity in different source classes is in a good agreement with the unification theories: less luminous FRIs are followed by FRIIs and then by SSRQs most aligned version of FRIIs. For the sources studied here it is interesting to compare the energy released in the γ-ray band with the capability of the central source (Eddington accretion power). More reasonable would be to compare the γ-ray luminosity in the proper frame of the jet ($L_{em,\gamma} \simeq L_\gamma / 2\Gamma_{bulk}^2$) but it requires to make different assumptions to estimate unknown Γ_{bulk}. Considering that Γ_{bulk} is usually not very high for non-blazar AGNs, it is reasonable to use L_γ. We did not find black hole masses for Cen B, 3C 221, PKS 1203+04, TXS 0331+3915 and 4C +39.23B while for other sources the values available in the literature have been used. A common feature for all FRIs is that the intrinsic γ-ray luminosity corresponds to only a small portion of the Eddington accretion power - $L_\gamma / L_{Edd} \leq 10^{-4}$. For example, M87 hosts a super massive black hole with an enormous mass of $(6.6 \pm 0.4) \times 10^9\, M_\odot$ [81], but $L_\gamma / L_{Edd} \simeq 9.6 \times 10^{-7}$ implying that in the γ-ray band only a very small fraction of the source capability is realized. Similarly, $L_\gamma / L_{Edd} 3.0 \times 10^{-5}$ is for the nearby Cen A and $L_\gamma / L_{Edd} \simeq 9.1 \times 10^{-4}$ for the distant PKS 0625-35 radiogalaxy. For FRIIs and SSRQs $L_\gamma / L_{Edd} = 10^{-3} - 10^{-4}$ and 0.2–0.4, thus the total available power is very efficiently converted to the emission in the γ-ray band. Interestingly, due to the small black hole masses in NLSy1s, $L_\gamma / L_{Edd} = (2 - 4)$ which can be even higher during the flaring periods, similar to blazars, where also such "super-Eddington" regimes (but with larger L_γ / L_{Edd} ratio) are observed (e.g., [145]).

Name	Class	d_L Mpc	Γ	F_γ $(>100MeV)$ $(10^{-9} ph\, cm^{-2}\, s^{-1})$	L_γ $(erg\, s^{-1})$	σ	E_{max} GeV	time MJD
3C 264	FRI	3.8	2.09 ± 0.14	3.48 ± 1.26	3.71×10^{42}	9.1	97.2	56452.9
NGC 1275	FRI	189.6	2.10 ± 0.01	342.4 ± 3.29	2.33×10^{44}	267.4	221. 5	55402.4
3C 120	FRI	55.9	2.73 ± 0.06	36.3 ± 4.95	3.47×10^{43}	18.3	4.81	56838.1
Cen A Core	FRI	18.4	2.68 ± 0.02	164.9 ± 2.86	1.12×10^{41}	82.4	111.0	55018.5
NGC 2484	FRI	107.9	2.21 ± 0.21	2.49 ± 1.24	8.13×10^{42}	5.6	39.7	54977.4
Cen B	FRI	125.5	2.49 ± 0.04	65.9 ± 5.09	1.18×10^{43}	18.7	66.2	55044.84
M87	FRI	89.6	2.01 ± 0.04	15.9 ± 1.26	8.00×10^{41}	32.2	258.8	55658.0
NGC 6251	FRI	243.7	2.36 ± 0.04	25.3 ± 1.57	2.02×10^{43}	32.0	8.717	56858.0
NGC 1218	FRI	215.5	2.04 ± 0.07	6.67 ± 1.22	1.42×10^{43}	13.5	14.9	55664.4
TXS 0331+3915	FRI	668.0	1.84 ± 0.17	1.49 ± 0.80	3.10×10^{42}	6.6 4	6.3	55870.7
PKS 0625-35	FRI	154.3	1.89 ± 0.04	11.4 ± 1.14	1.48×10^{44}	30.6	107.9	57000.3
3C 111	FRII	4120.2	2.76 ± 0.06	44.29 ± 3.24	9.09×10^{43}	16.8	6.72	56676.3
3C 303	FRII	–	2.04 ± 0.19	1.44 ± 0.75	8.75×10^{43}	5.2	4.49	56274.9
Pictor A	FRII	3215.	2.54 ± 0.14	12.19 ± 3.36	1.56×10^{43}	11.0	25.4	54948.8
3C 207	SSRQ	1	2.66 ± 0.09	14.06 ± 1.79	1.15×10^{46}	11.5	6.0	54783.4
3C 221[6]	SSRQ	4203.	2.44 ± 0.09	8.64 ± 1.49	–	11.2	3.43	56094.1
3C 275.1	SSRQ	2	2.48 ± 0.12	10.03 ± 2.06	6.02×10^{45}	10.5	6.71	56722.4
3C 380	SSRQ	3737.	2.43 ± 0.03	37.39 ± 1.88	4.08×10^{46}	36.2	66.7	55463.4
PKS 1203+04	SSRQ	6	2.85 ± 0.18	9.89 ± 2.38	5.75×10^{45}	6.3	3.38	54961.0
3C 286	SSRQ	5409.	2.71 ± 0.12	11.04 ± 1.85	1.49×10^{46}	8.6	3.56	55038.6
4C +39.23B	CSS	8	2.48 ± 0.06	19.11 ± 1.95	7.77×10^{46}	20.5	9.87	55543.0
1H 0323+342	NLSy1	8370.	2.86 ± 0.04	72.63 ± 2.82	2.25×10^{44}	35.9	3.06	56147.0
SBS 0846+513	NLSy1	8	2.26 ± 0.02	41.78 ± 1.60	4.02×10^{46}	56.2	16.5	56443.5
PMN J0948+0022	NLSy1	273.5	2.64 ± 0.02	136.5 ± 2.78	7.85×10^{46}	78.3	4.78	56483.8
PKS 1502+036	NLSy1	3423.7	2.67 ± 0.04	47.93 ± 2.40	1.13×1046	31.4	4.62	56765.7
PKS 2004-447	NLSy1	3426.	2.63 ± 0.05	25.33 ± 1.89	1.81×10^{45}	19.1	7.97	54761.7

Table 2.2: Results of the Fermi-LAT observation of non-blazar AGNs from August 4 2008 to August 4 2015.

For FRIIs and SSRQs $L_\gamma/L_{Edd} = 10^{-3} - 10^{-4}$ and 0.2–0.4, thus the total available power is very efficiently converted to the emission in the γ-ray band. Interestingly, due to the small black hole masses in NLSy1s, $L_\gamma/L_{Edd} = (2 - 4)$ which can be even higher during the

[6] No red shift found

flaring periods, similar to blazars, where also such "super-Eddington" regimes (but with larger L_γ/L_{Edd} ratio) are observed (e.g., [145]).

The highest energy of the events with higher probability of being associated with the sources and having less angular separation and their detection times, computed using the *gtsrcprob* tool, are presented in Table 2.2. The highest-energy photons of 258.8, 221.5, 111.0 and 107.9 GeV were detected from M87, NGC 1275, Cen A and PKS 0625-35, respectively. Except Cen A, all the other sources have comparably hard photon indexes, so their spectra extend to HEs allowing to detect photons above 100 GeV.

2.5 Discussion

The γ-ray spectra of most of the sources studied here are described significantly better by a PL. However, the γ-ray spectra of some bright sources have been detected with a higher significance show a tendency of a cutoff/break above 1 GeV. In addition, non-blazar AGNs variability studies can shed light on the physical processes in action, such as particle acceleration and emission mechanisms, origin of brightening (s) and the structure and location of the emission region (s). Below, the non-blazar AGNs detected by Fermi-LAT are discussed individually or by each set of objects that behave in a similar fashion. The spectra and light curves are presented in Figs. 2.2 and 2.3 and the main parameters are in Tables 2.2 and 2.3.

NGC 1275: The γ-ray spectrum is shown in Fig. 2.2 (a). The spectrum starts to steepen around $\simeq (1-10)\,GeV$ and more complex log-parabola and power-law with exponential cut-off models are used to fit the data. The log likelihood ratio test shows that the power-law with exponential cut-off modeling when $\beta = 0.43 \pm 0.04$ is preferred over the simple power-law with a significance of 5.8σ. This model is shown with red color in Fig. 2.2 (a) together with log-parabola (blue) and power-law with exponential cut-off (β = 1, orange) models. Among the considered sources, NGC 1275 is unique, where the flux variation in time scales as short as a day can be investigated. The light curve with normal (7-day) and adaptive time binning (assuming 20% uncertainty) is shown in Fig. 2.2.3 (a) with blue and red colors, respectively. The γ-ray light curve appears to be quite a complex one, with many peaks and

flaring periods. The adaptively binned light curve shows that in the active states the required uncertainty is reached on sub-day scales, which once again confirms the short-scale variability of this source. Also, after MJD 56000 (2012) the source was mostly in a bright state, which resulted in the increase of the average flux (Fig. 2.2.3 [a]).

3C 120: The light curve with 90-day binning (see the insert in Fig. 2.2.3 [b]) shows that up to MJD 56900 the source flux is below the Fermi-LAT sensitivity threshold and is mostly undetectable (only upper limits). Afterwards, the γ-ray flux increased being detected by Fermi-LAT almost all the time. More dramatic changes in shorter time scales can be seen on the adaptively binned light curve shown in Fig. 2.2.3 (b) (red data). The data collected from MJD 54682 (4 August 2008) up to MJD 56919.31 (19 September 2014) are necessary to reach the 20% uncertainty in the first bin, while it took shorter time afterwards. The most dramatic increase in the γ-ray flux was observed on April 24, 2015 when within 19.0 min the flux reached $(7.46 \pm 1.56) \times 10^{-6}\, photon\, cm^{-2}\, s^{-1}$ with $\Gamma = 2.29 \pm 0.21$ and 11.2σ detection significance. Then the flux slowly decreased and the data collected within 10 to 35 days were enough to reach 20% uncertainty.

Cen A core: The changes observed in the γ-ray spectrum are shown in Fig. 2.2 [b]. The presence of the unusual break [50] is confirmed using the Fermi-LAT data accumulated for a longer period. In the energy range of 0.1-300 GeV, the broken power-law with the break energy 2.35 ± 0.08 GeV is preferred over the power-law at $\simeq 5.0\sigma$ level. The energy range of 0.1-300 GeV was divided into (0.10-2.35) GeV and (2.35-300) GeV subintervals and the likelihood analyses were re-run. The first component with $\Gamma = 2.75 \pm 0.02$ and a photon flux of $(1.62 \pm 0.04) \times 10^{-7}\, photon\, cm^{-2}\, s^{-1}$ is detected with 71.5σ and shown with black color in Fig. 2.2 (b) while the red line shows the second component with $\Gamma = 2.31 \pm 0.1$ and $(9.16 \pm 0.68) \times 10^{-10}\, photon\, cm^{-2}\, s^{-1}$ detected with 25.7σ. This break is unusual in that the spectrum gets harder instead of getting softer, while typically the opposite occurs. This is a unique case and has never been yet observed in the γ-ray spectra of other AGNs. This hardening could be caused by the contribution of an additional HE component beyond the common SSC jet emission.

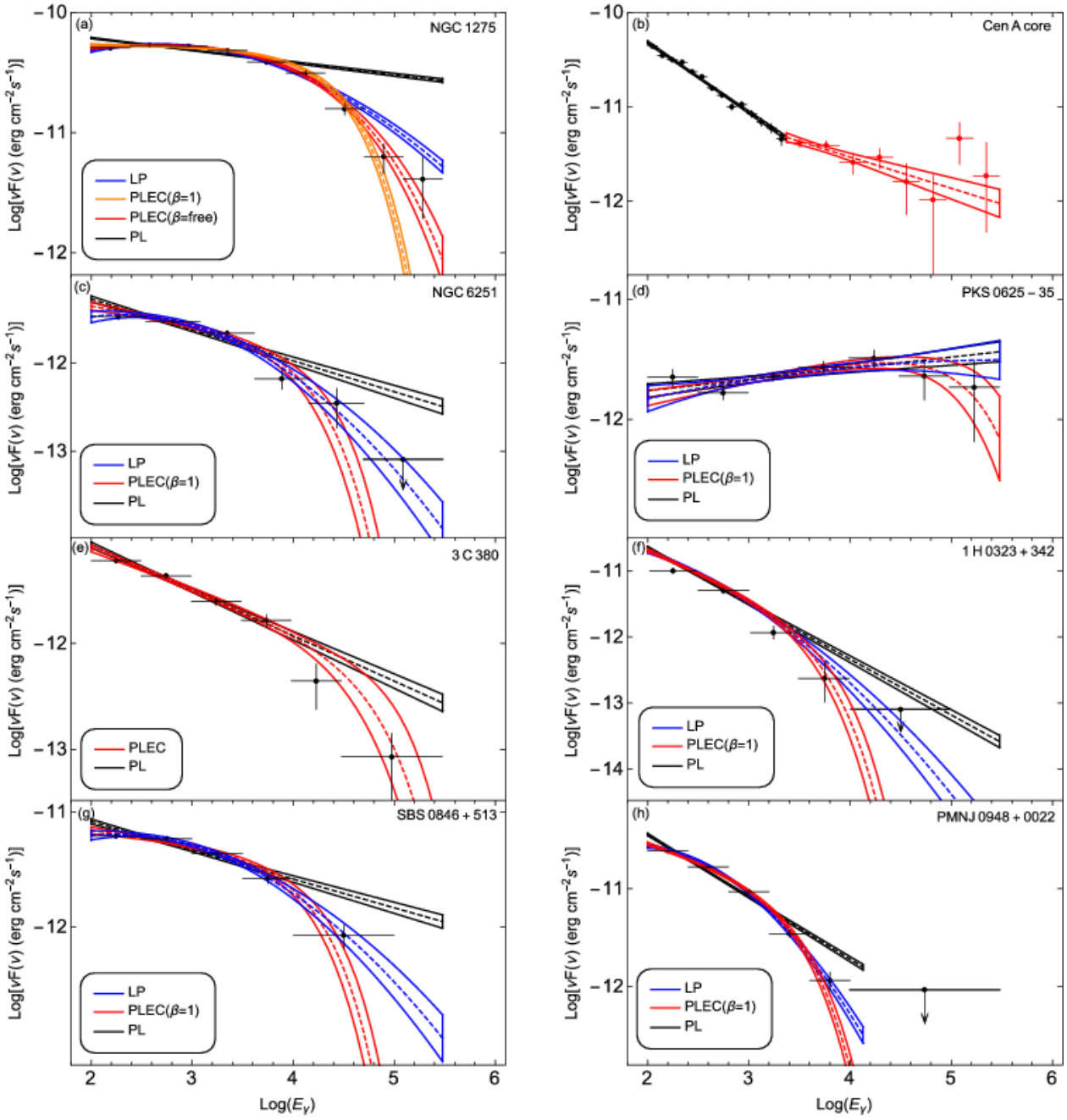

Figure 2.2: Spectra of NGC 1275, Cen A core, NGC 6251, PKS 0625-35, 3C 380, SBS 0846+513, 1H 0323+342 and PMN J0948+0022 measured in the energy range from 100 MeV to 300 GeV, which showed deviation from the simple power-law model above several GeV (see the text). The best fit models obtained with gtlike are depicted together with spectral points which have been obtained by separately running gtlike for smaller energy intervals. The corresponding parameters are given in Table 2.2.

NGC 6251: Detected with 32.0σ, its spectrum extends up to $\simeq (60-70)$ GeV, but the power-law model fails to explain the γ-ray data above 1 GeV. The results of fitting with

alternative models, log-parabola (blue) and power-law with exponential cut-off (β = 1, red), are shown in Fig. 2.2 (c). The data are better explained by log-parabola with $\alpha = 2.29 \pm 0.05$ and $\beta = 0.10 \pm 0.03$. Among the considered radiogalaxies, only the spectrum of NGC 6251 is described by LP, indicating that perhaps a different process is responsible for the particle acceleration. As shown by [142], the γ-ray spectra well described by the log-parabola are formed when the jet electrons are accelerated stochastically. Instead, the power-law with exponential cut-off is formed within diffuse shock acceleration theories and can be interpreted as the emission from accelerated particles, where the cut-off is due to i) escape of the highest energy particles, ii) limitation of the acceleration processes or iii) radiation losses.

Name	Model	α	β	E_{cut} GeV	$F_{>100\ MeV}$ $10^{-8}\ ph\ cm^{-2}s^{-1}$	$2(\Delta\mathcal{L})$
NGC 1275	PLEC	1.86 ± 0.03	0.43 ± 0.04	6.24 ± 2.30	31.84 ± 0.38	34.1
NGC 6251	LP	2.29 ±0.05	0.1 ± 0.03	-	2.10 ± 0.19	16.2
PKS 0625-354	PLEC	1.83 ± 0.06	1	131.2 ± 88.04	1.04 ± 0.13	4.0
3C 380	PLEC	2.36 ±0.05	1	55.57 ± 50.74	3.21 ± 0.19	2.0
1H 0323+342	LP	2.74 ± 0.06	0.09 ± 0.04	-	7.03 ± 0.30	9.6
SBS 0846+513	LP	2.15 ± 0.03	0.09 ± 0.02	-	3.21 ± 0.18	25.8
PMN J0948+0022	LP	2.41 ± 0.02	0.16 ± 0.01	-	12.75 ± 0.02	95.2

Table 2.3: The parameters obtained from the fitting with log-parabola (LP) or power-law with exponential cut-off (PLEC) models.

PKS 0625-25: This is one of the radiogalaxies detected in the VHE γ-ray band [146]. Its γ-ray photon index, $\Gamma = 1.89 \pm 0.04$, is unusually harder as compared with those of other radiogalaxies. Around 100 GeV, there is a hint of substantial deviation from power-law (black curve in Fig. 2.2 [d]), but the power-law with exponential cut-off model with $\Gamma = 1.83 \pm 0.06$ and $E_{cut} = 131.2 \pm 88.04$ GeV (Fig. 2.2 [d], red curve) is preferred over the simple power-law only at the $\sim 2\sigma$ level, so that the power-law can't be rejected. However, the spectrum of PKS 0625-35 in the TeV band is softer, $\Gamma_{TeV} = 2.8 \pm 0.5$ [146], which

strengthens the assumptions of the cutoff in the GeV band. This source was separately studied using broadband data, which was published in [147] and described in chapter 4.

3C 380: Its γ-ray spectrum can be described by power-law with $\Gamma = 2.43 \pm 0.03$ detected with $\approx 36.2\sigma$ and its emission extends up to 300 GeV (Fig. 2.2 [e]). We note an indication of deviation of the power-law with respect to the data above 10s of GeV, but the power-law with exponential cut-off modeling with $\Gamma = 2.36 \pm 0.05$ and $E_c = (55.57 \pm 50.74)$ GeV (Fig. 2.2 (e) red color) is preferred over power-law only at the level of $\sim$ 1.4σ. Its γ-ray emission is variable in 30-day scales but the adaptively binned light curve shows that sometimes the flux increases also in short periods: for example on MJD 55184.71 within 21.3 days the flux increased up to $(8.45 \pm 1.37) \times 10^{-8}\, photon\, cm^{-2}\, s^{-1}$.

Noticeably different spectral and temporal properties are observed for NLSy1s analyzed here. The spectra of PKS 1502+036 and PKS 2004-447 were better described by power-law with steep, $\Gamma = 2.67 \pm 0.04$ and $\Gamma = 2.63 \pm 0.05$ photon indexes, respectively. Their emissions are variable in long (e.g., 45- and 60-day) time scales and the spectra extends up to 10–30 GeV. Instead, the γ-ray emission of 1H 0323+342, SBS 0846+513 and PMN J0948+0022 significantly increases in day- or a few-days scales [18, 19, 148]. With the help of the light curves generated by the adaptive binning method, we report on flux variations and spectral changes in shorter time scales.

1H 0323+342: Its spectrum is steep ($\Gamma = 2.86 \pm 0.04$) and the γ-rays are detected up to 10 GeV. There is a marginal evidence of a spectral curvature around 1 GeV (Fig. 2.2 (f) black curve) and both log-parabola or power-law with exponential cut-off (β = 1) models can better explain the observed data (blue and red curves in Fig. 2.2 (f), respectively). However, because of low statistics ($\sim 3.1\sigma$) power-law modeling cannot be excluded. For most of the time, the γ-ray flux of 1H 0323+342 did not much exceed the value averaged over the whole observational time (blue data in Fig. 2.2.3 [c]). The adaptively binned light curve calculated for 15% uncertainty shows several periods when the flux significantly increased (Fig. 2.2.3 [c] red data). The most significant increase was observed on MJD 56534.3 when within 16.2 hours the flux was as high as $(1.98 \pm 0.31) \times 10^{-6}\, photon\, cm^{-2}\, s^{-1}$ and the photon index hardened to $\Gamma = 2.22 \pm 0.15$. During this flare, the flux-doubling time was as

short as 0.49 days, implying the emission is produced in a very compact region, $\simeq 1.2 \times 10^{15} \times \delta\, cm$ [149]. After this rapid flare, the source again entered its quiescent state.

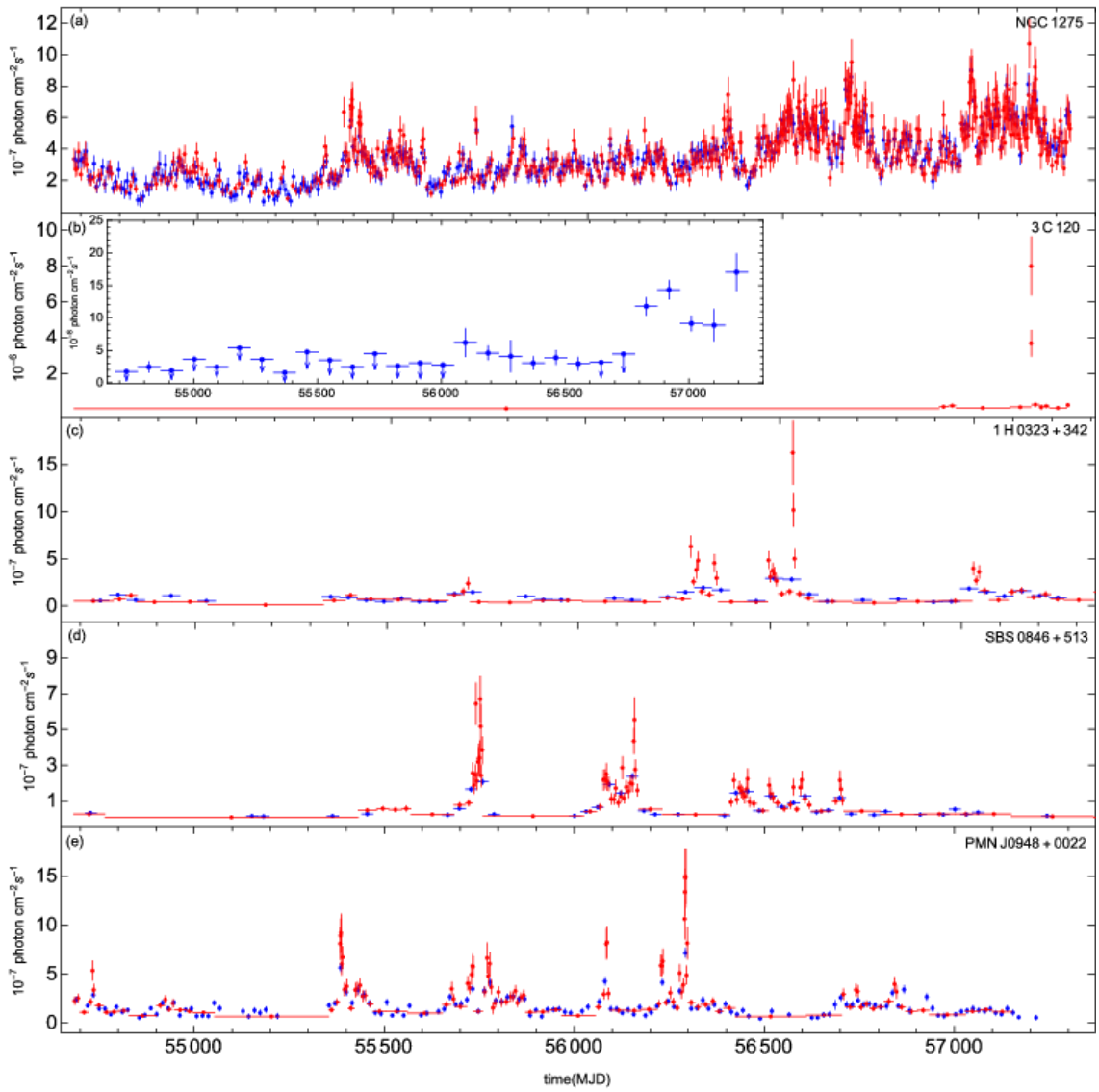

Figure 2.3: Light curves of NGC 1275, 3C 120, 1H 0323+342, SBS 0846+513 and PMN J0948+0022. The light curves are calculated with standard gtlike tool for normal (blue) and adaptively binned (red) time scales.

PMN J0948+0022: Its spectrum measured in the narrow 0.1-10 GeV range appeared with a significant curvature Fig. 2.2 (h). The comparison of log-parabola and power-law models yields a log likelihood ratio of 95.2, so the power-law modeling can be rejected with a significance of 9.76σ. The log-parabola model compared with the observed spectrum is shown in Fig. 2.2 (h) with blue color (for parameters see Table 2). The γ-ray light curve with

15-day (blue) and adaptive bins (red, 20%) shows that the source is alternatingly in its flaring or quiescent states (Fig. 2.2.3 [e]). Several times, the source flux was above $10^{-6}\, photon\, cm^{-2}\, s^{-1}$ and during an extremely active state from MJD 56290.96 to MJD 56294.60, it reached a peak flux of $(1.51 \pm 0.31) \times 10^{-6}\, photon\, cm^{-2}\, s^{-1}$ within 18.9 hrs, corresponding to an apparent isotropic γ-ray luminosity of $L_\gamma \approx 1.09 \times 10^{48}\, erg\, s^{-1}$, which is typical for the brightest FSRQs. For most of the time the photon index is > 2.5, where the hardest one is $\Gamma = 2.13 \pm 0.18$. The observed rapid flux changes in intra-day scales and the amplitude of the increase once more show that in the γ-ray band NLSy1s behave similar to blazars.

SBS 0846+513: Below $\simeq 10 GeV$ the spectrum can be well described by a power-law (black curve in Fig. 2.2 [g]) with $\Gamma = 2.26 \pm 0.02$ which is the hardest photon index obtained for the selected NLSY1s. At higher energies, the power-law model over predicts the observed data (blue line in Fig. 2.2 [g]) suggesting a turn-over in the spectrum. Indeed, at 5.1σ the log-parabola with $\alpha = 2.15 \pm 0.03$ and $\beta = 0.09 \pm 0.02$ explains the data statistically better. A sequence of flares can be identified on the γ-ray light curve of SBS 0846+51 with 30-day (blue) and adaptive bins (red, 20%) shown in Fig. 2.2.3 [d], though with a lower amplitude as compared with the flares of 1H 0323+342. The highest flux of $(6.35 \pm 1.12) \times 10^{-7}\, photon\, cm^{-2}\, s^{-1}$ was observed on MJD 56145.6 and the active state lasted till MJD 56146.8, when within 19.6 hours the flux was $(4.15 \pm 1.04) \times 10^{-7}\, photon\, cm^{-2}\, s^{-1}$, but the photon index was significantly hard 1.73 ± 0.14. This is the hardest γ-ray photon index detected during the considered seven years and, interestingly, the highest-energy 16.5 GeV photon had been also observed during this period. This hardening is most likely associated with the emission from the re-accelerated or fresh electrons which produced also the observed highest-energy photon.

PKS 1502+036 and PKS 2004-447: The spectra of these NLSy1s were described by power-law model with $\Gamma = 2.67 \pm 70.04$ and $\Gamma = 2.63 \pm 30.05$ photon indexes respectively. A calculation showed a flux variability only within longer 45- and 60-day. The adaptive light curve of these sources did not showed considerable increase of the flux during the time,

although due to the bad statistics the adaptive bins were enough longer not allowing to study the variation in shorter time scales.

Sources with long time variability: The γ-ray emission from some sources varies within longer time periods as compared with NGC 1275 and 3C 120. For example, the low energy component of Cen A core emission is variable within 45 days which confirms the marginal evidence reported in [50]. In the second emission component, there is an indication (at the limit) of a year and half-year scale variability, but because of limited statistics, however, no definite conclusion can be drawn. There is a hint of variability in the γ-ray light curves of M87 and PKS 0625-35 with 60-day binning but the statistics does not allow neither to confirm nor explore it in shorter time scales. The previous observations of M87 in the HE and VHE γ-ray bands have already suggested that it is in its quiescent state [42, 150], while being active and repeatedly in the flaring state in 2005 [151]. Interestingly, these sources are also the ones which have been detected in the VHE γ-ray band so far [88].

FRIIs, SSRQs and CSS. Among these sources 3C 111, 3C 207, 3C 275.1, 3C 380 and 4C+39.23B are variable. The variability of 3C 111 is highly significant in the light curve with 60-day binning. For 3C 207 and 3C 275.1, the significance is still not high enough to confirm the variability in short time scales, but the γ-ray emission is variable within a year. For 4C +39.23B, in the light curves with 90-day and 60-day binning, the periods when the source was and was not detected by Fermi-LAT are comparable, therefore no definite conclusion can be made but the γ-ray emission is variable within a half-year period. Nevertheless, a short time scale activity around 21 April 2011 was observed, when within 29.4 days the flux was $(4.39 \pm 0.85) \times 10^{-8}\, photon\, cm^{-2}\, s^{-1}$ (as inferred from the adaptively binned light curve). The significance is still not high enough to search for γ-ray variability in the other sources studied here. It is interesting to highlight Cen B and NGC 6251 where the γ-ray emission is detected with high 18.5σ and 31.6σ significances, respectively. The constant flux assumption can't be rejected when using light curves with short (few months) or long times scales (half-year/year). Although this does not allow to rule out possible variability completely, this is interesting, since both have large scale structures,

$\sim$ 380 kpc for Cen B [76] and ~ 1.8 Mpc for NGC 6251 [92], and in principle, the γ-rays can be produced in these regions.

2.6 Summary

The γ-ray emission from non-blazar AGNs included in the third catalog of AGNs detected by Fermi-LAT is investigated using the Fermi-LAT data accumulated in 2008-2015. The sample consists of eleven FRI, three FRII, six SSRQ, one CSS and five NLSy1 sources. We obtained the following results:

i) The γ-ray photon index of non-blazar AGNs changes within 1.84–2.86. The hardest photon indexes of $\Gamma = 1.84 \pm 0.17$ and $\Gamma = 1.89 \pm 0.04$ were obtained for TXS 0331+3915 and PKS 0625-35, respectively, and the softest for 1H 0323+342, $\Gamma = 2.86 \pm 0.04$. The measured faintest flux is of the order of a few times $10^{-9}\, photon\, cm^{-2}\, s^{-1}$, while the flux from bright sources exceeds $10^{-7}\, photon\, cm^{-2}\, s^{-1}$. The farthest non-blazar AGN detected by Fermi-LAT is 4C +39.23B at $z \simeq 1.21$ with a γ-ray flux of $(1.91 \pm 0.19) \times 10^{-8}\, photon\, cm^{-2}\, s^{-1}$.

ii) In the $\Gamma - F_\gamma$ plane, the FRIs have a harder γ-ray photon index with $\Gamma_m \simeq 2.22$ and a flux ranging from $\simeq 1.5 \times 10^{-9}\, photon\, cm^{-2}\, s^{-1}$ to $3.6 \times 10^{-8}\, photon\, cm^{-2}\, s^{-1}$. The mean photon index of FRIIs/SSRQs shifts to a higher value of $\Gamma_m \simeq 2.58$ (i.e., softer spectra) and the flux to the range of $(0.9 - 4) \times 10^{-7}$ photon cm^{-2} s^{-1}. With a γ-ray flux of $\geq 10^{-7}$ photon cm^{-2} s^{-1}, the average photon index of NLSYs is similar to that of FRIIs/SSRQs with $\Gamma > 2.3$.

iii) In the $\Gamma - L_\gamma$ plane we confirm the previous results from the analysis of a smaller sample of non-blazar AGNs. The γ-ray luminosity of most of FRIs is $L_\gamma < 3 \times 10^{44}$ erg s^{-1} with $\Gamma < 2.3$ while for FRII $L_\gamma > 3 \times 10^{44}$ erg s^{-1} but $\Gamma > 2.3$. SSRQs and NLSy1s occupy the area beyond $\Gamma > 2.3$ and $L_\gamma > 3 \times 10^{45}$ erg s^{-1}, which is more typical for FSRQs, and are clearly separated from FRIs and FRIIs. The ratio of apparent γ-ray luminosity to the Eddington accretion power is different for each class of objects considered here. This ratio

is usually very small for FRIs ($< 10^{-4}$), increasing for FRIIs/SSRQs ($10^{-3} - 10^{-2}$), and exceeding unity for NLSy1s.

iv) The γ-ray spectra of most of the sources studied here are described significantly better by a PL. The spectra of NGC 1275, NGC 6251, SBS 0846+513 and PMN J0948+0022 deviate from power-law significantly. The spectra of NGC 6251, SBS 0846+513 and PMN J0948+0022 are better modeled with log-parabola while the curvature in the γ-ray spectra of NGC 1275 can be better described using power-law with exponential cut-off (β free). There is a hint of possible cutoff in the spectra of 3C 380, PKS 0625-35 and 1H 0323+342, though the current data does not allow us to reject the power-law model. The unusual break in the spectrum of Cen A is confirmed, which shows that below and above $2.35 \pm 0.08\,\mathrm{GeV}$, the photon index is $\Gamma = 2.75 \pm 0.02$ and 2.31 ± 0.1, respectively.

v) New sources having variable γ-ray emission have been identified. Apart rapid and strong variability of NGC 1275 and 3C 120, periods of strong flux increase and short time scale variability are found for 1H 0323+342, SBS 0846+513 and PMN J0948+0022, using the light curves generated with an adaptive binning method. The γ-ray emissions from 3C 380, 3C 111, Cen A core (low energy component), PKS 1502+036 and PKS 2004-447 vary within months, and there is an indication (at the threshold limit) of variability of the flux of PKS 0625-35 and M87. The γ-ray flux of 3C 207, 3C 275.1 and 4C +39.23B varies within half-year or one-year periods. Notable is the absence of γ-ray variability of Cen B and NGC 6251, which appeared to have been detected with a significance of 18.5σ and 31.6σ, respectively.

vi) The γ-ray emission from NLSy1s with their flares and peculiar multiwavelength properties make them more similar to blazars. The γ-ray emission is variable, showing flares in short time scales along with a moderate hardening of their spectra. For example, on MJD 56146.8 SBS 0846+513 was in its high state with a flux of $(4.15 \pm 1.04) \times 10^{-7}\,\mathrm{photon\,cm^{-2}\,s^{-1}}$ with a significantly hard photon index of 1.73 ± 0.14. During the active state of PMN J0948+0022 from MJD 56290.96 to MJD 56294.60, the peak γ-ray flux was $(1.51 \pm 0.31) \times 10^{-6}\,\mathrm{photon\,cm^{-2}\,s^{-1}}$ within 18.9 hrs, which corresponds to an apparent isotropic γ-ray luminosity of $\mathrm{L_\gamma} \approx 1.09 \times 10^{48}\,\mathrm{erg\,s^{-1}}$.

Chapter 3

3. γ-RAY VARIABILITY OF NGC 1275

3.1 Introduction

Due to its proximity ($z = 0.0176$, ≈ 75.6 Mpc) and brightness, the radiogalaxy NGC 1275 has been a target for observations in almost all energy bands. Core-dominated asymmetrical jets at both kpc [152] and pc scales [153] have been detected in the radio band with characteristics more similar to those of Fanaroff and Riley type 1 sources [2]. The emission in the X-ray band is mostly dominated by the thermal emission from the cluster, although a non-thermal component in the energy range 0.5-10 keV with a photon index of $\Gamma_X \simeq 1.65$ has been observed [154]. High Energy (HE; > 100 MeV) γ-rays from NGC 1275 had already been detected by Fermi-LAT using the data obtained during the first 4 months of observations [42]. Then, using the data accumulated for longer periods γ-ray flux and photon index variation on month timescales were detected [48]. However, the γ-ray emission is variable also in shorter (a few days) time scales [155]. Very High Energy (VHE; >100 GeV) γ-ray emission with a steep spectral index of 4.1 ± 0.7 was detected by MAGIC, using the data accumulated between August 2010 and February 2011 [156]. No hints of variability above 100 GeV were seen on month time scales.

Even, if the observed γ-ray variability allowed to exclude Perseus cluster as the main source of γ-ray emission, the exact mechanisms responsible for the broadband emission from NGC 1275 are still unclear. The multiwavelength Spectral Energy Distribution (SED) hints at a double-peaked SED with the peaks around 10^{14} Hz and $(10^{23} - 10^{24})$ Hz [157]. Within a "classical" misaligned BL Lac scenario, a one-zone synchrotron/Synchrotron Self Compton (SSC) interpretation of the SED can well explain the HE peak constrained by Fermi-LAT and MAGIC data but has difficulties explaining the low energy data. It requires that the jet should be more aligned than it is estimated, e.g., $30° - 55°$ [158]. Therefore, additional assumptions on the jet properties and/or more complex scenarios for inverse-Compton scattering should be made.

In the HE γ-ray band frequently flaring activities are known for NGC 1275 [159]. A substantial increase of the γ-ray flux in the HE and VHE γ-ray bands was detected in October 2015 and January 2017 [160, 161, 162]. In October 25, 2015 Fermi-LAT detected a bright flare with a daily peak flux of $(1.6 \pm 0.2) \times 10^{-6} photon\, cm^{-2}\, s^{-1}$ [160]. Then, in the night between 31 December 2016 and 01 January 2017 a major flare was detected in the VHE γ-ray band when the flux was 60 times higher than the mean flux [161]. Also the flux >100 MeV was about 12 times higher than the most significant flux observed with AGILE [162]. Besides, Swift observations during this major γ-ray active period provided data in the UV and X-ray bands and so giving a unique chance to investigate the flaring activity of NGC 1275 in the multiwavelength context.

The goal of the current study is to have a new look on the γ-ray emission from NGC 1275 (the btightest radiogalaxy in the GeV band) in the last ~ 8.7 years in general and during the major flaring periods in particular. The larger data set allows to investigate the γ-ray flux evolution in time with improved statistics in shorter time scales, while a detailed analysis of recently observed exceptional flares will allow to have an insight into the particle acceleration and emission processes.

3.2 Fermi-LAT observation and Data Analysis

Data reduction and analysis. For the current study, publicly available data accumulated during the last ~8.7 years of Fermi-LAT operation (from August 4, 2008 to March 15, 2017) are analyzed with the standard Fermi Science Tools v10r0p5 software package with the same principle as described in section 1.4.1. In the analysis we selected different radii $(9°, 10°, 12°$ and $15°)$ of the ROI to ensure that the selected ROI is an accurate representation of the observation. This yielded essentially the same results within statistical uncertainties, so a radius of $12°$ was used and the photons from a $16.9° \times 16.9°$ square region centered at the location of NGC 1275, (RA, dec) = (49.96, 41.51), were downloaded. As in 3FGL, the γ-ray spectrum of NGC 1275 was modeled using a log-parabolic spectrum:

$$\frac{dN}{dE} = N_0 \left(\frac{E_\gamma}{E_0}\right)^{-\alpha-\beta log\ (E_\gamma/E_b)} \tag{3.1}$$

where N_0 is the normalization, α is the photon index at E_b energy, which is fixed during the analysis and β represents the curvature of the spectra.

Using of the data accumulated for an almost 2 times longer period than in 3FGL, can result in new γ-ray sources in the ROI which are not properly accounted for in the model file. In order to probe for additional sources, a TS map of the ROI is created with *gttsmap* tool using the best-fit model of 0.1-500 GeV events. To identify the coordinates of the excess hot spots with TS>25 (5σ), we used the find source iterative source-finding algorithm implemented in *Fermipy*. In the TS map it identifies the peaks with TS > 25 and adds a source at each peak starting from the highest TS peak. The sources position is obtained by fitting a 2D parabola to the log-likelihood surface around the maximum. Alternatively, the sources position was calculated by hand using the pixels surrounding the highest TS (similar to the method used in [163]. Both methods resulted in similar values. For each given point we sequentially added a new point source with a conventional spectral definition (power-law) and performed binned likelihood analysis with *gtlike*. For the further analysis we used the model file with the new additional point-like sources to have better representation of the data.

Temporal variability. The γ-ray light curve is calculated using the unbinned likelihood analysis method as described in section 1.4.1 using the events in the energy range of (0.1 – 300) GeV. Different model files are used to ensure that the possible contribution from sources within ROI are properly accounted for. In the model file obtained from the whole-time analysis, the photon indices of all background sources are first fixed to the best guess values in order to reduce the uncertainties in the flux estimations, then those of the sources within ROI are considered as free parameters. In addition, we analyzed the data accumulated during the one-month periods covering the major flares (01-30 October and 15 December 2016-15 January 2017). Then we fixed the spectral parameters of all background sources as in [40]. All approaches yielded essentially the same results. We used the latter model as the rising and decaying times of the first flare can be evaluated better. Given shorter periods are considered, the spectrum of NGC 1275 has been modeled using a power-law function with the index and normalization as free parameters.

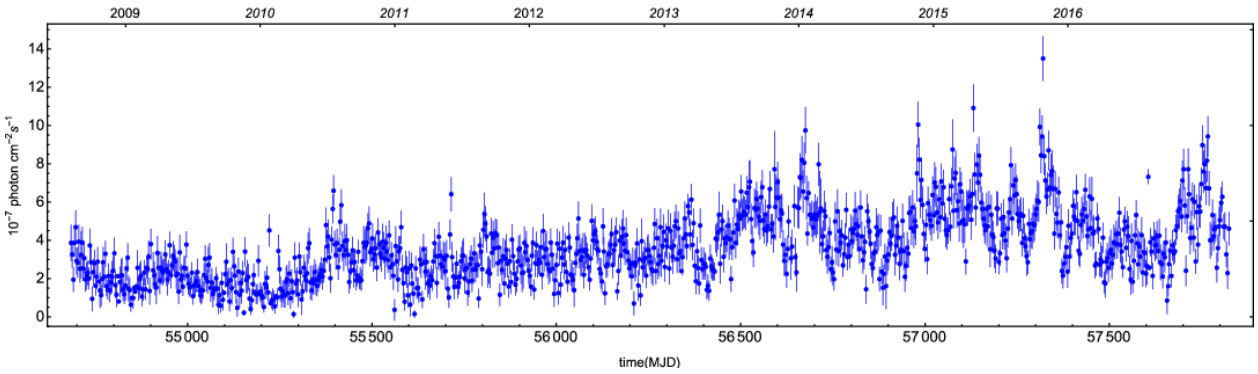

Figure 3.1: The light curve of $0.1 < E < 300$ GeV γ-rays from NGC 1275 from August 4, 2008 to March 5, 2017, with 3-day (blue) binning.

Since no variability is expected for the background diffuse emission, the normalization of both background components is also fixed to the values obtained for the whole time period. Fig. 3.1 shows the γ-ray light curve with three-day bin size. Despite the fact that the flux sometimes exceeded the averaged value presented in 3FGL ($\approx 2.26 \times 10^{-7}\, photons\, cm^{-2}\, s^{-1}$), pronounced flaring activities were detected in October 2015 (hereafter Flare 1 [F1]) and in December 2016/January 2017 (hereafter Flare 2 [F2]). Starting from 22 October 2015 the daily averaged flux of NGC 1275 was above $10^{-6}\, photons\, cm^{-2}\, s^{-1}$ and remained high for 5 days with a daily averaged maximum of $(1.48 \pm 0.20) \times 10^{-6}\, photons\, cm^{-2}\, s^{-1}$ observed on 24 October 2015. Another substantial increase in the γ-ray flux was observed on December 31, 2016 when the flux increased from about $(4 \sim 5) \times 10^{-7}\, photons\, cm^{-2}\, s^{-1}$ to $(2.21 \pm 0.26) \times 10^{-7}\, photons\, cm^{-2}\, s^{-1}$ within a day with a detection significance of $\sim 21.5\sigma$. The photon statistics allowed us to study these flares with denser time sampling (sub-day) for the first time. The shortest bin sizes have been chosen to ensure that i) the flare rise and decay periods are well constrained and ii) the detection significance for each bin exceeds the $\sim 5\sigma$ limit. The statistics allowed to use bins with 8-hour intervals for F1 and 3-hour bins for F2. For example, from MJD 57317 to MJD 57322, the detection significance varied between 5.1σ and 13.1σ, and from MJD 557753 to MJD 57754 it was between 5.3σ and 10.4σ. The corresponding light curves are shown in the lower panels of Fig. 3.2. In order to check if the likelihood fit has converged in each time bin, the plot of $N_{pred}/\sqrt{N_{pred}}$ vs $Flux/\Delta Flux$ is

shown in the lower panels of Fig. 3.2 for 8-hour (left) and 3-hour (right) bins. We verified that the fit has converged in the surrounding bins as well. As one can see, it seems there is a linear correlation without any declination, so the errors are an accurate representation of the observation.

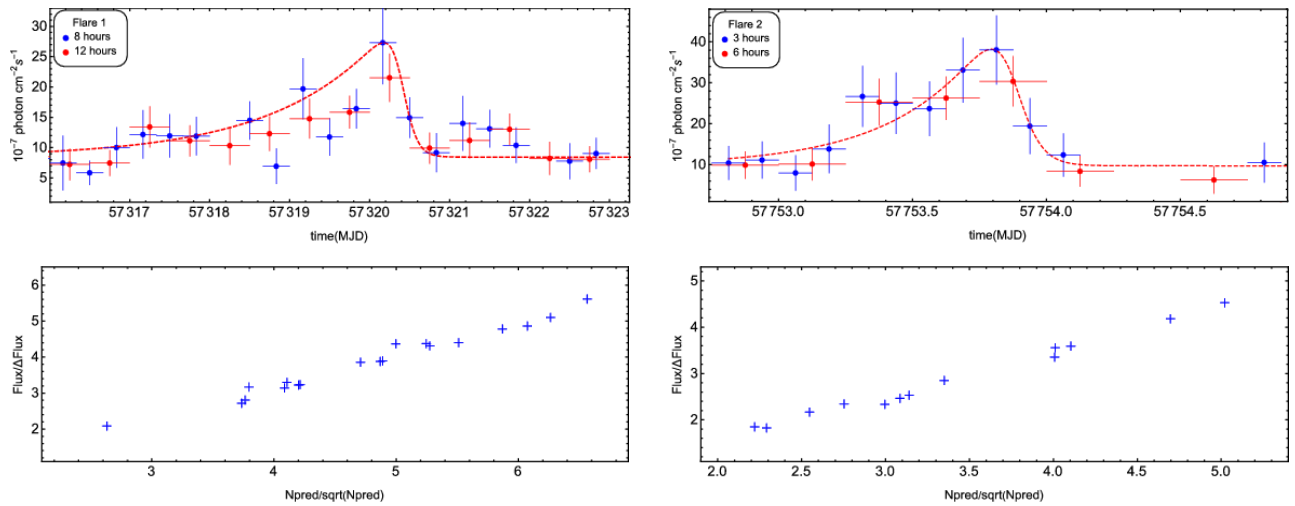

Figure 3.2: Top panels: Sub intervals covering F1 (left) and F2 (right). F1 is shown with 8-hour (blue) and 12-hour (red) time intervals and F2 with 3-hour (blue) and 6-hour (red) bins. The red dashed lines show the fit of F1 and F2 with Eq.1.8. Lower panels: The plot of $N_{pred}/\sqrt{N_{pred}}$ vs $Flux/\Delta Flux$ for 8-hour (left) and 3-hour (right) bins.

Further, the γ-ray flux and photon index variations are investigated using a light curve generated by an adaptive binning method [30] (see Section 1.4.1). In order to reach the necessary relative flux uncertainty, the integral fluxes are computed above the optimal energy [30], which in this case is $E_0 = 208.6$ MeV. Also, in order to improve the accuracy of the method, the flux of bright sources which lie close to NGC 1275 have been taken into account. This is done by providing the parameters of confusing sources during the adaptive binning light curve calculations. The light curve calculated assuming a constant 15% uncertainty is shown in Fig. 3.3 (upper panels) for the period covering the large flares.

Spectral Analysis. The changes in the γ-ray photon index are investigated by analyzing the data from the following four periods:

1. overlapping with the observation of Swift on 30 December 2016. Even if the Swift observations lasted ~960 seconds, in order to increase the statistics, the γ-ray

spectrum has been extracted for the period MJD 57752.75-57753.25 where the source has a comparable flux as revealed from the light curve with a 6-hour binning (Fig. 3.2, upper right panel).

2. MJD 57754.00-57755.75, when the flux is relatively constant and it coincides with the observations of Swift on 01 January 2017.
3. at the peak of F2 (MJD 57753.81), using the data accumulated for 3 hours.
4. MJD 57442.32-57444.45, which corresponds to the quiet (steady) state in the X-ray and γ-ray bands.

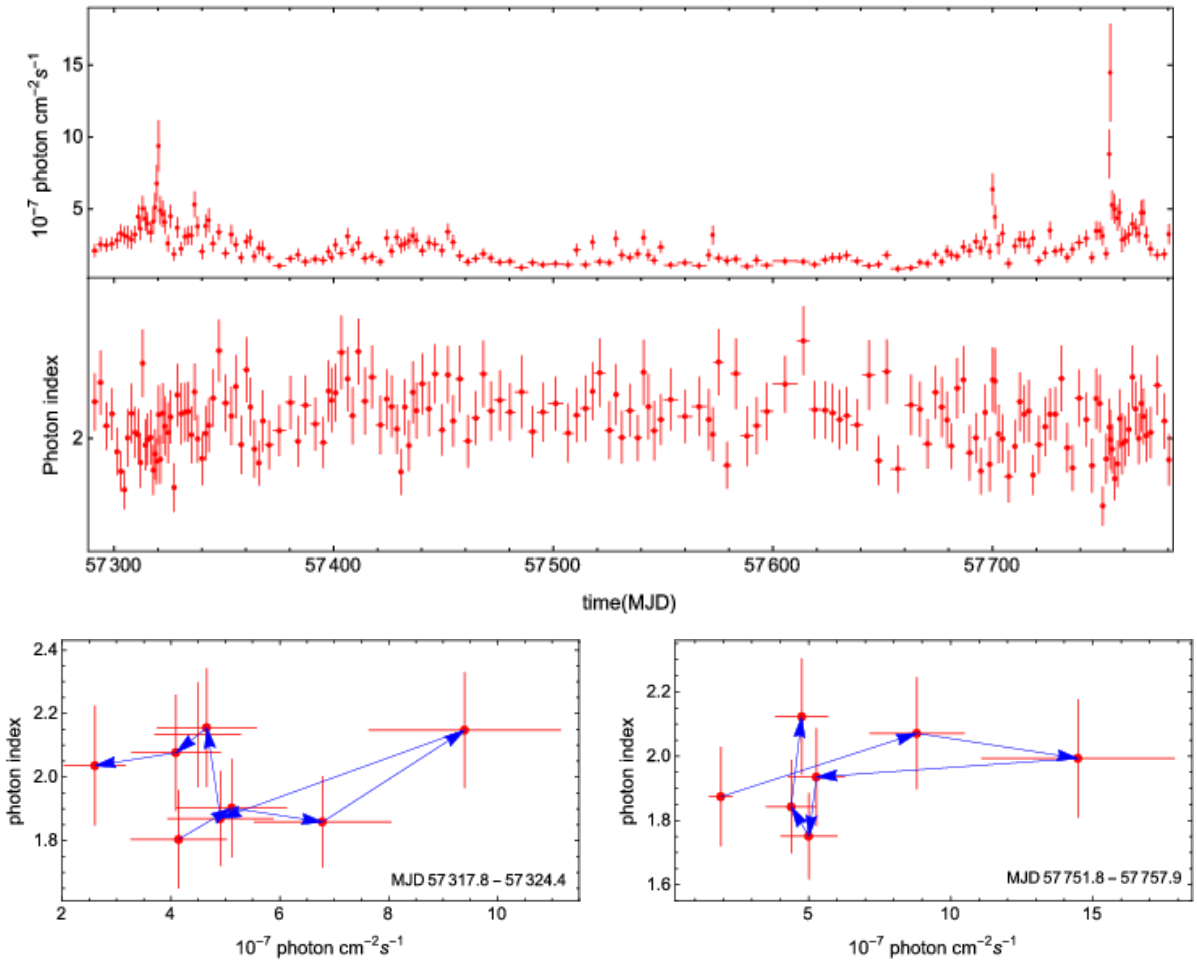

Figure 3.3: Top panels: The upper panel shows the period of major flares with the constant uncertainty (15%) light curve above 208.6 MeV obtained with the adaptive binning method. The lower panel shows the photon index variation during the same period. Bottom panels: The photon index vs. the flux above 208.6 MeV for F1 (left) and F2 (right).

The γ-ray spectrum of NGC 1275 has been modeled using a power-law function ($dN/dE \sim N_0 E^{-\Gamma}$) where the normalization (N_0) and power-law index (Γ) are considered as free parameters. The best matches between the spectral models and events are obtained with an unbinned likelihood analysis implemented in *gtlike*. The spectral fitting results are summarized in Table 3.1. After analyzing the data for each considered period, the SEDs are obtained by freezing the NGC 1275 photon index in the model file and separately running *gtlike* for smaller energy bins of equal width in log scale. The SED for each period is shown in Fig. 3.4. Although some features can be noticed, it is hard to make any conclusion because of large uncertainties in the estimated parameters.

We separately analyze the Fermi-LAT data to determine the energy of the highest energy photon detected from NGC 1275 using *gtsrcprob* tool and the model file obtained from the likelihood fitting. All spectral parameters of the sources within ROI are first fixed to the best fitting values obtained in the whole time analysis and then are left free. Both yielded identical results. In this case, additional care must be taken since IC 310, which is known to be a strong emitter in the VHE γ-ray band [164], is only at a distance of 0.623°. So both sources are considered to estimate the probability whether the photon belongs to NGC 1275 or to IC 310. The highest-energy photons detected during the four periods mentioned above are presented in Table 3.1.

3.3 Swift UVOT/XRT Data Analysis

XRT Data. During the F2 flare Swift made 3 observations, but unfortunately no observation during the F1. In addition to these observations, the Swift data of February 25, 2016, corresponding to a relatively stable state in the X-ray band have been analyzed. The steps of Swift-XRT data analysis is presented in section 1.4.2, but below several parameters related with analyses of NGC 1275 data are presented. The XRT data were analyzed with the XRTDAS software package (v.3.3.0) distributed by HEASARC along with the HEASoft package (v.6.21) (for more detail, please see section 1.4.2). The source region was defined as a circle with a radius of 10.6 pixels ($25''$) at the center of the source, while the

background region as an annulus centered at the source with its inner and outer radii being 20 (47″) and 30 pixels (71″), respectively.

Fermi-LAT					
Period	Date	Flux[a]	Ph. Index[b]	TS	H.P.E.[c] (GeV)
57442.32-57444.45	2016/02 (24-26)	4.18 ± 0.85	1.93 ± 0.14	123	10.39
57752.75-57753.25	2016/12 (30-31)	8.56 ± 2.30	1.79 ± 0.17	106	34.77
57753.81	2016/12 31	34.82 ± 8.67	1.93 ± 0.19	102	5.84
57754.00-57755.75	2017/01 (01-02)	6.27 ± 1.20	1.67 ± 0.11	178	4.18

Swift-XRT					
Obs id	Date	Exp. time	Ph. Index[d]	Unab. Flux[e]	$X^2_{\mathrm{red.}}\,(\mathrm{d.o.f.})$
34380005	2016-02-25	2750	1.52 ± 0.08	3.10 ± 0.19	1.04 (75)
87312001	2016-12-30	939	1.75 ± 0.12	8.64 ± 0.76	0.74 (24)
87311001	2017-01-01	619	1.77 ± 0.17	10.57 ± 1.26	1.15 (15)
31770011	2017-01-01	984	1.77 ± 0.08	10.29 ± 0.55	0.95 (173)

Table 3.1: Parameters of spectral analysis.

Notes:

a) Integrated γ-ray flux in the 0.1 – 100 GeV energy range in units of $10^{-7}\ photon\ cm^{-2}\ s^{-2}$.

b) γ-ray photon index from likelihood analysis.

c) Photon energy in GeV.

d) Photon index from X-ray data analysis.

e) X-ray flux in the energy range 0.3–10 keV in units of $\times\ 10^{-11}\ erg\ cm^{-2}\ s^{-1}$ (corrected for the Galactic absorption).

Such selections allowed minimizing the possible contribution from the cluster emission. For PC mode observations (Obsid 87312001, 87311001), the count rate was above 0.5 count/s, being affected by the piling-up in the inner part of the PSF. This effect was removed, excluding the events within a 4-pixel radius circle centered on the source position. All spectra were re-binned to have at least 20 counts per bin, ignoring the channels with

energy below 0.3 keV and fitted using Xspec v12.9.1a. The results of the fit are presented in Table 3.1.

UVOT Data. In the analysis of Swift-UVOT data, the source counts were extracted from an aperture of $5.0''$ radius around the source. The background counts were taken from the neighboring circular source-free region with a radius of $20''$. The magnitude calculation and correction for Galactic extinction were performed as described in section 1.4.3. The spectra of these observations for each filter are shown in Fig. 3.4.

3.4 Interpretation of the Results

The γ-ray light curve appears to be quite a complex one, with many peaks and flaring periods. The highest fluxes were detected in October 2015 and December 2016/January 2017 when the daily averaged peak γ-ray fluxes $\simeq (1.48 - 2.21) \times 10^{-6}\, photons\, cm^{-2}\, s^{-1}$ integrated above 100 MeV were detected. It reached its maximum of $(3.48 \pm 0.87) \times 10^{-6}\, photons\, cm^{-2}\, s^{-1}$ on December 31, 2016, within 3 hours, which is the highest γ-ray flux observed from NGC 1275 so far; it exceeds the averaged flux by a factor of ~15.4. The apparent isotropic γ-ray luminosity at the peak of the flare, $L_\gamma \simeq 3.84 \times 10^{45}\, erg\, s^{-1}$ (using $d_L = 75.6$ Mpc), exceeds the averaged γ-ray luminosity of other radiogalaxies detected by Fermi-LAT (usually $\leq 10^{45}\, erg\, s^{-1}$ [45]); it is more comparable with the luminosity of BL Lac blazars. This is quite impressive, considering the large Doppler boosting factors of blazars ($\delta \geq 10$) as compared with the value of $\delta \sim (2 - 4)$ usually used for the radiogalaxies. Yet, at $\delta = 4$ the total power emitted in the γ-ray band in the proper frame of the jet would be $L_{em,\gamma} \simeq L_\gamma / 2\delta^2 \simeq 1.2 \times 10^{44}\, erg\, s^{-1}$. It is of the same order as the kinetic energy of the NGC 1275 jet ($L_{jet} \simeq (0.6 - 4.9) \times 10^{44}\, erg\, s^{-1}$) estimated from broad-band SED modeling [43]. This implies that during the discussed flaring period a substantial fraction of the total jet power, ($L_{em,\gamma}/L_{jet} \leq 1$), is converted into γ-rays. These assumptions are in a strong dependence with δ, which is highly unknown. But it seems that $\delta = 4$ is already a limiting case, and larger decrease of $L_{em,\gamma}$ is not expected.

The γ-ray spectrum estimated during the peak flux appeared as a nearly flat one (cyan data

in Fig. 3.4), though the photon index estimation uncertainty is large ($\Gamma = 1.93 \pm 0.19$). This is similar with the spectrum measured in a quiet state (Fig. 3.4, gray data), although with a significantly increased flux. The γ-ray photon index measured before and after the peak flux hints at spectral hardening (see Table 3.1 and Fig. 3.4 blue and red data). However, large uncertainties in the photon index estimations do not allow us to make strong conclusions on the spectral hardening or softening. Although, as compared with the quiet state, it is clear that during the active states the γ-ray flux increases and the spectrum shifts to higher energies.

The broadband SED of NGC 1275 (Fig. 3.4) shows that during the bright γ-ray states, the X-ray flux also has increased. The analysis of the Swift XRT data detected during F2 results in an unabsorbed flux of $F_{0.3-10\,keV} \approx (0.86 - 1.06) \times 10^{-10}\, erg\, cm^{-2}\, s^{-1}$ which nearly 3 times exceeds the averaged flux observed in February 2016. We note that the X-ray photon index measured during the quiet state is somewhat similar to the values measured by XMM-Newton [154], while during the active states the X-ray photon index is steeper (~ 1.7). In the lower energy band, the UV flux from UVOT observations is relatively stable when comparing the quiescent and flaring states, albeit the data from all filters are not available to make definite conclusions.

3.4.1 The Variation of γ-ray Photon Index

The γ-ray photon index changes during ~8.7 years of Fermi-LAT observations are investigated with the help of an adaptively binned light curve. In Fig. 3.3 (upper panels) the photon flux and index variation in time are shown for the time that covers only F1 and F2. In the course of $\sim$ 8.7 years, the hardest photon index of $\Gamma = 1.62 \pm 0.13$ was observed on MJD 55331.51 for $\sim$ 2.78 days, while the softest index of $\Gamma = 2.77 \pm 0.21$ was detected on MJD 56124.71. The lowest and highest fluxes (above 208.6 MeV) were $F_\gamma = (4.27 \pm 1.06) \times 10^{-8}\, photons\, cm^{-2}\, s^{-1}$ and $F_\gamma = (1.18 \pm 0.28) \times 10^{-6}\, photons\, cm^{-2}\, s^{-1}$, respectively. When the source is in active state, the data accumulated for a few hours is already enough to reach 15% flux uncertainty, while in the quiet states, the data should be accumulated for several days. Interestingly, in the first ~ 8.7 years of Fermi-LAT operation,

the highest-energy photon with $E_\gamma = 241.2$ GeV has been detected on MJD 57756.62 (after F2) within a circle of 0.071° around the nucleus of NGC 1275 with the 3.36σ probability to be associated with it. Another events with $E_\gamma = 221.5, 164.9, 125.6, 123.3$ and 109.2 GeV have been observed on MJD 55402.39, 56760.82, 56610.75, 56578.00 and 57694.65, respectively. We note that the PSF of Fermi-LAT at energies > 10 GeV is sufficient to distinguish the photons with high accuracy, so the highest energy photons are most likely coming from NGC 1275. It appeared that the γ-ray spectra for the periods when the highest energy photons were emitted, have mostly harder photon indexes (e.g., $\Gamma = 1.74 \pm 0.14$ when $E_\gamma = 241.2$ GeV photon was detected). Likewise, when photons with $E_\gamma = 221.5, 164.9, 125.6, 123.3$ and 109.2 GeV were detected, the photon indexes were $= 1.81 \pm 0.15$, 1.93 ± 0.15, 1.79 ± 0.13, 1.94 ± 0.14 and 1.86 ± 0.15, respectively. This hardening is probably associated with the emission from reaccelerated or fresh electrons, which produce also the observed highest energy photons.

The spectral changes observed in the photon-index-flux plane give us important information about the dynamics of the source and an insight into the particle acceleration and emission processes. The photon index Γ as a function of the flux during F1 and F2 is shown in the bottom panels of Fig. 3.3. A counter-clockwise loop is observed during F1, while during F2 the spectral index and flux changes follow a clockwise path. Such loops are expected to occur as a consequence of diffusive particle acceleration at strong shocks and cooling of the radiating particles. As discussed in [165], it is expected to have a counter-clockwise loop, if the variability, acceleration and cooling timescales are similar, implying that during the flare, the spectral slope is controlled by the acceleration rather than by the cooling processes. Consequently, the occurrence of a flare propagates from lower to higher energies, so the lower energy photons lead the higher energy ones. Instead, if the spectral slope is controlled by synchrotron cooling or any cooling process that is faster at higher energies, a clockwise loop will be seen. The counter-clockwise loop observed during F1 suggests that, most likely, this flaring event is due to the acceleration of the lower-energy electrons. Note that such 'harder-when-brighter' behavior was already observed during the previous flares of NGC 1275 [48,155]. The clockwise loop observed during F2 indicates that

during this flare the flux started to increase at low energies (HE radiating particles cool down and radiate at lower and lower energies) and then propagate to HE. This shows that HE electrons are playing a key role during F2, which also produce the highest energy photons from NGC 1275 observed around F2.

The interpretation of the mechanism responsible for spectral evolution can be more complicated than it was discussed above. It has been already shown that, depending on the change of the total injected energy, the dominance of synchrotron and Compton components can also vary, so that the trajectory in the photon index-flux plane evolves clockwise or counter clock-wise, depending on the total energy and the observed energy bands [166]. Thus, the observed spectral evolution is quite sensitive to various parameters in the model and it is hard to draw any firm conclusions. The discussions above are of first order approximation and are generally meant to understand the dynamics of the system.

3.4.2 The Estimation of the Flux Variability Period

During F1 and F2, the flare time profiles (Fig. 3.2 upper panels blue data) are investigated by fitting them with double exponential functions [31] and described in section 1.4.1. The fitting parameters are summarized in Table 3.2 and the corresponding fit is shown in Fig. 3.2 middle panels (red dashed line). The time profiles show asymmetric structures in both flares, showing a slow rise and a fast decay trend. The time peak of F1 is MJD 57320.18 with the maximum intensity of $(2.39 \pm 0.31) \times 10^{-6}\, photons\, cm^{-2}\, s^{-1}$. The rise time is 32.49 ± 7.20 hours with a sudden drop within 2.22 ± 1.19 hours. The parameters of F2 are better estimated and are characterized with a shorter rise time, when within 8.03 ± 1.24 hours the flux reaches its maximum of $(4.20 \pm 0.48) \times 10^{-6}\, photons\, cm^{-2}\, s^{-1}$ on MJD 57753.79 and drops nearly 4 times in $\sim$ 6 hours. The minimal e-folding time is $t_d = 1.21 \pm 0.22$ hours, using the decay time scale of F2, and it is the most rapid γ-ray variability observed for NGC 1275. We note that even if the rise time of F2 is used, the flux e-folding time of about 8.03 ± 1.24 hours will still be shorter than any previously reported value. The obtained shortest flux e-folding time, $t_d = 1.21 \pm 0.22$ hours, is unusual for radiogalaxies and has never been observed for any other radiogalaxy so far.

Flare period	$t_r \pm err$ (hour)	$t_d \pm err$ (hour)	t_0 MJD	$F_c(\times 10^{-7})$ $ph\ cm^{-2}s^{-1}$	$F_0(\times 10^{-7})$ $ph\ cm^{-2}s^{-1}$
2015 October	32.49 ± 7.20	2.22 ± 1.19	57320.41 ± 0.19	8.43 ± 1.42	23.92 ± 3.08
2016 Dec/2017Jan	8.03 ± 1.24	1.21 ± 0.22	57753.88 ±0.04	9.73 ± 1.75	41.96± 4.82

Table 3.2: Parameter values best explaining the flares.

It is more similar to the rapid γ-ray variability detected from several bright blazars [39, 40]. [39] was the first to point out that during the γ-ray flares of PKS 1510-089 the flux doubling time-scale was as short as 1.3 ± 0.12 hours which was the shortest variability time-scales measured at MeV/GeV energies at that time. It is interesting that such rapid γ-ray variability is mostly observed from flat-spectrum radio quasars. The asymmetric profile of NGC 1275 flares can be explained if assumed that the accelerated particles (e.g., by shock acceleration) quickly cool down due to the increase of the magnetic field (assuming the electrons dominantly lose energy by synchrotron cooling). In order to interpret the fast decay ($t_d = 1.21 \pm 0.22$ hours) as cooling of relativistic electrons ($t_{decay} = t_{cooling}/\delta$; $t_{cooling} = 6\,\pi\, m^2 e\, c^3/\sigma_T B^2\, E_e$) with $E_e = 100$ GeV, the magnetic field should $be\, B \approx 478\, mG(\delta/4)^{-1/2}(tdec/1.2h)^{-1/2}\,(Ee/100GeV\,)^{-1/2}$ (where we assumed a moderate Doppler boosting factor of δ = 4), which is not far from the typical values usually used in the modeling of emission from radiogalaxies [42]. Even if the magnetic field is 10–100 times lower than this value, the shock acceleration time scales ($t_{acc} \approx 6\, r_g\, c/v_s^2$) would be more than enough to accelerate the electrons > 100 GeV within the observed rise time scale (8.03 ± 1.24 hours).

3.4.3 The Origin of Multiwavelength Emission: Discussion

The observed short time scale variability of 1.21 ± 0.22 hours allows constraining the characteristic size of the emitting region radius to $R_\gamma \leq \delta \times c \times \tau \approx 5.22 \times 10^{14}\,(\delta/4)$ cm. If the entire jet width is responsible for the emission, assuming the jet half-opening angle $\theta_j \simeq 0.1^\circ$, the location of the emitting region along the jet will be $r \simeq R_\gamma\,/\theta_j \simeq 0.1\,(\delta/4)\,(\theta_j/0.1^\circ)^{-1}$ pc. This strongly suggests that the observed emission is most likely produced in the subparsec-scale jet. In principle the jet can be much more extended and

the emission is produced in a region smaller than the width of the jet. For example, multiple regions moving in a wider jet having different beaming factors can be an alternative possibility [53].

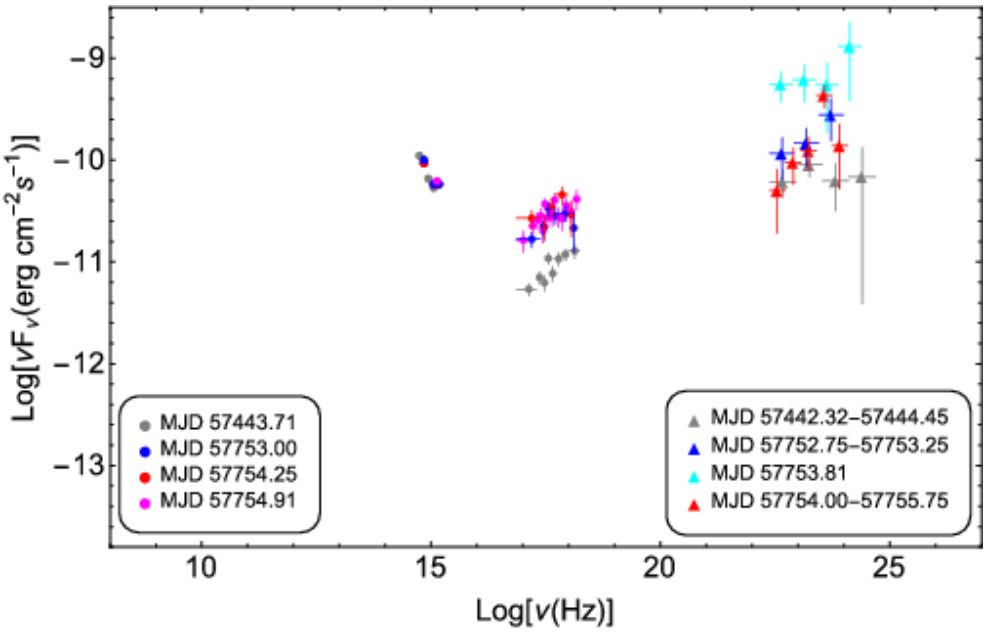

Figure 3.4: The multiwavelength SED for the periods presented in Table 3.1.

In this model, the emission is expected to take place in a broadened jet formation zone close to the central supermassive black hole, where even for a large jet angle, a few emission zones can move directly toward the observer and Doppler boost the emission. Here the emission region is very close to central source, again implying that the innermost jet (sub parsec-scale) is responsible for the emission. The SED presented in Fig. 3.4 as well as that in [157], hint at a double-peaked SED similar to those of other GeV/TeV-emitting radiogalaxies [42] and blazars. This similarity allowed to model the SED of NGC 1275 within the one-zone synchrotron SSC scenario [157]. However, it failed to reproduce the required large separation of the two peaks (gray data in Fig. 3.4) with small Doppler factors ($\delta = 2 - 4$) typical for radiogalaxies. With the new data, the situation even worsened: even if the data are not enough to exactly identify the location of the peaks, clearly, the first peak is at $\sim (10^{14} - 10^{15}) Hz$ (unchanged) while the rising shape of the MeV/GeV spectrum indicates the second peak shifted to higher frequencies. Such large separation of the two SED peaks unavoidably requires a higher Doppler factor than that used previously.

Moreover, if one-zone SSC emission dominates, usually it is expected to have correlated changes in the X-ray/γ-ray band, which are not observed here. One can avoid these difficulties by assuming that HE emission is produced in a local substructure of the jet, which is characterized by a higher boosting factor and/or smaller inclination angle.

For example, the mini-jets generated by local reconnection outflows in a global jet ('jets in a jet' model [168]) can have extra Lorentz boosting and the emission can be produced around these local reconnection regions. This successfully explains the fast TeV variability of M87 [169] so that it can be naturally considered also in this case. In addition, two-zone SSC models, when different regions are responsible for low and high-energy emissions, can be an alternative. In more complex-structured jet models the seed photons for IC scattering can be of external origin (the emission region is the layer and external photons are from the spine, or vice versa [55] the energy of which is higher than that of synchrotron photons resulting in the shift of the emission peak to higher energies. However, these models involve additional parameters, which cannot be constrained with the current data set and additional observations in the radio/optical and VHE γ-ray bands are required.

3.5 Summary

The γ-ray emission from NGC 1275 during $\sim$ 8.7 years of Fermi LAT observations was investigated. The source displayed prominent flaring activities in October 2015 and December 2016/January 2017 with the 3-hour peak flux above 100 MeV of $(3.48 \pm 0.87) \times 10^{-6}\, photon\, cm^{-2}\, s^{-1}$ observed on 2016 December 31 corresponding to an apparent isotropic γ-ray luminosity of $L\gamma \simeq 3.84 \times 10^{45}\, erg\, s^{-1}$. This luminosity is more typical for BL Lac blazars and corresponds to a large fraction of the kinetic energy of the NGC 1275 jet, implying that the γ-ray production efficiency is very high.

During the major flares, the photon statistics allowed us to investigate the flare properties with as short as 3-hour intervals for the first time. This allowed to find very rapid variability with the flux e-folding time as short as 1.21 ± 0.22 hours, which is very unusual for radiogalaxies. The γ-ray photon index of the source was evolving during the flaring periods, showing counter clockwise and clockwise loops in the photon-index-flux plane during the

flares in October 2015 and December 2016/January 2017, respectively. Also, some of the highest energy γ-ray photons observed from the source during ~8.7 years arrived around the same active periods. Perhaps this rapid γ-ray flare was associated with effective particle acceleration that led to emission of these photons.

The observed hour-scale variability suggests that the emission is produced in a very compact emission region with $R_\gamma \leq 5.22 \times 10^{14}\ (\delta/4)\ cm$, and perhaps it is produced in a sub-parsec scale jet. During the γ-ray activity, the HE component not only increased but also shifted to higher energies. Considering this shift and the large γ-ray luminosity, it makes it very challenging to explain the observed X-ray and γ-ray data in the standard synchrotron/SSC models. Additional assumptions on the jet structure/emission processes are to be made.

Chapter 4

4. HE γ-RAY EMISSION FROM PKS 0625-35 RADIOGALAXY

4.1 Introduction

As we mentioned in section 1.1, in the γ-ray band the dominant sources are AGNs of different types. The studies of blazars, which are the dominant type of AGNs detected in the γ-ray band, allowed to investigate the emission processes in the innermost part of the je. The AGNs with the jets pointing away from the observer (radiogalaxies, seyferts, etc.) were not considered as favored GeV sources, because the larger jet inclination angle (compared with the jet of blazars) makes their non-thermal emission less Doppler-boosted. The detection of these sources provided new perspectives to study HE emission processes in different components of AGNs.

It is interesting that the emission from some radiogalaxies the γ-rays not only in HE but also VHE γ-ray band were detected. These are Centaurus A [65], M87 [170], NGC 1275 [171] and PKS 0625-35 [146]. Using multiwavelength data, the emission detected from Centaurus A, M87 and NGC 1275 is well investigated showing that the emission is most likely produced in the innermost jet and interestingly the emission is described by blazar like synchrotron/SSC emission. These observations allowed obtain important information about the physics of their jets. Only recently VHE γ-ray emission above 250 GeV has been detected from PKS 0625-35 [146]. The emission is well described by a power-law with the index of $\Gamma = 2.8 \pm 0.5$, which extends up to 10 TeV. PKS 0625-35 is at a red shift of $z = 0.055$ having radio morphology more similar to that of the Fanaroff-Riley class I radio sources [172]. In the MeV/GeV band, the γ-ray emission from PKS 0625-35 is described with an unusual hard photon index, $\Gamma = 1.87 \pm 0.06,$ as compared with the average photon index of radiogalaxies - $\Gamma > 2.3$. The hard photon index and the detection in the VHE γ-ray band have made this

radiogalaxy an interesting target where the particle acceleration and emission processes can be examined under the most extreme regimes.

Considering the large amount of data available in the γ-ray band (around 9 years), one can study the γ-ray emission properties with improved statistics. Namely, the γ-ray spectra above GeV energies can be investigated with better statistics than before and by considering the data from longer periods, one can look for γ-ray flux variability in long as well as in short time scales, which is necessary for theoretical modeling. This is motivated us to have a new look on the emission from PKS 0625-30 using the most recent data available from Fermi LAT and Swift UVOT/XRT data.

4.2 Fermi-LAT Data Analysis

For the present analysis, the publicly available Fermi-LAT 9-years data, from 4th August 2008 to 4th August 2017 (MET 239557417–518227205) are analyzed with the same steps as presented in section 1.4.1, where the Pass 8 data used. In particular, we downloaded photons from a 10° region centered on VLBI radio position of PKS 0625-35 (RA, Dec) = (96.77, -35.49) and worked with a $14^\circ \times 14^\circ$ square region of interest (ROI). The fitting model includes diffuse emission components and γ-ray sources within ROI (the model file is created based on 3FGL) and the Galactic background component is modeled using the LAT standard gll_iem_v06 diffuse background model and iso_P8R2_SOURCE_V6_v06 for the isotropic γ-ray background. The normalization of background models as well as fluxes and spectral indices of sources within 10° are left as free parameters in the analysis.

Results of the Spectral analysis: We assume that the γ-ray emission from PKS 0625-35 is described by the power-law where the normalization and index are considered as free parameters, then the binned likelihood analysis is performed. From a binned gtlike analysis, the best-fit power-law parameters for PKS 0625-35 are

$$\left(\frac{dN}{dE}\right)_P = (8.99 \pm 0.47) \times 10^{-11} \left(\frac{E}{100}\right)^{-1.88 \pm 0.04} \text{MeV}^{-1}\,\text{s}^{-1}\,\text{cm}^{-2}, \qquad (4.1)$$

Which corresponds to $F_\gamma = (1.02 \pm 0.10) \times 10^{-8}\,\text{photon}\,\text{cm}^{-2}\text{s}^{-1}$ integral flux with $\text{TS} = 1041.1$, that is $\approx 32.3\sigma$ detection significance above 100 MeV.

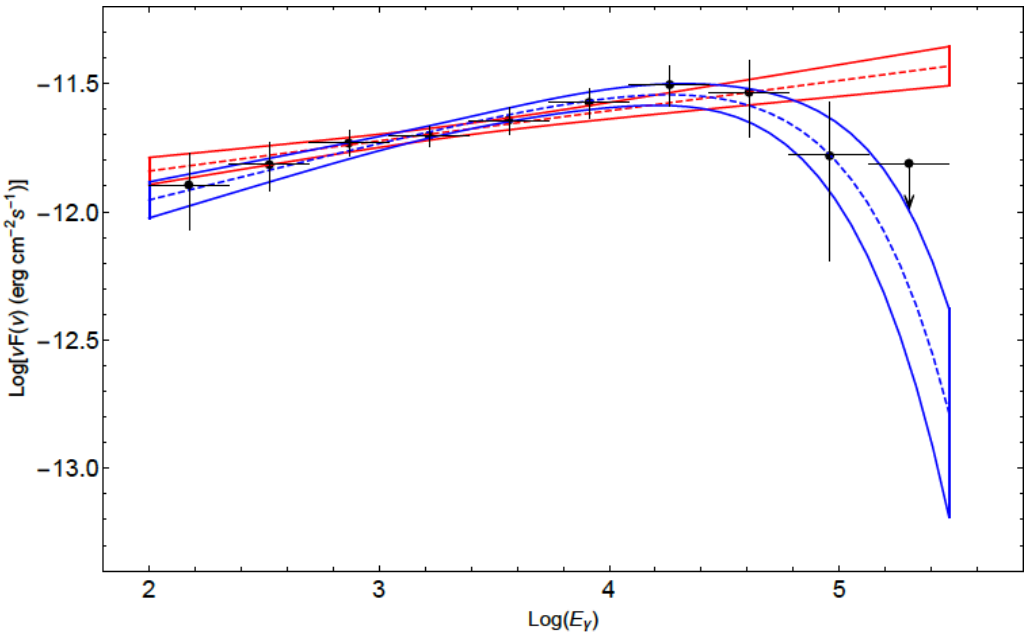

Figure 4.1: Spectral energy distribution of the core of PKS 0625-35 as compared with the best Power-Law (red) and Power-Law with Exponential Cut-off (blue) models.

This spectrum for 10 energy bins is presented in Fig. 4.1 with the red bowtie. There is an indication of deviation of the power-law model with respect to the data around 100 GeV. In order to check for a statistically significant curvature in the spectrum, an alternative fit of the power-law with an exponential cutoff function in the form of $\mathrm{dN/dE} = \mathrm{E}^{-\alpha}\mathrm{Exp}(-\mathrm{E}/\mathrm{E}_{\mathrm{cut}})$ is done, which results in $\alpha = 1.76 \pm 0.16$ and $\mathrm{E}_{\mathrm{cut}} = 80.77 \pm 40.95$ GeV (blue bowtie plot in Fig. 4.1). The power-law and cutoff models are compared with a log likelihood ratio test: the TS is twice the difference in the log likelihoods, which gives 9.9 for this case. Thus, the exponential cutoff model is preferred over the simple power-law only at 3.2σ level, so that the power-law can't be rejected; but the detection of PKS 0625-35 in the TeV band by H.E.S.S [144] gives a photon index of $\Gamma_{\mathrm{TeV}} = 2.8 \pm 0.5$ which strengthens the assumptions of the cut-off in the GeV band.

Temporal analysis: The γ-ray light curve is calculated with the unbinned likelihood analysis method implemented in the gtlike tool. $(0.1 - 300)$ GeV photons are used in the analysis with the appropriate quality cuts applied in the data selection. The photon indices of all background sources are fixed to the best guess values obtained in full time analysis in order to reduce the uncertainties in the flux estimations.

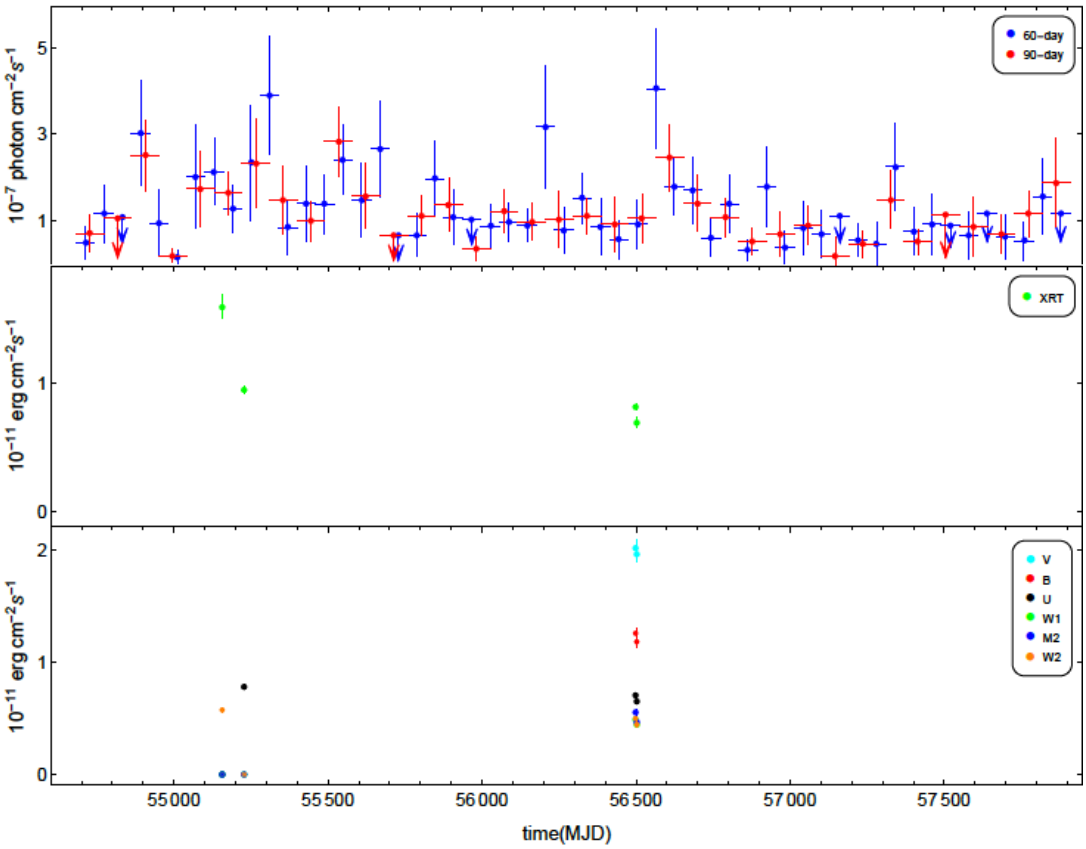

Figure 4.2: The light curves in the γ-ray, X-ray and optical bands. The γ-ray light curve was calculated using 60-day (blue) and 90-day (red) bins.

The power-law index of PKS 0625-35 is first considered as a free parameter and then as a fixed one. Since no variability is expected for the background diffuse emission, the normalization of both background components is also fixed to the values obtained for the whole time period. Fig. 4.2 illustrates the γ-ray flux variation above 100 MeV for 60-day (circle) and 90-day (triangle) sampling. A χ^2 test shows that the reduced χ^2 is $\chi^2/\mathrm{dof} = 0.95$ with the probability of constant flux $\mathrm{P}(\chi^2) = 0.56$ for 60-day bins and $\chi^2/\mathrm{dof} = 1.45$ with $\mathrm{P}(\chi^2) = 0.049$ for the 90-day bins. These numbers are consistent with no variability although the light curve with 90-day bins indicates possible variability. Because of limited statistics, no definite conclusion can be drawn.

4.3 Optical/UV and X-Ray Data Analysis

Swift XRT: All XRT observations were in PC mode (ObsID: 39136001, 39136002, 49667001 and 49667002 and the observations were made on MJD 55157.8, MJD 56502.8,

MJD 56499.8 and MJD 55228.2, respectively. The data are analyzed following the steps presented in the section 1.4.1. Namely, the data were analyzed using the XRTDAS software package (v.3.3.0) distributed by HEASARC as part of the HEASoft package (v.6.21). The source spectrum region was defined as a circle with a radius of $47"$ at the center of the source, while the background region was defined as an annulus centered at the source with its inner and outer radii being $120"$ and $200"$ respectively. Since the source count rate was always below $0.5\,\mathrm{counts\,s^{-1}}$ no pile-up correction was necessary. The spectrum was rebinned to have at least 20 counts per bin, ignoring the channels with energy below 0.3 keV, and fitted using XSPEC v12.9.1a. The 0.3-10.0 keV spectrum is well fitted by an absorbed power-law model with column density $\mathrm{N_H} = 6.36 \times 10^{20}\mathrm{cm^{-2}}$. The results of the fit are given in Table 4.1 and the corresponding spectra are shown in Fig. 4.3.

Obs. ID	Date	Exp. Time (s)	Photon Index[a]	Unab. Flux[b]	$\mathrm{x^2_{red}(d.o.f.)}$
39136001	Nov 22,2009	1379	1.97 ± 0.08	15.86± 0.90	1.20 (20)
39136002	Feb 01,2010	4523	2.26 ± 0.05	9.42 ± 0.31	1.31 (43)
49667001	Jul 26, 2013	8079	2.11 ± 0.09	8.09 ± 0.23	1.35 (59)
49667002	Jul 29, 2013	2452	2.12 ± 0.04	6.90 ± 0.41	1.05 (15)

Table 4.1: Fitting results of the data obtained by the XRT instrument on board Swift.

Notes:

[a]Photon index from X-ray data analysis.

[b]X-ray flux in the energy range 0.3–10 keV in units of $\times 10^{-12}\ erg\ cm^{-2}\ s^{-1}$ (corrected for the Galactic absorption).

The change of the X-ray flux during these observations can be seen on the light curve shown in Fig. 4.2 (middle panel). Although the X-ray flux did not increase significantly (the highest flux of $\mathrm{F_{0.3-10\,keV}} = (15.86 \pm 0.90) \times 10^{-12}\ \mathrm{erg\,cm^{-2}\,s^{-1}}$ observed on November 22, 2009, exceeds the lowest by 2.3 times), the X-ray photon index softened, changing in the range of $\Gamma_x = (1.97 - 2.26)$ during the whole γ-ray observational period.

Swift UVOT: In the analysis of the Swift UVOT data, the source counts were extracted from an aperture of $5.0"$ radius around the source. The background counts were taken from the neighboring circular region having a radius of $15"$. The magnitudes were computed using

the uvotsource tool (HEASOFT v6.21) and then the furthers steps (correction for Galactic absorption, effective wavelength calculations, etc.) are presented in section 1.4.1. For the first two observations on MJD 55157.8 and MJD 56502.8 W2 U filters were unavailable, while all filters for the last two observations are available.

4.4 The Theoretical modeling of the Broadband SED

Modeling Data. The broadband SEDs of PKS 0625-35 are shown in Fig. 4.3 where the radio data (gray) are archival and taken from ASI Science Data Center. The SEDs hint at the existence of two non-thermal emission peaks in the IR/optical/UV and HE γ-ray bands. Taking into account the results of the previous studies of other Fermi LAT-observed radiogalaxies [148, 46, 72], the multiwavelength emission of PKS 0625-35 is modeled using the synchrotron/Synchrotron Self-Compton (SSC) [173, 174] model. The radio through optical emission is due to the synchrotron emission of energetic electrons in the homogeneous, randomly oriented magnetic field, while the X-ray to HE γ-ray emission is due to the inverse Compton scattering of the same synchrotron photons.

The emission region (the "blob") is assumed to be a sphere with a radius of R which carries a magnetic field with an intensity of B and a population of relativistic electrons, which have a power-law with an exponential cut-off energy distribution expected from shock acceleration theories [175], $N_e'(E_e') = N_0' \, (E_e'/m_e c^2)^{-\alpha} \, Exp[-E_e'/E_{cut}']$ and the electron energy density (U_e) scales with that of the magnetic fields (U_B). Since the blob moves along the jet, the radiation will be amplified by a relativistic Doppler factor of δ for which a typical value of (for the radiogalaxies) $\delta = 4$ was used. It is hard to estimate the emission region size in the absence of statistically significant γ-ray variability. Most likely, the innermost jet is responsible for the γ-ray emission, and we assume that the blob size is $R \approx 4 \times 10^{17} cm \sim 0.1 \, pc$.

The construction of the parameters is performed by Markov chain Monte Carlo (MCMC) method using the modified *naima* package [176], where the spectral parameters and the uncertainty of the model for each parameter is estimated by MCMC sampling of their likelihood distributions. The sampling is run by 64 simultaneous walkers, with 100 steps and

100 burin-in of run. During the sampling, we use the following ranges of the parameters: $1.5 \leq \alpha \leq 10$, $0.511\,MeV \leq E'_{(cut,min,max)} \leq 1\,TeV$, N_0 and B are constrained to be positive values. In the case of synchrotron/SSC model, the applied emissivity function of Synchrotron radiation is taken from [177], where random magnetic field is considered. And the IC radiation is calculated using the monochromatic differential cross-section presented in [178].

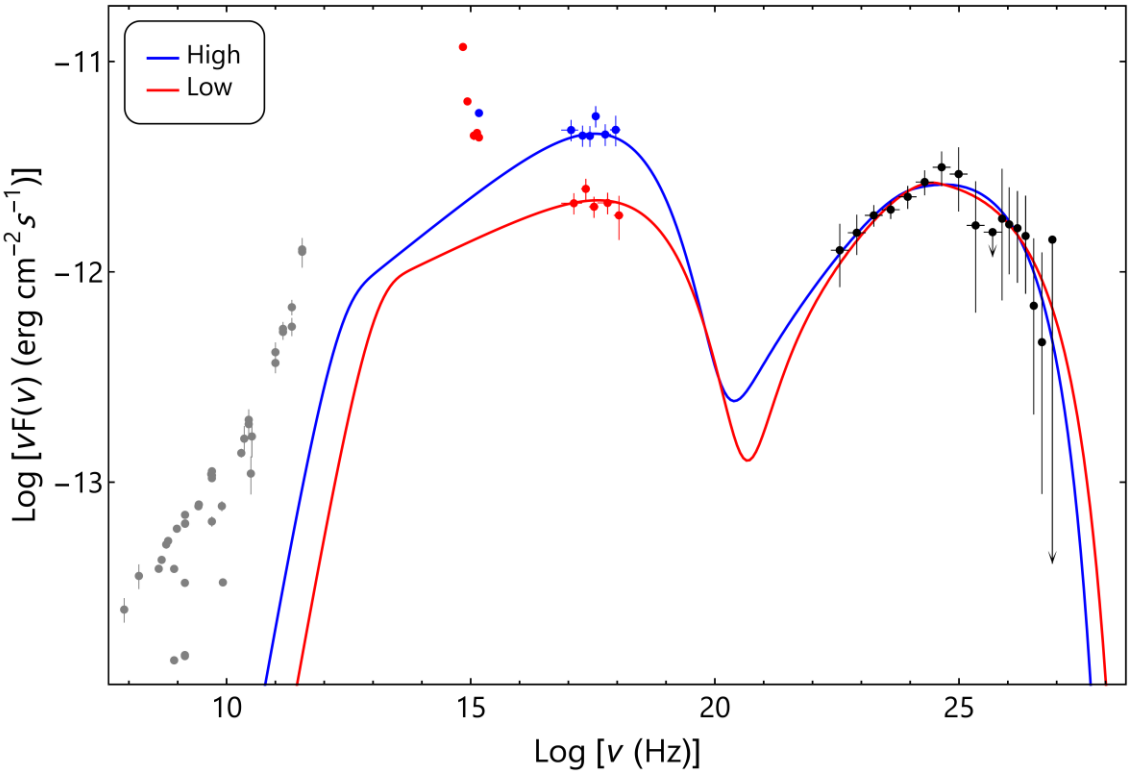

Figure 4.3: The broadband SED of PKS 0625-35 emission for low and active states. The blue and red solid lines are the synchrotron/SSC model fitting for two different X-ray fluxes. The model parameters are presented in Table 4.2.

The results of the modeling: The broadband emission modeling results obtained in two different X-ray states are shown in Fig. 4.3 with the corresponding parameters in Table 4.2. We choose to model the SEDs for two different photon indices in the X-ray band, $\Gamma_X = 1.97 \pm 0.08$ (blue circle) and $\Gamma_X = 2.12 \pm 0.04$ (red circle). Also, these periods correspond to the highest and lowest X-ray fluxes observed during the considered period. In the fit we did not include the radio data since the radio emission can be produced from the low-energy electrons which are accumulated for longer periods, but require that the

radio flux should not exceed the observed flux. Thus higher values of E'_{min} are obtained, $E'_{min} = 3.40 \pm 2.18\, GeV$ (summed the errors in quadrature) and $E'_{min} = 1.23 \pm 1.13\, GeV$ for the low and active states, respectively. The HE tail of the underlying electron distribution, E'_{max}, is mostly defined by the HESS data, this is why in the modeling of SEDs in the active and low states its values are similar, $E'_{max} = 44.84 \pm 34.42\, TeV$ and $E'_{max} = 46.38 \pm 33.88\, TeV$, respectively. The -ray photon index observed in the MeV/GeV band by Fermi LAT allows to estimate the power-law index of underlying electrons responsible for the emission. The slope of IC emission, $(\nu F\nu \propto \nu^{1-s})$ is related with the power-law index of electron by $s = (\alpha - 1)/2$ where $s = 1 + \Gamma = -0.88$. The estimated values are $\alpha = 2.76 \pm 0.12$and $\alpha = 2.63 \pm 0.15$ for the low and active states respectively, in agreement with the predictions.

	Parameter	Steady	Active
Doppler factor	δ	4	4
Norm. of electron distribution	$N'_0 \times 10^{52} eV^{-1}$	$12.02^{+0.25}_{-0.28}$	$1.261^{+0.03}_{-0.03}$
Electron spectral index	α	2.76 ± 0.12	2.63 ± 0.15
Minimum electron energy	$E'_{min}(GeV)$	$3.40^{+22.65}_{-20.93}$	$1.26^{+14.02}_{-0.76}$
Cutoff electron energy	$E'_{cut}(TeV)$	$4.20^{+2.38}_{-1.74}$	$19.71^{+1.22}_{-0.63}$
Maximum electron energy	$E'_{max}(GeV)$	$44.84^{+35.78}_{-33.01}$	$46.38^{+35.81}_{-31.84}$
Magnetic field	$B[mG]$	$8.95^{+2.64}_{-2.22}$	$16.27^{+4.40}_{-3.45}$
Jet power in magnetic field	$L_B \times 10^{41} erg\ s^{-1}$	7.69	25.41
Jet power in electrons	$L_e \times 10^{43} erg\ s^{-1}$	7.48	5.58

Table 4.2. Model parameters.

Since the synchrotron component has increased, the magnetic field in the active state $B = (16.27 \pm 3.95)\, mG$ is higher than in the low state $B = (8.95 \pm 2.43)\, mG$, since the synchrotron emission depends on the total number of emitting electrons N_e, Doppler factor δ and magnetic field strength B. The magnetic field energy density is $U_B = 0.32 \times 10^{-5}\ erg\ cm^{-3}$ and $U_B = 1.05 \times 10^{-5}\ erg\ cm^{-3}$ for low and high states, respectively, lower than the same values for electrons, $U_e = 3.10 \times 10^{-4}\ erg\ cm^{-3}$ and $U_e = 2.31 \times 10^{-4}\ erg\ cm^{-3}$, respectively.

The jet power in the form of magnetic field and electron kinetic energy are calculated by $L_B = \pi c R_b^2 \Gamma^2 U_B$ and $L_e = \pi c R_b^2 \Gamma^2 U_e$, respectively, and are given in Table 4.2. The jet power in electrons changes within $(5.58 - 7.48) \times 10^{43}\ erg\ s^{-1}$ and that in the magnetic field changes within $(7.69 - 25.41) \times 10^{41}\ erg\ s^{-1}$, which are lower than the Eddington luminosity $L_{EDD} = 1.63 \times 10^{47}\ erg\ s^{-1}$ for the black hole with $1.29 \times 10^9 M_\odot$ [179].

4.5 Summary

In this chapter, the multiwavelength emission from PKS 0625-30 is investigated using the Swift XRT/UVOT and Fermi LAT data. The modeling of SEDs in different periods allowed to investigate the jet properties and physical processes that take place in the core where, most likely, the jet is formed.

The γ-ray data analysis shows that the source emission extends above 100 GeV with a hard photon index of $\Gamma = 1.88 \pm 0.04$ and a detection significance of $\approx 32.3\sigma$. There is a hint of a spectral curvature in the γ-ray spectrum of PKS 0625-30, but the power-law with an exponential cut-off model is preferred over the simple power-law modeling assuming a break around $E_{cut} = 80.77 \pm 40.95\ GeV$ with a significance of only 3.2σ. Although the low statistics does not allow to claim for a statistically significant curvature in the spectrum, the γ-ray photon index observed in the VHE γ-ray band, $\Gamma_{TeV} = 2.8 \pm 0.5$ strongly supports the presence of a break or a cutoff in the GeV spectrum of PKS 0625-30. There is a marginal evidence of variability in the light curve with 90-day binning, although because of low statistics no definite conclusion can be drawn.

In the X-ray band, the average flux in the $0.3 - 10.0$ keV range is around $(0.7 - 1.6) \times 10^{-11}\ erg\ cm^{-2}\ s^{-1}$ with the X-ray photon index of $\Gamma = 2.0 - 2.3$. When the lowest and highest fluxes from Table 4.1 are compared, a nearly 2.3 times increase of the X-ray flux is found, which can be related with the changes of magnetic field in the emitting region. The hardest X-ray photon index is $\Gamma = 1.97 \pm 0.08$ and the softest is $\Gamma = 2.26 \pm 0.05$. These changes in the X-ray flux level and the photon index softening might indicate that different mechanisms are contributing to the acceleration and/or cooling of electrons, which modify the power-law index and the minimum energy of underlying electrons.

The one-zone synchrotron/SSC model can reproduce the observed multiwavelength SED, assuming the γ-rays are produced in a compact region ($\sim 4.17 \times 10^{17}\ cm$) in the innermost jet. Assuming the electrons are accelerated up to $E_{max} = 50\ TeV$ with a power-law index of $\alpha = 2.63 - 2.76$, the observed spectrum above TeV energies can be explained by IC scattering of synchrotron photons on the electron population producing the radio-to-X-ray emission in the jet. The necessary jet kinetic power is $(5.83 - 7.56) \times 10^{43}\ erg\ s^{-1}$, which corresponds to $(0.018 - 0.023)$ % of Eddington power.

Chapter 5

5. X-RAY AND γ-RAY EMISSIONS FROM NLSy1s GALAXIES

5.1 INTRODUCTION

Recently, Fermi-LAT has detected γ-ray emission from five NLSy1s (for more detailed about NLSY1s see section 1.1.3, where the γ-ray emission properties of PKS 1502+036 and PKS 2004-447 were discussed: these sources have flux variability in relatively long time scales and soft photon index in the γ-ray band with 2.61 ± 0.05 and 2.47 ± 0.09 values, respectively. Instead the emission from 1H 0323+342, PMN J0948+0022 and SBS 0846+513 are variable in short time scales and are more powerful sources with large detection significance, which allows to identify and examine flaring period, find minimum variability periods, etc. In this chapter the broad band emission from these three bright NLSy1 is investigated using the ~ 8.8 years Fermi LAT accumulated data and Swift UVOT/XRT observations during the considered period. The basic characteristics of these sources are:

1H 0323+342: The γ-ray emission from this source was initialy reported in [18] using data accunmulated in 9 months. Among the considered sources, it has the closest distance at z=0.0629 [179]. The radio observations showed a flatness in radio spectrum [181] and pc-scale core-jet structure is resolved by VLBI [182]. More recent observations with VLBI at 15 GHz detected sumperluminal component with $\sim(1-7)c$ speed, which allowed to restrict the jet viweing angle to $\leq (4^\circ - 13^\circ)$ [183]. We note that this source has the brightest optical emission compared to other γ-NLSy1s. The black hole mass estimated by different method varies in the range of $(1-3)\times 10^8 M_\odot$ with approximately equal accretion and Eddington rates. The emission from this source is variable almost in all observed bands, from radio to γ-ray bands.

PMN J0948+0022: This galaxy at $z = 0.5846$ is the first γ-ray emitting NLSy1 detected by Fermi-LAT [148] and since now it is considered the most powerful γ-ray emitter among the NLSYs. The radio loudness of this source is $R \approx 846$ [184]. The radio observations showed a hint of core-jet structure [185] with inverted radio spectrum, which also suport the presence of the relativistic jet [186]. PMN J0948+0022 is variable in almost all wavebands, although it is more evident in γ-ray band [187]. The broad band emission was explained using one zone leptonic models, where for the HE γ-ray component IC scattering of synchrotron and BLR photons are used.

SBS 0846+513: This is another NLSy1 powerful in the γ-ray band at z=0.585. The VLBI images showed two components having core-jet structure [139], followed by the detection of superluminal motions [19] and radio to γ-ray variability. In the γ-ray band two significant flaring periods, in 2012 (May-Aug) and in 2013 (Apr-Jun), where observed. The last flare activity in γ-ray band was accompanied by activities in optical/UV and X-ray bands. The broad band emission of SBS 0846+513 was modelled with one-zone synchrotron plus IC from the external BLR [188] or dust torus [189] photons.

5.2 Fermi-LAT Data Analysis

Data acquisition. For the current study, we have used the publicly available data accumulated during the last ~ 8.8 years of Fermi-LAT operation (from August 4, 2008 to June 4, 2017). The data were analyzed with the standard described in section 1.4.1, where $14.1° \times 14.1°$ square ROI centered at the locations of PMN J0948+0022- (RA, dec)= (147.223, 0.363) and SBS 0846+513- (RA, dec)= (132.482, 51.145), and $12.7° \times 12.7°$ at 1H 0323+342- (RA, dec)= (51.313, 34.171) were applied.

Temporal analysis. To identify flaring periods, we generated the light curves with the help of adaptive binning method (see chapter 1, section 1.4.1). The optimal energies providing 20% flux uncertainity were $\mathrm{E_0} = 156.4, 170.8$ and 282.3 MeV for 1H 0323+342, PMN J0948+0022 and SBS 0846+513, respectively and the corresponding light curves for the period from 2008 to 2017 are presented in Fig. 5.1, Fig. 5.2 and Fig. 5.3 with the same sequence.

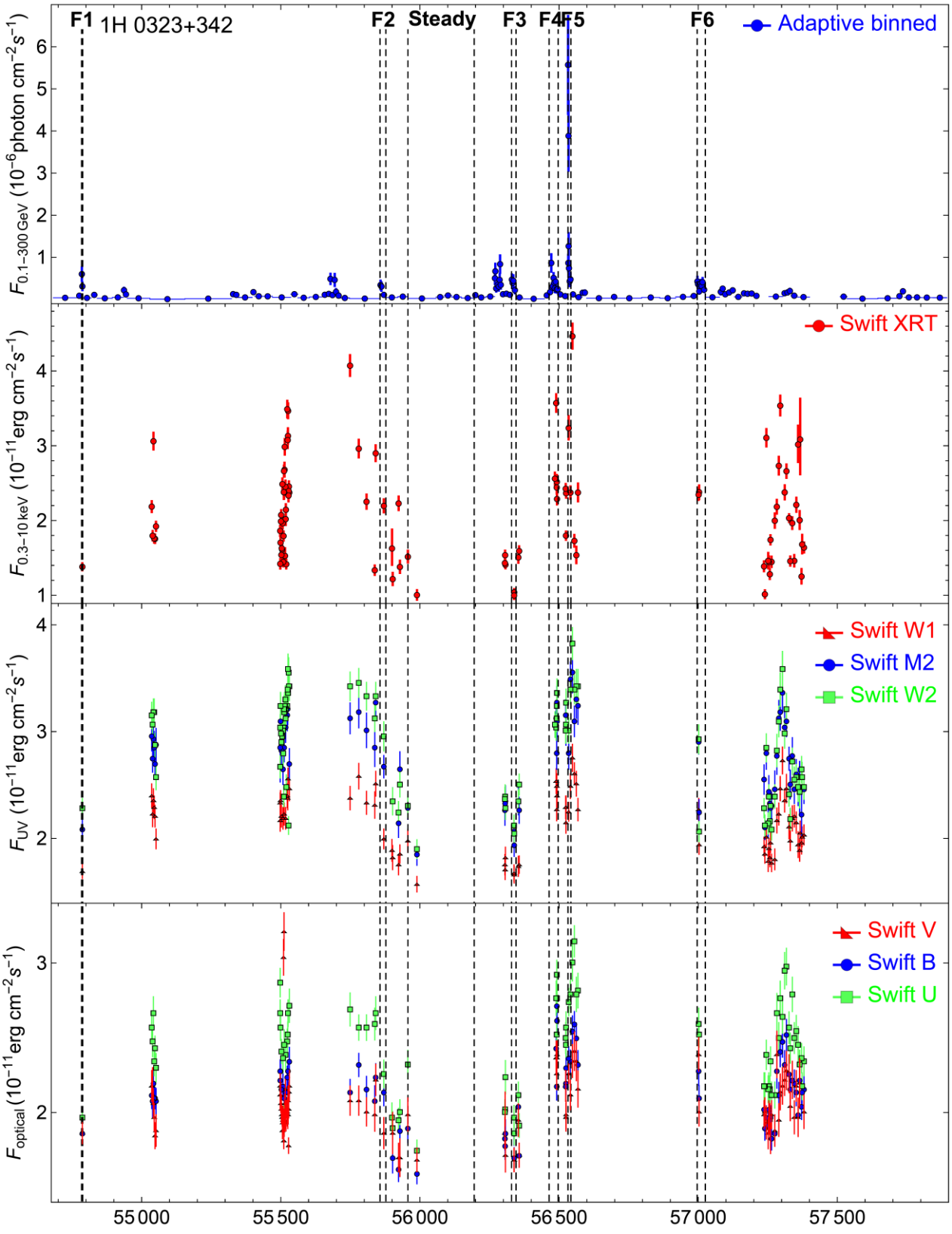

Figure 5.1: The γ-ray, X-ray and optical/UV light curves of 1H 0323+342 between 2008-2017, where the dashed lines denote the flaring and steady states.

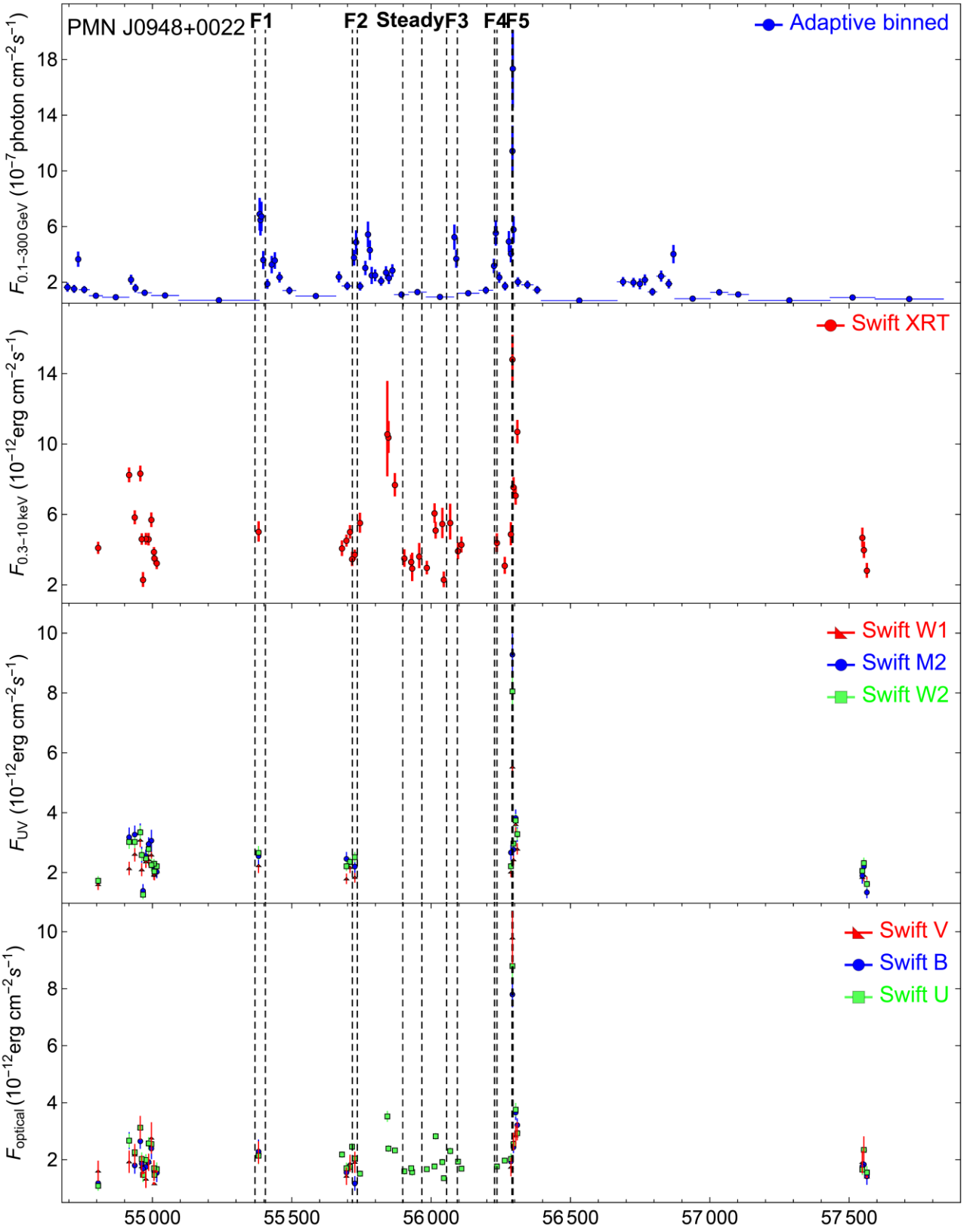

Figure 5.3: The γ-ray, X-ray and optical/UV light curves of PMN J0948+0022 between 2008-2017, where the dashed lines denote the flaring and steady states.

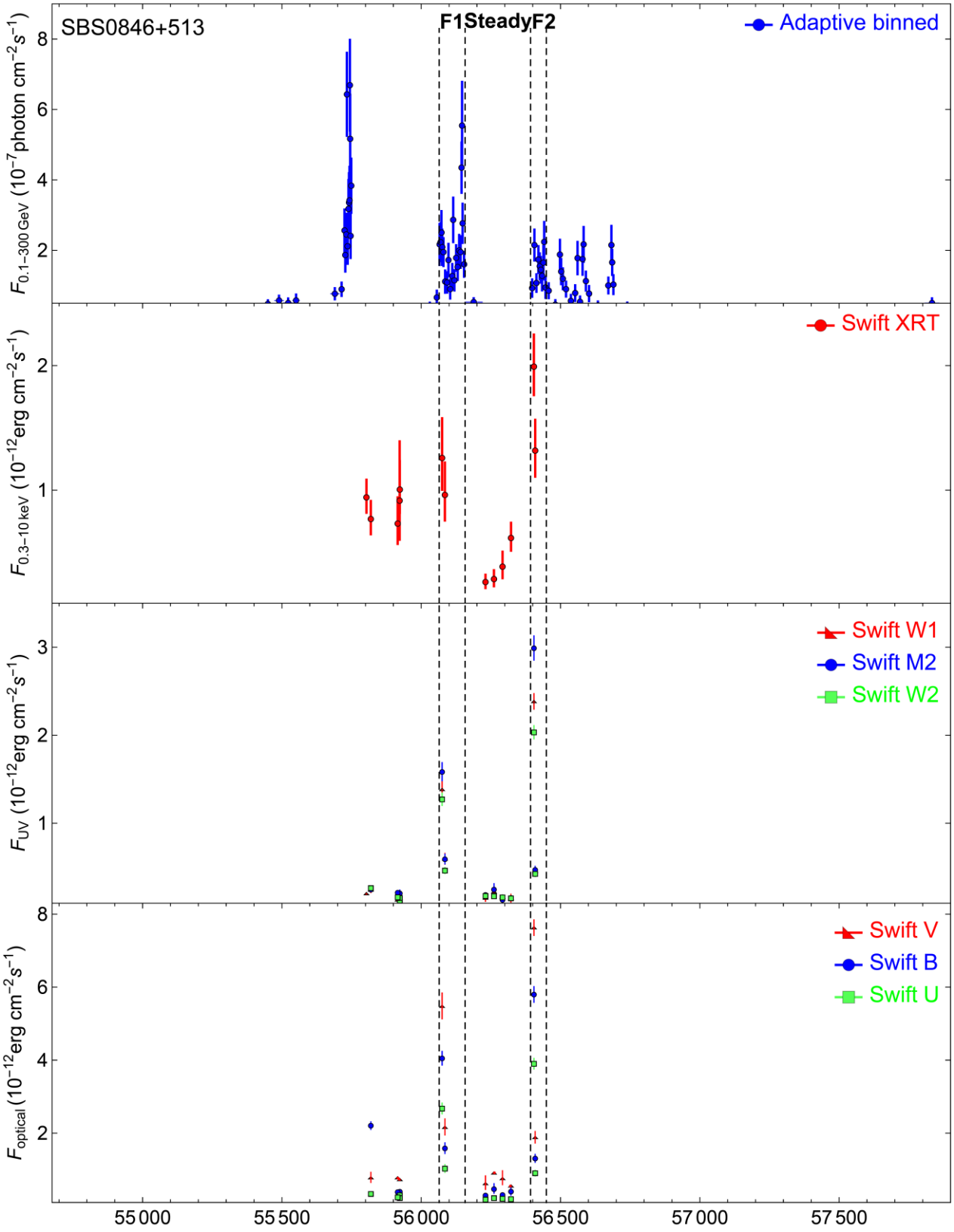

Figure 5.2: The γ-ray, X-ray and optical/UV light curves of SBS 0846+513 between 2008-2017, where the dashed lines denote the flaring and steady states.

In the γ-ray band, 1H 0323+342 is in its quiescent state for most of the time (the flux did not much exceed the averaged value), but the flux increased significantly several times. The most violent increase was observed on MJD 56534.3 when the flux increased up to $(1.98 \pm 0.31) \times 10^{-6}\, photon\, cm^{-2}\, s^{-1}$ within 16.2 hrs and the photon index hardened to 2.22±0.15. After this rapid flare, the source again entered its quiescent state. A sequence of flares can be identified in the light curve of SBS 0846+513, however with a lower amplitude as compared with the flares of 1H 0323+342: the highest flux was observed on MJD 56145.6 - $(6.35 \pm 1.12) \times 10^{-7}\, photon\, cm^{-2}\, s^{-1}$. The high state of SBS 0846+513 continued till MJD 56146.8, when within 19.6 hours the flux was $(4.15 \pm 1.04) \times 10^{-7}\, photon\, cm^{-2}\, s^{-1}$, but the photon index was significantly hard 1.73 ± 0.14, which is the hardest γ-ray photon index detected during the considered period. The light curve of PMN J0948+0022 shows that the source is alternatingly in its flaring or quiescent state. The source flux was above $10^{-6}\, photon\, cm^{-2}\, s^{-1}$ several times (during brightening) which is impressive, considering the large distance of z=0.585. The source was in an extremely active state during MJD 56290.96 - MJD 56294.60, reaching a peak flux of $(1.51 \pm 0.31) \times 10^{-6}\, photon\, cm^{-2}\, s^{-1}$ within 18.9 hrs, which corresponds to an apparent isotropic γ-ray luminosity of $L_\gamma \approx 1.09 \times 10^{48}\, erg\, s^{-1}$, which is typical for the brightest FSRQs. The observed hardest photon index is 2.13 ± 0.18, but for most of the time it is > 2.5. The rapid changes observed in intra-day scales and the amplitude of the increase once more show that in the γ-ray band NLSy1 sources have properties similar to those of blazars.

5.3 Swift UVOT/XRT Data Analysis

5.3.1 XRT Data

The observations of these sources with Swift have been performed many times during the considered ~ 8.8 years. All XRT data were analyzed with the XRTDAS software package (v.3.3.0) distributed by HEASARC along with the HEASoft package (v.6.21). The data were taken only in photon counting (PC) mode for all sources, and since the count rates of all sources were always below $0.5\, counts\, s^{-1}$, no pile-up corrections were necessary. Source

events were extracted in the 0.3-10 keV range within a circle of a radius of 20 pixels (47"), while the background events were extracted from annular regions around the targets. Due to low count statistics for PMN J0948+0022 and SBS 0846+513, to perform spectral analysis, we rebinned the spectrum to ensure a minimum of 1 count per bin and used Cash statistics. All spectra of 1H 0323+342 were rebinned with a minimum of 20 counts per energy bin to allow $\chi 2$ fitting. Whenever multiple datasets were available during the quiescent and flaring states, the event files were merged together. The spectra in the 0.3-10 keV energy range were then analyzed with the Xspec v12.9.1a package, using the power-law model with the Galactic absorption values from [32] taken as frozen parameters. The detailed description of XRT data analysis including data reduction, pile-up correction, spectral analysis and unabsorbed flux calculation are presented in section 1.4.2. The results for all sources are listed Table 5.1.

5.3.2 UVOT Data

In this case the counts were extracted from 5" aperture centered on the source position. The background events of SBS 0846+513 were extracted from circle in free source region with 15" radius, while in the case of 1H 0323+342 and PMN J0948+0022 the annular regions were used with 27" and 24" inner radii, respectively and the widths in both cases were 8". The detailed description of magnitude calculation and correction is presented in section 1.4.3.

5.4 Size of the γ-Ray Emission Region

Initially for all the considered sources, performing a temporal analyses the emission region sizes are estimated. In the light curves presented in Fig. 5.1, 5.2 and 5.3, several bright periods for each source can be identified. In order to derive the flare rise and decay time scales, the light curves for the periods of these flares have been calculated with normal time binning. The shortest bin sizes have been chosen to ensure that i) the flare rise and decay periods are well constrained and ii) the detection significance for each bin exceeds the $\sim 5\sigma$ limit. For some flares, when a large increase of intensity is observed, the flare rise or decay

periods cannot be constrained even when the bins with day or sub-day scales are used. So we select only the intervals when the rise and decay periods of the flares are clearly visible.

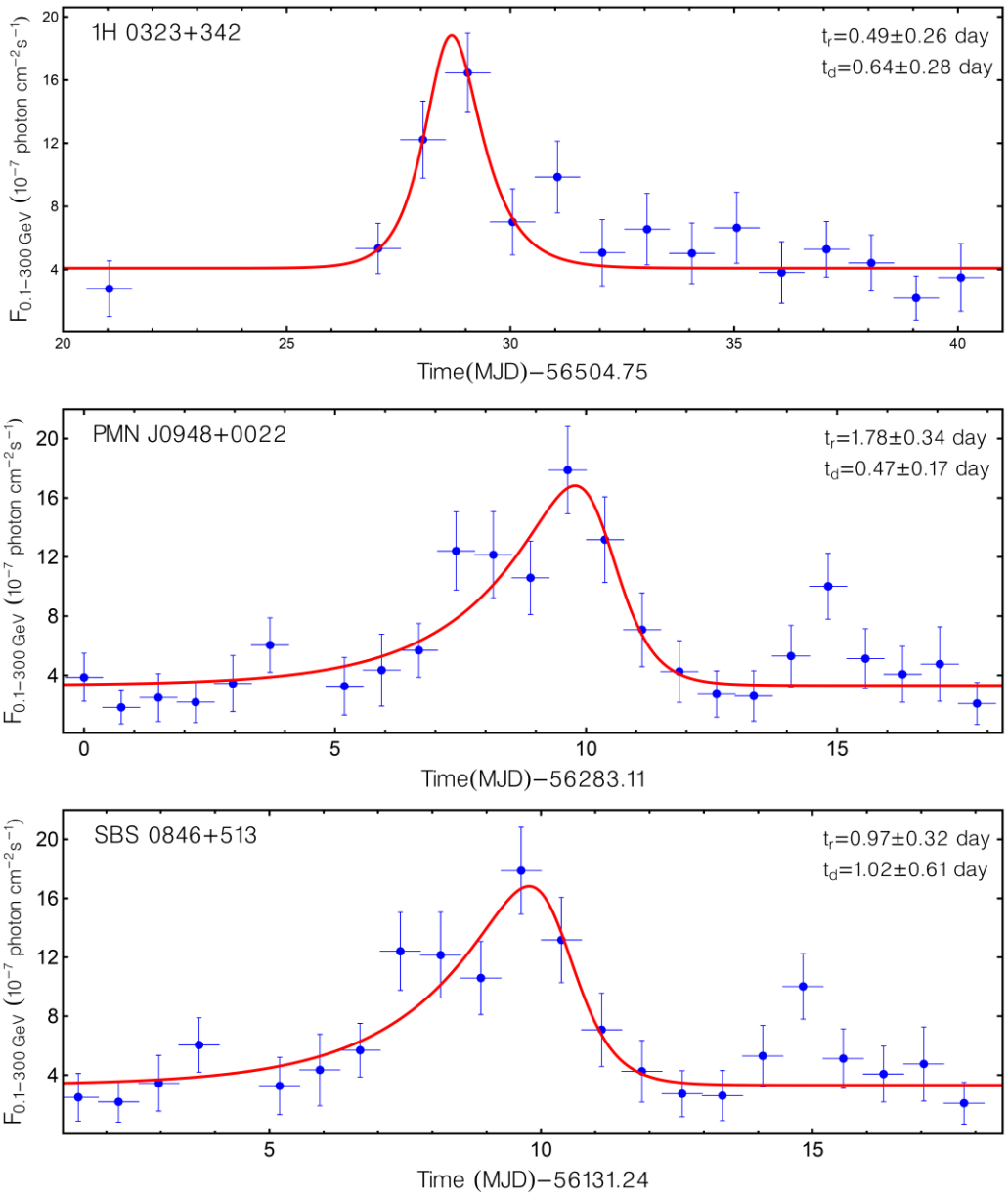

Figure 5.4: The theoretical fitting of 1H0323+342 (F5, Figure 5.1), PMN J0948+0022 (F5, Figure 5.2) and SBS 0846+513 (F2, Figure 5.3) flaring periods with exponential function shown with red lines (the detailed description of this procedure is presented in section 1.4.1).

The period chosen for 1H0323+342 is from MJD 56504.3 to MJD 56596.4, that for SBS 0846+513 is from MJD 56130.7 to MJD 56156.8, both with a day bin, and that for PMN J0948+0022 is from MJD 56282.7 to MJD 56308.7 with an 18-hour bin. The corresponding light curves are shown in Fig. 5.4. To derive the flare doubling timescales and understand

the nature of the flares, the light curves are fitted with an exponential function (see Section 1.4.1 for more detail) and the corresponding fits are shown in Fig. 5.4 (blue line) with the fitting parameters given in each plot. In the case of 1H0323+342 the flux increases several times within $t_r = 0.49 \pm 0.26$ day and then slowly decreases within $t_d = 0.64 \pm 0.28$ day (Fig. 5.4 [upper panel]). The rise time scale of PMN J0948+0022 (Fig. 5.4 [middle panel]), $t_r = 1.78 \pm 0.34$ day is comparably longer than $t_d = 0.47 \pm 0.17$ day, showing a slow rise and a fast decay trend. The time profiles show a nearly symmetric structure in the flare of SBS 0846+513 (Fig. 5.4 [lower panel]) with $t_r = 0.97 \pm 0.32$ day and $t_d = 1.02 \pm 0.61$.

5.5 Quiescent and Flaring States of the Sources

From the γ-ray ligh curves of 1H0323+342, PMN J0948+0022 and SBS 0846+513 flaring and quesecent periods for further spectral analyses were selected. From the many flares tnly the ones, which have simultaneous Swift observations were considered. These periods in all light curves are marked with dashed lines and named with F_i (see Fig. 5.1, 5.2 and 5.3), where F5, F5 and F2 flares of 1H0323+342, PMN J0948+0022 and SBS 0846+513, respectively were considered during the theoretical fitting (in the next section). In the case of steady states, we chose only one period for each source, when the source in all energy bands was in its relatively quiet state. The γ-ray data analysis were performed with unbinned likelihood method and the spectra of each source modeled using simple PL. The fitted model was used to generate the SED with the same steps as described in section 4.4. The results of the spectral analysis are presented in Table 5.1. In the case of XRT analysis, we combined all the observations for the given period. Using *xselect* package, *we* merge the event files, while the combination of exposure maps was performed with *ximage* package. Due to the merging of the counts rate, for some periods the rate was higher than $0.5\ \mathrm{counts\ s^{-1}}$ and the pile-up analysis (see section 1.4.2 for more detail) was performed excluding the events from the $3-4$ pixel circle in the inner part of the PSF. The grouping and spectral analysis for these periods were performed with the same way as for the single observation described in section 5.3.1. The fitting results are provided in the Table 5.1. Different UVOT IDs were combained with the following steps. First we summed the image

extentions of the same exposure into one image with *uvotimsum*, then we copied them into another file using *fappend* task of the FUITILS[7] sub-package. And finally, we summed all copied images again using *uvotimsum* command. The selected source and background regions were the same as for the single observations described in section 1.4.1. The extinction corrected magnitude calculation and conversation into fluxes was performed as explained in section 1.4.2 and the results are presented in Table 5.1.

1H0323+342

Fermi-LAT

State	Period[1]	Flux[2]	Photon index[3]	Test Statistic[4]
Flare 1	54784.4-54788.0	3.82 ± 0.80	2.61 ± 0.19	65.9
Flare 2	55856.7-55877.5	1.57 ± 0.30	2.74 ± 0.17	56.8
Steady	55957.0-56194.9	0.45 ± 0.02	3.07 ± 0.06	47.3
Flare 3	56329.2-56345.4	3.36 ± 0.48	2.79 ± 0.15	108.9
Flare 4	56464.0-56497.1	3.03 ± 0.24	$2.55 \pm 0.0.07$	365.1
Flare 5	56532.3-56542.5	7.82 ± 0.70	2.67 ± 0.10	343.9
Flare 6	56996.3-57025.8	3.17 ± 0.27	2.88 ± 0.10	270.9

Swift-XRT

State	Exposure[5]	Flux[6]	Photon Index[7]	X^2_{red} (d.o.f.)[8]
Flare 1	5944	1.38 ± 0.05	1.89 ± 0.05	1.27(49)
Flare 2	2040	2.19 ± 0.09	1.90 ± 0.06	0.63(35)
Steady	1536	1.00 ± 0.06	1.91 ± 0.10	0.91(13)
Flare 3	4001	1.00 ± 0.05	1.64 ± 0.06	0.92(30)
Flare 4	16890	2.93 ± 0.05	1.82 ± 0.02	0.99(182)
Flare 5	4460	2.83 ± 0.09	1.72 ± 0.04	1.14(62)
Flare 6	5804	2.29 ± 0.05	2.02 ± 0.04	0.97(93)

Swift-UVOT

State	V[9]	B[9]	U[9]	W1[9]	M2[9]	W2[9]
Flare 1	1.86±0.07	1.86±0.02	1.97±0.07	1.69±0.07	2.08±0.10	2.28±0.0
Flare 2	1.86±0.10	2.13±0.09	2.26±0.0	2.00±0.0	2.67±0.10	2.96±0.14

[7] This is one of the FTOOLS sub-packages designed for the manipulation of fits files.

Steady	1.68±0.07	1.59±0.07	1.74±0.07	1.57±0.07	1.85±0.10	1.90±0.0
Flare 3	1.68±0.07	1.86±0.08	1.97±0.08	1.68±0.0	2.06±0.11	2.12±0.10
Flare 4	2.25±0.0	2.37±0.04	2.67±0.07	2.43±0.0	3.13±0.09	3.31±0.06
Flare 5	2.20±0.0	2.35±0.0	2.80±0.0	2.50±0.0	3.28±0.0	3.43±0.0
Flare 6	2.16±0.06	2.20±0.0	2.64±0.07	2.36±0.0	2.97±0.0	2.88±0.0

PMN J0948+0022

Fermi-LAT

State	Period[1]	Flux[2]	Photon index[3]	Test Statistic[4]
Flare 1	55368.1-55405.2	*3.58±0.27*	*2.53±0.07*	504.0
Flare 2	55717.4-55735.1	*4.13±0.39*	*2.62±0.10*	303.8
Steady	55898.1-55966.8	*1.11±0.14*	*2.63±0.11*	148.3
Flare 3	56055.4-	*2.36±0.24*	*2.59±0.10*	261.4
Flare 4	56227.5-56236.5	*5.17±0.58*	*2.66±0.12*	228.0
Flare 5	56290.0-56293.7	*12.66±1.33*	*2.59±0.11*	316.4

Swift-XRT

State	Exposure[5]	Flux[6]	Photon Index[7]	X^2_{red} $(d.o.f.)$[8]
Flare 1	*1556*	*5.01±0.51*	*1.64±0.12*	0.96(120)
Flare 2	*5161*	*3.70±0.23*	*1.61±0.07*	1.09(233)
Steady	*5212*	*3.35±0.23*	*1.59±0.08*	0.88(223)
Flare 3	*741.7*	*5.51±0.95*	*1.57±0.22*	0.71(62)
Flare 4	*2050*	4.38±0.46	*1.55±0.12*	0.97(117)
Flare 5	*721.7*	*14.80±1.28*	*1.65±0.11*	1.00(158)

Swift-UVOT

State	V[9]	B[9]	U[9]	W1[9]	M2[9]	W2[9]
Flare 1	*2.26±0.37*	*2.29±0.40*	*2.14±0.28*	2.24±0.23	2.55±0.31	*2.66±0.21*
Flare 2	*1.91±0.35*	*1.17±0.23*	2.04±0.19	1.84±0.16	2.20±0.19	*2.51±0.16*
Steady	-	-	*1.60±0.04*	-	-	-
Flare 3	-	*2.30±0.0*	-	-	-	-
Flare 4	-	-	*1.76±0.07*	-	-	-
Flare 5	*9.79±0.9*	*8.80±0.5*	*7.80±0.4*	5.53±0.2	9.28±0.6	*8.05±0.4*

SBS 0846+513				
Fermi-LAT				
State	Period[1]	Flux[2]	Photon index[3]	Test Statistic[4]
Flare 1	56064.6-56157.5	1.76 ± 0.10	2.11 ± 0.04	1499.3
Steady	56157.5-56392.7	0.24 ± 0.05	2.53 ± 0.15	61.13
Flare 2	56392.7-56448.9	1.37 ± 0.12	2.11 ± 0.06	689.2

Swift-XRT				
State	Exposure[5]	Flux[6]	Photon Index[7]	X^2_{red} $(d.o.f.)$[8]
Flare 1	4750	1.09 ± 0.18	1.35 ± 0.18	1.53 (76)
Steady	19140	0.39 ± 0.04	1.55 ± 0.13	1.17 (123)
Flare 2	7629	1.63 ± 0.16	1.36 ± 0.11	0.93 (174)

Swift-UVOT						
State	V[9]	B[9]	U[9]	W1[9]	M2[9]	W2[9]
Flare 1	0.56±0.1	0.35±0.5	0.12±0.03	0.16±0.01	0.16±0.01	0.15±0.01
Steady	3.45±0.13	2.58±0.12	1.67±0.09	0.90±0.0	0.98±0.0	0.77±0.0
Flare 2	5.68±0.16	3.56±0.13	2.37±0.0	1.42±0.05	1.39±0.06	1.24±0.03

Table 5.1: The SEDs summary of separated flare and steady periods of 1H 0323+342, PMN J0948+0022 and SBS 0846+513 denoted in Fig. 5.1, 5.2, and 5.3.

Notes:

1) Flares and steady states time intervals in MJD.

2) Integral γ-ray flux calculated for 0.1–300 GeV range in units of $10^{-7}\ photon\ cm^{-2}\ s^{-1}$.

3) Photon index obtained from γ-ray data analysis.

4) Test Statistic of the γ-ray data likelihood analysis.

5) Net exposure in seconds.

6) Unabsorbed X-ray integral flux calculated in 0.3–10 keV range in units of $10^{-12}\ erg\ cm^{-2}\ s^{-1}$ for PMN J0948+0022 and SBS 0846+513 and $10^{-11}\ erg\ cm^{-2}\ s^{-1}$ for 1H 0323+342.

7) Photon index obtained from X-ray analysis.

8) Reduced chi suqare of X-ray data analysis with C-statistic.

5.6 Theoretical Modeling of the SEDs in Flare and Steady States

Taking into account the similarities between the emission characteristics of NLSy1s and blazars, the multi-wavelength emission in the quiescent and flaring states are modeled using the synchrotron/Synchrotron Self-Compton (SSC) [172, 173] model. The radio through optical emission is due to the synchrotron emission of energetic electrons in the homogeneous, randomly oriented magnetic field, while the X-ray to HE γ-ray emission is due to the inverse Compton scattering of the same synchrotron photons.

	α	E'_{min} MeV	E'_{cut} GeV	E'_{max} TeV	B mG	L_{jet} $\times 10^{45} erg\ s^{-1}$
1H 0323+342						
Q (δ=10)	$2.49^{+0.07}_{-0.05}$	$4.87^{+8.53}_{-2.97}$	$5.24^{+0.66}_{-0.60}$	$2.81^{+4.28}_{-1.89}$	$244.23^{+23.83}_{-18.09}$	0.56
F1 (δ=15)	$1.90^{+0.06}_{-0.07}$	$4.60^{+3.56}_{-2.75}$	$4.57^{+0.50}_{-0.58}$	$5.93^{+7.97}_{-4.10}$	$32.77^{+1.98}_{-1.90}$	2.25
PMN J0948+0022						
Q (δ=10)	$1.93^{+0.11}_{-0.12}$	$56.62^{+32.29}_{-20.82}$	$3.02^{+0.60}_{-0.46}$	$4.65^{+6.86}_{-3.04}$	$237.06^{+17.00}_{-14.25}$	1.54
F5 (δ=15)	$1.75^{+0.12}_{-0.12}$	$95.81^{+22.53}_{-14.72}$	$3.16^{+0.70}_{-0.46}$	$5.69^{+10.84}_{-4.28}$	$107.41^{+7.97}_{-5.96}$	7.03
SBS 0846+513						
Q (δ=10)	$2.01^{+0.17}_{-0.14}$	$123.73^{+63.60}_{-74.71}$	$7.15^{+2.43}_{-1.52}$	$5.25^{+8.67}_{-3.88}$	$38.19^{+4.07}_{-4.51}$	1.90
F1 (δ=15)	$2.05^{+0.19}_{-0.18}$	$269.94^{+92.33}_{-105.40}$	$10.63^{+2.04}_{-1.76}$	$5.29^{+7.68}_{-3.42}$	$16.63^{+1.20}_{-1.09}$	8.20
F2 (δ=15)	$2.01^{+0.13}_{-0.13}$	$128.56^{+62.27}_{-66.02}$	$9.89^{+2.33}_{-1.83}$	$4.24^{+5.68}_{-3.14}$	$26.66^{+1.74}_{-1.58}$	5.79

Table 5.2: Model Parameters.

The emission region (the "blob") is assumed to be a sphere with a radius of R which carries a magnetic field with an intensity of B and a population of relativistic electrons which have a power-law with an exponential cut-off energy distribution, expected from shock acceleration

theories, [175] $N'_e(E'_e) = N'_0 (E'_e/m_e c^2)^{-\alpha} Exp[-E'_e/E'_{cut}]$ for $E'_{min} \leq E'_e \leq E'_{max}$, where E'_{min} and E'_{max} are the minimum and maximum electron energies, respectively.

For each source, the emitting region size has been calculated taking into account the flux doubling times given in Fig. 5.4. Since the blob moves along the jet with a bulk Lorentz factor of Γ_{bulk}, the radiation will be amplified by a relativistic Doppler factor of $\delta = 1/\Gamma_{bulk}(1 - \beta cos[\theta_{obs}])$, where θ_{obs} is the angle between the bulk velocity and the line of sight. We assumed that $\delta = 10$ in the quiescent state and then $\delta = 15$ during the flaring periods. These values have been chosen similar to the estimated mean bulk Lorentz factors of FSRQs obtained from the analysis of a large sample of γ-ray emitting FSRQs, [190] considering the similarities between FSRQs and NLSy1. The constraint of model parameters was performed by modified *naima* package [176] as described in section 4.4.

5.7 Results

The results of SEDs modeling are shown in Fig. 5.4, 5.5 and 5.6 with the corresponding parameters in Table 5.2. The radio emission is due to the low-energy electrons which are accumulated for longer periods, that is why, the radio data are treated as an upper limit for the purposes of our modeling.

The broadband SEDs of 1H 0323+342 in the quiescent and flaring states are shown in Fig. 5.5 (left panel). During the flare the X-ray spectra significantly hardened, $\Gamma_X = 1.72 \pm 0.04$ compared with $\Gamma_X = 1.91 \pm 0.10$ in the quiescent state accompanied by the increase of the X-ray flux from $F_X = (10.03 \pm 0.63) \times 10^{-12} erg\ cm^{-2}\ s^{-1}$ to $F_X = (28.32 \pm 0.88) \times 10^{-12} erg\ cm^{-2}\ s^{-1}$. Similar changes are observed also in the γ-ray band: the flux increased 18.2 times (during the flare it was $F_\gamma = (7.85 \pm 0.70) \times 10^{-7}\ photon\ cm^{-2}\ s^{-1}$) and the photon index changed from $\alpha = 3.02 \pm 0.21$ to $\alpha = 2.67 \pm 0.10$. In the quiescent state the emission can be explained, assuming $\alpha = 2.49 \pm 0.06$ and $E_{cut} = (52.40 \pm 6.30)$ GeV (observer frame) for the underlying electron distribution. While in the modeling of a flaring state, harder $\alpha = 1.90 \pm 0.07$ and higher $E_{cut} = (68.55 \pm 8.10)$ GeV (observer frame) are needed. This change in α is due to the X-ray spectrum hardening and the increase of Ecut can explain the shift of the γ-ray spectrum to higher energies. The total jet luminosity

$(L_{jet} = L_e + L_B)$ is $L_{jet} = 0.56 \times 10^{45}\, erg\, s^{-1}$ in the quiescent state and $L_{jet} = 2.25 \times 10^{45}\, erg\, s^{-1}$ in the flaring period.

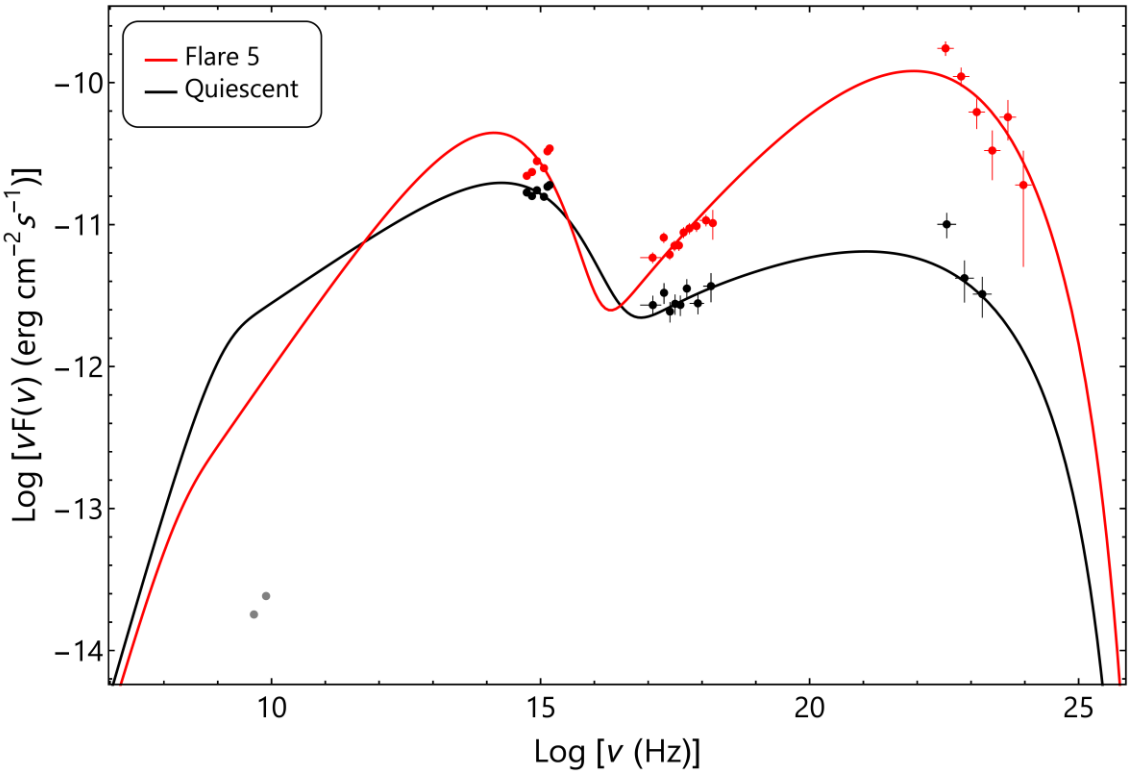

Figure 5.5: The broad band SED of 1H 0323+342 in the flaring and quiescent states.

The multiwavelength SED of PMN J0948+0022 observed during quiescent (black) and flaring states (blue) is shown in Fig. 5.6. Among many flares observed during the considered time, almost all of them had rather similar γ-ray photon indices $\alpha = (2.34 - 2.52)$ but different fluxes. We chose the flare from MJD 56290.0 to MJD 56293.7, when the γ-ray flux was almost to its maximum. During this period, the X-ray photon index hardened $(\Gamma_X = 1.65 \pm 0.11)$ and the flux increased $(14.80 \pm 1.28) \times 10^{-12} erg\, cm^{-2}\, s^{-1}$ as compared with quiescent state $\Gamma_X = 1.59 \pm 0.08$ and $(3.35 \pm 0.23) \times 10^{-12} erg\, cm^{-2}\, s^{-1}$. If the power-law index of the electrons is $\alpha = 1.93 \pm 0.12$ with $E_{cut} = (30.19 \pm 5.32)$ GeV (observer frame) and $\alpha = 1.75 \pm 0.12$ with $E_{cut} = (47.33 \pm 5.93)$ GeV (observer frame), for the quiescent and flaring states respectively, the emission in the X- and γ-ray band can be explained by SSC emission from the electron population producing the radio to optical emission in the jet. When the emission in the quiescent state is modeled $(\delta = 10)$, as the emitting region size is small, the magnetic field should be larger $B = 0.24 \pm 0.02$ G to

account for the observed data, while at δ = 15 the magnetic field is weaker, $B = 0.11 \pm 0.01$ G. The jet total luminosity, $L_{jet} = 1.54 \times 10^{45}\ erg\ s^{-1}$, increases up to $L_{jet} = 7.03 \times 10^{45}\ erg\ s^{-1}$ during the flare.

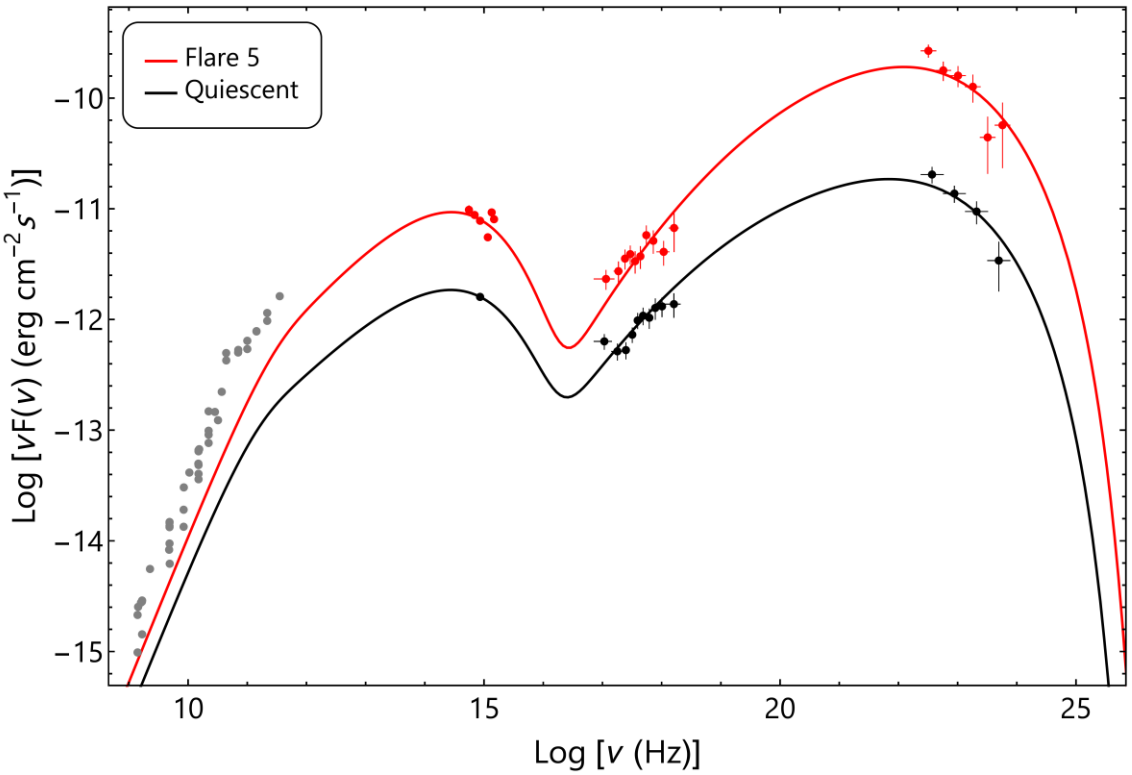

Figure 5.6: The broad band SED of PMN J0948+0022 in the flaring and quiescent states.

The broadband spectrum of SBS 0846+513 is shown in Fig. 5.7 for quiescent (gray) and flaring states (Flare 1 (blue) and Flare 2 [red]). During the flaring states the X-ray photon index slightly hardened ($\Gamma_X = 1.35 \pm 0.18$ for Flare 1 and $\Gamma_X = 1.36 \pm 0.11$ for Flare 2) as compared with the quiescent state ($\Gamma_X = 1.55 \pm 0.13$). Due to large uncertainties, the power-law index of underlying electrons does not change significantly and $\alpha = 2.00 \pm 0.1$ well explains the observed data in both states. A similar photon index hardening is observed also in the γ-ray band when comparing quiescent and flaring states ($\Gamma = 2.53 \pm 0.15$ versus $\Gamma = 2.11 \pm 0.05$), which resulted in that the cut-off is shifted to higher energies, e.g., $E_{cut} = 71.53 \pm 20.26$ GeV in the quiescent and $E_{cut} = (148.35 - 159.45)$ GeV in the flaring states (both in the observer frame). In the modeling the magnetic field should be changed in accordance with the changes of the flux observed in the X-ray band (2.5-3.5 times), and it is $B = (16.63 \pm 1.14)$ mG in the quiescent and $B = (26.66 - 38.19)$ mG in

the flaring states. The total jet luminosity is particle dominated, with $L_{jet} = 1.90 \times 10^{45} erg\ s^{-1}$ in the quiescent state, and it increases up to $L_{jet} = (5.79 - 8.20) \times 10^{45} erg\ s^{-1}$ during the flares.

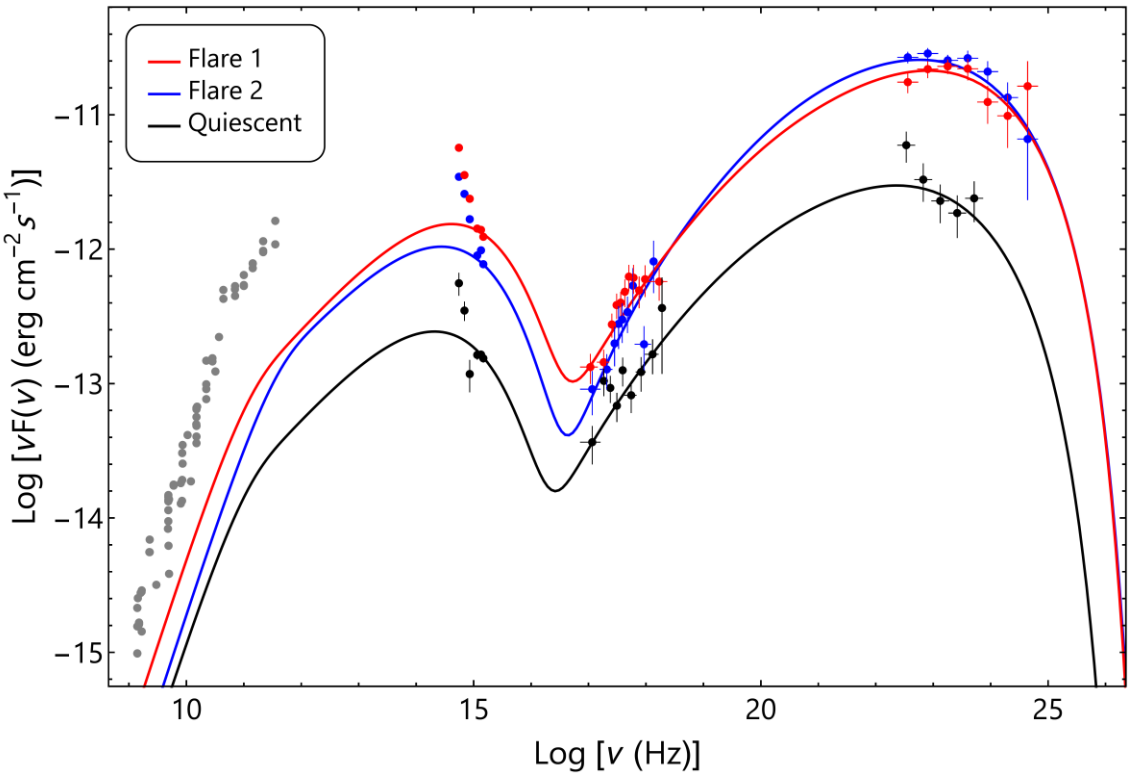

Figure 5.7: The broad band SED of SBS 0846+513 in the flaring and quiescent states.

The modeling presented above illustrates that the one-zone synchrotron/SSC model can successfully explain the observed multiwavelength emission from 1H0323+342, PMN J0948+0022 and SBS 0846+513. The hard X-ray photon index implies a hard power-law index also for the electrons $\alpha \leq 2.0$ and from the γ-ray data, the cut-off energy is $E_{cut} \geq 50\ GeV$. This implies that the emission is dominated by the emission from freshly accelerated electrons, which are effectively accelerated up to/above TeV energies. The jet total luminosity required for modeling, $L_{jet} \simeq (1 - 8) \times 10^{45}\ erg\ s^{-1}$ which is almost of the same order as the Eddington accretion power, $L_{Edd} = (10^{45} - 10^{46}) erg\ s^{-1}$ for the black hole mass of $(10^7 - 10^8) M_{\odot}$, which implies that the total jet luminosity is effectively converted to emission in the jets of NLSy1s.

CONCLUSION

AGNs are among the most powerful sources of the Universe and their studies allow not only understanding the physical processes and their formation, but also the Universe at large distances. Since their discovery, AGNs were always studied in different bands, but rapid development was in recent years, when simultaneous operations of many telescopes in different band allowed studying the spectral properties from radio ($\sim 10^7$ Hz) to VHE γ-ray ($\sim 10^{27}$ Hz) bands. These multiwavelength studies provided chance not only to apply the known theories, but also new and unknown features were discovered. The high quality data from the observation allowed to examine the emission processes, which supported the investigation of dynamic changes in these sources.

Studies of AGNs are especially important in the HE γ-ray band for several reasons. First of all, most of the AGN jet energy is released in the γ-ray band, so the most extreme features of AGNs can be investigated. The emission from AGNs is continuously monitored since August 2008, which is crucial to understanding the origin of their variable emission. Moreover, the γ-ray data are necessary to fully understand the nature of the HE MeV/GeV emission component in the AGN spectrum. Indeed, the recent observations in the γ-ray band were crucial for identifying new γ-ray emitting AGNs as well as in understanding the emission processes. For example, Fermi-LAT observations showed, that together with blazars the AGNs with higher jet inclination angle (e.g, radiogalaxies) are another and very important class of γ-ray emission. On the other hand, the single source studies revealed that energy released in the γ-ray band sometimes can exceed the maximum available energy of the central source (Eddington power).

In this thesis, the γ-ray emission properties of up to now in the γ-ray band detected 27 non-blazar AGNs, including eleven FRI and ten FRII radiogalaxies/SSRQs and five NLSy1s were investigated using available most recent 7-years data. Such studies are intended to determine the general properties in non-blazar AGNs, moreover the comparison with blazars features allow us to understand the main difference between blazar and non-blazar AGNs in the γ-ray band. Also, emissions features of two well known objects NGC 1275 (the most bright radiogalaxy in the MeV/GeV band) and PKS 0625-35 (one of the radiogalaxies

also detected in VHE γ-ray band so far) were studied. Especially, HE emission features in recently detected NLSy1 sources were discussed in detail.

The main results by chapters are:

In chapter 1 the types of the AGNs discussed in the thesis with their properties, Swift UVOT/XRT and Fermi-LAT observed data analyses methods and steps as well as the main radiation mechanisms are described.

In chapter 2 the spectral and temporal properties of γ-ray emission from non-blazar AGNs using the recent *Fermi*-LAT observational data were investigated. It was shown that non-blazar AGNs have a γ-ray photon index in the range of 1.84 – 2.86 described with power-law model and a flux varying from a few times $10^{-9}\,photon\,cm^{-2}\,s^{-1}$ to $10^{-7}\,photon\,cm^{-2}\,s^{-1}$. Over long time periods, power-law provided an adequate description of the γ-ray spectra of almost all sources. Significant curvature was observed in the γ-ray spectra of NGC 1275, NGC 6251, SBS 0846+513 and PMN J0948+0022. In these cases alternative log-parabola or power-law with exponential cut-off models gave better descriptions of their spectra. The γ-ray spectra of PKS 0625-25 and 3C 380 showed a possible deviation from a simple power-law shape, indicating a spectral cutoff around the observed photon energy of $E_{cut} = 131.2 \pm 88.04$ GeV and $E_{cut} = 55.57 \pm 50.74$ GeV, respectively. Our analysis confirmed the previous finding of an unusual spectral turnover in the γ-ray spectrum of Cen A: the photon index changes from $\Gamma = 2.75 \pm 0.02$ to 2.31 ± 0.1 at 2.35 ± 0.08 GeV. In the $\Gamma - L_\gamma$ plane, the luminosities of non-blazar AGNs are spread from $1.12 \times 10^{41}\,erg\,s^{-1}$ to $7.85 \times 10^{46}\,erg\ s^{-1}$, where FRI radiogalaxies have the lowest luminosities (but typically appear with a harder photon index) and SSRQs/NLSy1s sources show the highest luminosities (with softer photon indexes). We confirm the previously reported short-timescale flux variability of NGC 1275 and 3C 120. The γ-ray emission from NLSy1s, 1H 0323+342, SBS 0846+513 and PMN J0948+0022, is variable, showing flares in short scales sometimes accompanied by a moderate hardening of their spectra (e.g., on MJD 56146.8 the γ-ray photon index of SBS 0846+513 was $\Gamma = 1.73 \pm 0.14$). In the case of 3C 111, Cen A core, 3C 207, 3C 275.1, 3C 380, 4C+39.23B, PKS 1502+036 and PKS 2004-447 long-timescale flux variability in the γ-ray band was detected.

In chapter 3 a detailed analysis of the γ-ray light curve of NGC 1275 using the Fermi-LAT data accumulated in 2008-2017 was performed. Major γ-ray flares were observed in October 2015 and December 2016/January 2017, when the source reached a daily peak flux of $(2.21 \pm 0.26) \times 10^{-6}\, photon\, cm^{-2}\, s^{-1}$ and the maximum flux of $(3.48 \pm 0.87) \times 10^{-6}\, photon\, cm^{-2}\, s^{-1}$ was detected within 3 hours, which corresponds to an apparent isotropic γ-ray luminosity of $\simeq 3.84 \times 10^{45} erg\, s^{-1}$. The most rapid flare had e-folding time as short as 1.21 ± 0.22 hours, which has never been previously observed from any radiogalaxy in γ-ray band. Also γ-ray spectral changes were observed during these flares: in the flux versus photon index plane the spectral evolution follows correspondingly a counter clockwise and a clockwise loop inferred from the light curve generated by an adaptive binning method. On December 30, 2016 and January 01, 2017 the X-ray photon index softened ($\Gamma_X \simeq 1.75 - 1.77$) and the flux increased nearly ~ 3 times as compared with the quiet state. The observed hour-scale variability suggests a very compact emission region ($R_\gamma \leq 5.22 \times 10^{14}\, (\delta/4)$ cm) implying that the observed emission is most likely produced in the sub parsec-scale of jet, if the entire jet width is responsible for the emission. During the active periods the γ-ray photon index hardened, shifting the peak of the HE spectral component to >GeV, making it difficult to explain the observed X-ray and γ-ray data in the standard one-zone synchrotron self-Compton model.

In chapter 4 the γ-ray emission from the radiogalaxy PKS 0625-35 was investigated using the Fermi LAT data accumulated during 2008-2017. γ-ray radiation up to 100 GeV has been detected with a detection significance of about 32.3σ. A power-law spectrum with a photon index of 1.88 ± 0.04 and an integrated flux of $F_{>100\, MeV} = (1.02 \pm 0.10)\, 10^{-8}\, photon\, cm^{-2}\, s^{-1}$, above 100 MeV well describes the data averaged over 9 years of observations. There is a hint of deviation from a simple power-law shape around tens of GeV energies; however, the low statistics does not allow to reject power-law model. The spectral energy distributions during high and low X-ray states are modeled using one-zone leptonic models that include the synchrotron, synchrotron self Compton processes; the model parameters were estimated using the Markov Chain Monte

Carlo method. The modeling shows that the particles (electrons) of PKS 0625-35 jet are accelerated to energies higher than 50 TeV.

In chapter 5 the multiwavelength emission properties of 1H 0323+342, SBS 0846+513 and PMN J0948+0022 NLSy1 galaxies were discussed, using the γ-ray data from the last 8.8 years Fermi-LAT observations as well as available Swift(UVOT/XRT) data. The temporal analyses showed that γ-ray radiation is produced in a compact region (smaller than several 10^{16}) and one-zone synchrotron/synchrotron self-Compton model can satisfactorily reproduce their observed broadband spectra.

BIBLIOGRAPHY

1. Urry C. M., Padovani P., “Unified Schemes for Radio-Loud Active Galactic Nuclei”, Publications of the Astronomical Society of the Pacific, v.107, p.803, (1995).

2. Beckmann, V. & Shrader, C. R., “The AGN phenomenon: open issues”, Proceedings of "An INTEGRAL view of the high-energy sky (the first 10 years)", (2012).

3. Fanaroff, B. L. & Riley, J. M., “The morphology of extragalactic radio sources of high and low luminosity”, Monthly Notices of the Royal Astronomical Society, Vol. 167, p. 31P-36P (1974).

4. Laing, R. A. & Bridle, A. H., “Rotation measure variation across M84” Monthly Notices of the Royal Astronomical Society (ISSN 0035-8711), vol. 228, p. 557-571, (1987).

5. Bridle et al., “Deep VLA imaging of twelve extended 3CR quasars”, The Astronomical Journal, vol. 108, no. 3, p. 766-820, (1994).

6. Peackock J. A., Wall J. V., “Bright extragalactic radio sources at 2.7 GHz. II - Observations with the Cambridge 5-km telescope”, Monthly Notices of the Royal Astronomical Society, vol. 198, p. 843-860, (1982).

7. Wilkinson P. N., Polatidis A. G., Readhead A. C. S., Xu W., Pearson T. J., “Two-sided ejection in powerful radio sources: The compact symmetric objects”, Astrophysical Journal, Part 2 - Letters (ISSN 0004-637X), vol. 432, no. 2, p. L87-L90, (1994).

8. Fanti et al., “Are compact steep-spectrum sources young?”, Astronomy and Astrophysics, v.302, p.317, (1995).

9. Murgia, M., Fanti, C., Fanti, R., et al., “Synchrotron spectra and ages of compact steep spectrum radio sources”, Astronomy and Astrophysics, v.345, p.769-777 (1999).

10. Liu, Y., Jiang, D. R., & Gu, M. F., “The Jet Power, Radio Loudness, and Black Hole Mass in Radio-loud Active Galactic Nuclei”, The Astrophysical Journal, Volume 637, Issue 2, pp. 669-681, (2006).

11. Gu, M. F., & Ai, Y. L., “The optical variability of steep-spectrum radio quasars in the SDSS stripe 82 region”, Astronomy & Astrophysics, Volume 534, id. A59, 9 pp., (2011).

12. Khachikian, E. Y. and Weedman, D. W., “An atlas of Seyfert galaxies”, Astrophysical Journal, vol. 192, pt. 1, p. 581-589, (1974).

13. Osterbrock D. E., Pogge R. W., “The spectra of narrow-line Seyfert 1 galaxies”, Astrophysical Journal, Part 1 (ISSN 0004-637X), vol. 297, p. 166-176, (1985).

14. Leighly, K. M., “A Comprehensive Spectral and Variability Study of Narrow-Line Seyfert 1 Galaxies Observed by ASCA. I. Observations and Time Series Analysis”, The Astrophysical Journal Supplement Series, Volume 125, Issue 2, pp. 297-316, (1999).

15. Pounds, K. A., Done, C., & Osborne, J. P., “RE 1034+39: a high-state Seyfert galaxy?”, Monthly Notices of the Royal Astronomical Society, Volume 277, Issue 1, pp. L5-L10, (1995).

16. Abdo, A. A., Ackermann, M., & et al., “Radio-Loud Narrow-Line Seyfert 1 as a New Class of Gamma-Ray Active Galactic Nuclei”, The Astrophysical Journal Letters, Volume 707, Issue 2, pp. L142-L147 (2009).

17. D’Ammando, F., Orienti, M., Finke, J., “SBS 0846+513: a new γ-ray-emitting narrow-line Seyfert 1 galaxy’, Monthly Notices of the Royal Astronomical Society, Volume 426, Issue 1, pp. 317-329, (2012).

18. Peterson, B. M., McHardy, I. M., Wilkes, B. J., et al., “X-Ray and Optical Variability in NGC 4051 and the Nature of Narrow-Line Seyfert 1 Galaxies”, The Astrophysical Journal, Volume 542, Issue 1, pp. 161-174, (2000).

19. Paliya, V. S., & Stalin, C. S., “The First GeV Outburst of the Radio-loud Narrow-line Seyfert 1 Galaxy PKS 1502+036”, The Astrophysical Journal, Volume 820, Issue 1, article id. 52, 8 pp. (2016).

20. Kotilainen, J. K., Le′on-Tavares, J., Olgu′in-Iglesias, A., et al., “Discovery of a Pseudobulge Galaxy Launching Powerful Relativistic Jets”, The Astrophysical Journal, Volume 832, Issue 2, article id. 157, 8 pp. (2016).

21. Dermer, C. D., “Rapid X-Ray Declines and Plateaus in Swift GRB Light Curves Explained by a Highly Radiative Blast Wave”, The Astrophysical Journal, Volume 664, Issue 1, pp. 384-396, (2016).

22. Finke, J.D., Dermer, C.D., & B¨ottcher, M., “Synchrotron Self-Compton Analysis of TeV X-Ray-Selected BL Lacertae Objects”, The Astrophysical Journal, Volume 686, Issue 1, pp. 181-194 (2008).

23. Blumenthal, G. R., & Gould, R. J., “Bremsstrahlung, Synchrotron Radiation, and Compton Scattering of High-Energy Electrons Traversing Dilute Gases”, Reviews of Modern Physics, vol. 42, Issue 2, pp. 237-271, (1970).

24. Jones, T. W., O’Dell, S. L., Stein, W. A., “Physics of Compact Nonthermal Sources. I. Theory of Radiation Processes”, Astrophysical Journal, Vol. 188, pp. 353-368 (1974).

25. Gehrels, N., “The Swift Gamma-Ray Burst Mission”, The Astrophysical Journal, Volume 611, Issue 2, pp. 1005-1020, (2004).

26. Moretti et al., “In-flight calibration of the Swift XRT Point Spread Function”, V, X-Ray, and Gamma-Ray Space Instrumentation for Astronomy XIV. Edited by Siegmund, Oswald H. W. Proceedings of the SPIE, Volume 5898, pp. 360-368 (2005).

27. Atwood, W. B., Abdo, A. A., Ackermann, M., et al., “The Large Area Telescope on the Fermi Gamma-Ray Space Telescope Mission”, The Astrophysical Journal, Volume 697, Issue 2, pp. 1071-1102 (2009).

28. Acero, F., & et al., “Fermi Large Area Telescope Third Source Catalog”, The Astrophysical Journal Supplement Series, Volume 218, Issue 2, article id. 23, 41 pp. (2015).

29. Mattox, J. R. & Bertsch, D. L. et al., “The Likelihood Analysis of EGRET Data”, Astrophysical Journal v.461, p.396, (1996).

30. Lott, B., Escande, L., Larsson, S., & Ballet, J. “An adaptive-binning method for generating constant-uncertainty/constant-significance light curves with Fermi-LAT data”, Astronomy & Astrophysics, Volume 544, id. A6, 12 pp., (2012).

31. Abdo, A., & et al., “Gamma-ray Light Curves and Variability of Bright Fermi-detected Blazars”, The Astrophysical Journal, Volume 722, Issue 1, pp. 520-542 (2010).

32. P. Kalberla, W. Burton, & et al., “The Leiden/Argentine/Bonn (LAB) Survey of Galactic HI. Final data release of the combined LDS and IAR surveys with improved stray-radiation corrections”, Astronomy and Astrophysics, Volume 440, Issue 2, pp.775-782, (2005).

33. Morrison, R. & McCammon, D., “Interstellar photoelectric absorption cross sections, 0.03-10 keV”, Astrophysical Journal, Part 1 (ISSN 0004-637X), vol. 270, p. 119-122, (1983).

34. Fitzpatrick, N., “Correcting for the Effects of Interstellar Extinction”, The Publications of the Astronomical Society of the Pacific, Volume 111, Issue 755, pp. 63-75, (1999).

35. Schlafly, E. F., and Finkbeiner, D. P., “Measuring Reddening with Sloan Digital Sky Survey Stellar Spectra and Recalibrating SFD”, The Astrophysical Journal, Volume 737, Issue 2, article id. 103, 13 pp. (2011).

36. Poole, T. S., Breeveld, A. A., Page, M. J., et al., “Photometric calibration of the Swift ultraviolet/optical telescope”, Monthly Notices of the Royal Astronomical Society, Volume 383, Issue 2, pp. 627-645, (2008).

37. Breeveld, A. A., Landsman, W. et al., “An Updated Ultraviolet Calibration for the Swift/UVOT”, GAMMA RAY BURSTS 2010. AIP Conference Proceedings, Volume 1358, pp. 373-376 (2011).

38. Aharonian, F., & et al., “An Exceptional Very High Energy Gamma-Ray Flare of PKS 2155-304”, The Astrophysical Journal, Volume 664, Issue 2, pp. L71-L74, (2007).

39. Brown, A. M., “Locating the γ-ray emission region of the flat spectrum radio quasar PKS 1510-089”, Monthly Notices of the Royal Astronomical Society, Volume 431, Issue 1, p.824-835, (2013).

41. Abdo, A. A., & et al., “Fermi Large Area Telescope View of the Core of the Radiogalaxy Centaurus A”, The Astrophysical Journal, Volume 719, Issue 2, pp. 1433-1444 (2010).

42. Abdo, A., & et al., “Fermi Large Area Telescope Gamma-Ray Detection of the Radiogalaxy M87”, The Astrophysical Journal, Volume 707, Issue 1, pp. 55-60 (2009).

43. Abdo, A. A., Ackermann, M., & et al., “Fermi Discovery of Gamma-ray Emission from NGC 1275”, The Astrophysical Journal, Volume 699, Issue 1, pp. 31-39 (2009).

44. Abdo, A. A., Ackermann, M., et al., “Fermi Large Area Telescope First Source Catalog”, The Astrophysical Journal Supplement, Volume 188, Issue 2, pp. 405-436 (2010).

45. Abdo, A. A., Ackermann, M., & et al., “Fermi Large Area Telescope Observations of Misaligned Active Galactic Nuclei”, The Astrophysical Journal, Volume 720, Issue 1, pp. 912-922 (2010).

46. Abdo, A. A., Ackermann, M., & et al., “Fermi Gamma-Ray Imaging of a Radio Galaxy”, Science, Volume 328, Issue 5979, pp. 725- (2010).

47. Ackermann, M., Ajello, M., & et al., “Fermi Large Area Telescope Detection of Extended Gamma-Ray Emission from the Radiogalaxy Fornax A”, The Astrophysical Journal, Volume 826, Issue 1, article id. 1, 9 pp. (2016).

48. Kataoka, J., Stawarz, £., Cheung, C. C., et al., “γ-ray Spectral Evolution of NGC 1275 Observed with Fermi Large Area Telescope”, The Astrophysical Journal, Volume 715, Issue 1, pp. 554-560 (2010).

49. Baghmanyan, V., Gasparyan, S., & Sahakyan, N., “Rapid Gamma-Ray Variability of NGC 1275”, The Astrophysical Journal, Volume 848, Issue 2, article id. 111, 8 pp. (2017).

50. Sahakyan, N.; Yang, R.; Aharonian, F. A.; Rieger, F. M., “Evidence for a Second Component in the High-energy Core Emission from Centaurus A?”, The Astrophysical Journal Letters, Volume 770, Issue 1, article id. L6, 5 pp. (2013).

51. Grandi, P., Torresi, E., & Stanghellini, C., “The γ-Ray Emission Region in the Fanaroff-Riley II Radiogalaxy 3C 111”, The Astrophysical Journal Letters, Volume 751, Issue 1, article id. L3, 5 pp. (2012).

52. Casadio, C., Gómez, J. L., Grandi, P., et al., “The Connection between the Radio Jet and the Gamma-ray Emission in the Radiogalaxy 3C 120”, The Astrophysical Journal, Volume 808, Issue 2, article id. 162, 11 pp. (2015).

53. Lenain, J., Boisson, C., Sol, H., and Katarzy′nski, K., “A synchrotron self-Compton scenario for the very high energy γ-ray emission of the radiogalaxy M 87. Unifying the TeV emission of blazars and other AGNs?”, Astronomy and Astrophysics, Volume 478, Issue 1, pp.111-120, (2008).

54. Janiak, M., Sikora, M., & Moderski, R., “Application of the spine-layer jet radiation model to outbursts in the broad-line radiogalaxy 3C 120”, Monthly Notices of the Royal Astronomical Society, Volume 458, Issue 3, p.2360-2370, (2016).

55. Tavecchio, F., and Ghisellini, G., “On the spine-layer scenario for the very high-energy emission of NGC 1275”, Monthly Notices of the Royal Astronomical Society, Volume 443, Issue 2, p.1224-1230, (2014).

56. Angioni, R., Grandi, P., Torresi, E., Vignali, C., & Knödlseder, J., “Radio galaxies with the Cherenkov Telescope Array”, Astroparticle Physics, Volume 92, p. 42-48, (2017).

57. Sahakyan, N.; Baghmanyan, V.; Zargaryan, D., “Fermi-LAT Observation of Non-Blazar AGNs”, Astronomy & Astrophysics, doi: 10.1051/0004-6361/201732304, (2018).

58. Ackermann, M., Ajello, M., & et al., “The Third Catalog of Active Galactic Nuclei Detected by the Fermi Large Area Telescope”, The Astrophysical Journal, Volume 810, Issue 1, article id. 14, 34 pp. (2015).

59. Gelderman, R. & Whittle, M., “An optical study of compact steep-spectrum radio sources. 1: The spectroscopic data”, Astrophysical Journal Supplement Series (ISSN 0067-0049), vol. 91, no. 2, p. 491-50, (1994).

60. Gallo, L. C. “Investigating the nature of narrow-line Seyfert 1 galaxies with high-energy spectral complexity”, Monthly Notices of the Royal Astronomical Society, Volume 368, Issue 1, pp. 479-486, (2006).

61. Ferrarese, L. et al., “The Discovery of Cepheids and a Distance to NGC 5128”, The Astrophysical Journal, Volume 654, Issue 1, pp. 186-218, (2007).

62. Burns, J. et al., “The inner radio structure of Centaurus A - Clues to the origin of the jet X-ray emission”, Astrophysical Journal, Part 1 (ISSN 0004-637X), vol. 273, p.128-153, (1983).

63. Cappellari M., Neumayer N., Reunanen J., van der Werf P. P., de Zeeuw P. T., & Rix H.-W, “The mass of the black hole in Centaurus A from SINFONI AO-assisted integral-field observations of stellar kinematics”, Monthly Notices of the Royal Astronomical Society, Volume 394, Issue 2, pp. 660-674, (2009).

64. Israel, F. P., “Centaurus A - NGC 5128”, The Astronomy and Astrophysics Review, Volume 8, Issue 4, pp. 237-278 (1998).

65. Aharonian F. et al. (H.E.S.S. collaboration), “Discovery of Very High Energy γ-Ray Emission from Centaurus a with H.E.S.S.”, The Astrophysical Journal Letters, Volume 695, Issue 1, pp. L40-L44 (2009).

66. Roustazadeh, P., & Bottcher, M., “Very High Energy Gamma-ray-induced Pair Cascades in the Radiation Fields of Dust Tori of Active Galactic Nuclei: Application to Cen A”, The Astrophysical Journal, Volume 728, Issue 2, article id. 134, 5 pp. (2011).

67. Smith, R. J., Lucey, J. R., Hudson, M. J., et al., “Streaming motions of galaxy clusters within 12000km s-1 - I. New spectroscopic data”, Monthly Notices of the Royal Astronomical Society, Volume 313, Issue 3, pp. 469-490, (2000).

68. Gavazzi, G., Perola, C. G., & Jaffe, W., “Observations of the head-tail radiogalaxy NGC 3862 /3C 264/ at 0.6, 1.4, and 5.0 GHz”, Astronomy and Astrophysics, vol. 103, no. 1, p. 35-43, (1981).

69. Lara, L., Cotton, W. D., Feretti, L., et al., “VLBI Observations of a Complete Sample of Radio Galaxies. VII. Study of the FR I Sources 3C 31, 4C 35.03, and 3C 264”, The Astrophysical Journal, Volume 474, Issue 1, pp. 179-187, (1997).

70. Gómez, J., et al., “Flashing Superluminal Components in the Jet of the Radiogalaxy 3C120”, Science, Volume 289, Issue 5488, pp. 2317-2320 (2000).

71. Chatterjee, R., Marscher, A., Jorstad, S., et al., “Disk-Jet Connection in the Radiogalaxy 3C 120”, The Astrophysical Journal, Volume 704, Issue 2, pp. 1689-1703 (2009).

72. Sahakyan, N., Zargaryan, D., & Baghmanyan, V., “On the gamma-ray emission from 3C 120”, Astronomy & Astrophysics, Volume 574, id. A88, 5 pp., (2015).

73. Parma P., Fanti C., Fanti R., Morganti R., de Ruiter H. R., “VLA observations of low-luminosity radio galaxies. VI - Discussion of radio jets”, Astronomy and Astrophysics (ISSN 0004-6361), vol. 181, no. 2, p. 244-264, (1987).

74. Capetti, A., Morganti, R., Parma, P., & Fanti, R., “Polarization in low luminosity radio galaxies”, Astronomy and Astrophysics Supplement Series (ISSN 0365-0138), vol. 99, no. 3, p. 407-435, (1993).

75. West, R. M., & Tarenghi, M., “The optical counterpart of the strong southern radio source PKS 1343-601 (13S6A)”, Astronomy and Astrophysics (ISSN 0004-6361), vol. 223, no. 1-2, p. 61-65, (1989).

76. Jones, P. A., Lloyd, B. D., & McAdam, W. B., “The radiogalaxy Centaurus B”, Monthly Notices of the Royal Astronomical Society, Volume 325, Issue 2, pp. 817-825, (2001).

77. Laing, R. A., Guidetti, D., Bridle, A. H., Parma, P., & Bondi, M., “Deep imaging of Fanaroff-Riley Class I radio galaxies with lobes”, Monthly Notices of the Royal Astronomical Society, Volume 417, Issue 4, pp. 2789-2808, (2011).

78. Tashiro, M., Kaneda, H., Makishima, K., et al., “Evidence of Energy Nonequipartition between Particles and Fields in Lobes of the Radiogalaxy PKS 1343-601 (Centaurus B)”, The Astrophysical Journal, Volume 499, Issue 2, pp. 713-718, (1998).

79. Marshall, H. L., Schwartz, D. A., Lovell, J. E. J., et al., “A Chandra Survey of Quasar Jets: First Results”, The Astrophysical Journal Supplement Series, Volume 156, Issue 1, pp. 13-33, (2005).

80. Tashiro, M., Isobe, N., Suzuki, M., et al., “Extended X-ray Emissions from the Radiogalaxy Centaurus B”, X-Ray and Radio Connections (eds. L.O. Sjouwerman and K.K Dyer) Published electronically by NRAO, (2005).

81. Ackermann, M., Ajello, M., Allafort, A., et al., "The Second Catalog of Active Galactic Nuclei Detected by the Fermi Large Area Telescope", The Astrophysical Journal, Volume 806, Issue 1, article id. 144, 3 pp. (2015).

82. Katsuta, J., Tanaka, Y. T., Stawarz, L., et al., “Fermi-LAT and Suzaku observations of the radiogalaxy Centaurus B”, Astronomy & Astrophysics, Volume 550, id. A66, 11 pp., (2013).

83. Gebhardt, K., Adams, J., Richstone, D., et al., “The Black Hole Mass in M87 from Gemini/NIFS Adaptive Optics Observations”, The Astrophysical Journal, Volume 729, Issue 2, article id. 119, 13 pp. (2011).

84. Bird, S., Harris, W. E., Blakeslee, J. P., & Flynn, C. “The inner halo of M 87: a first direct view of the red-giant population”, Astronomy and Astrophysics, Volume 524, id. A71, 9 pp., (2010).

85. Marshall, H. L., Miller, B. P., Davis, D. S., et al., “A High-Resolution X-Ray Image of the Jet in M87”, The Astrophysical Journal, Volume 564, Issue 2, pp. 683-687, (2002).

86. Biretta, J. A., Sparks, W. B., & Macchetto, F., “Hubble Space Telescope Observations of Superluminal Motion in the M87 Jet”, The Astrophysical Journal, Volume 520, Issue 2, pp. 621-626, (1999).

87. Aharonian F., Akhperjanian, A., & et al., “Is the giant radiogalaxy M 87 a TeV gamma-ray emitter?”, Astronomy and Astrophysics, v.403, p. L1-L5 (2003).

88. Sun, Xiao-Na; Yang, Rui-Zhi; Rieger, Frank M.; Liu, Ruo-yu; Aharonian, Felix, “The energy distribution of relativistic electrons in the kilo-parsec scale jet of M87 with Chandra”, eprint arXiv:1712.06390, (2017)

89. Aharonian, F. A., “Proton-synchrotron radiation of large-scale jets in active galactic nuclei”, Monthly Notices of the Royal Astronomical Society, Volume 332, Issue 1, pp. 215-230, (2002).

90. Zhang, J., Bai, J. M., Chen, L., & Liang, E., X-ray Radiation Mechanisms and Beaming Effect of Hot Spots and Knots in Active Galactic Nuclear Jets, The Astrophysical Journa, 710, 1017, (2010).

91. Wegner, G., Bernardi, M., Willmer, C. N. A., et al., "Redshift-Distance Survey of Early-Type Galaxies: Spectroscopic Data", The Astronomical Journal, Volume 126, Issue 5, pp. 2268-2280, (2003).

92. Waggett, P. C., Warner, P. J., & Baldwin, J. E., "NGC 6251, a very large radiogalaxy with an exceptional jet", Monthly Notices of the Royal Astronomical Society, vol. 181, Nov. 1977, p. 465-474, (1977).

93. Perley, R. A., Bridle, A. H., & Willis, A. G., "High-resolution VLA observations of the radio jet in NGC 6251", Astrophysical Journal Supplement Series (ISSN 0067-0049), vol. 54, p. 291-334, (1984).

94. Schoenmakers, A. P., de Bruyn, A. G., Rottgering, H. J. A., & van der Laan, H., "A new sample of giant radio galaxies from the WENSS survey. I. Sample definition, selection effects and first results", Astronomy and Astrophysics, v.374, p.861-870, (2001).

95. Takeuchi, Y., Kataoka, J., Stawarz, Ł., et al., "Suzaku X-Ray Imaging of the Extended Lobe in the Giant Radiogalaxy NGC 6251 Associated with the Fermi-LAT Source 2FGL J1629.4+8236", The Astrophysical Journal, Volume 749, Issue 1, article id. 66, 8 pp. (2012).

96. Abdo A. A., Ackermann, M., et al., "The First Catalog of Active Galactic Nuclei Detected by the Fermi Large Area Telescope", The Astrophysical Journal, Volume 715, Issue 1, pp. 429-457 (2010).

97. Migliori, G., Grandi, P., Torresi, E., et al., "Implications for the structure of the relativistic jet from multiwavelength observations of NGC 6251", Astronomy & Astrophysics, Volume 533, id. A72, 11 pp., (2011).

98. Ghisellini, G., Tavecchio, F., & Chiaberge, M., “Structured jets in TeV BL Lac objects and radiogalaxies. Implications for the observed properties”, Astronomy and Astrophysics, Volume 432, Issue 2, pp.401-410, (2005).

99. Chiaberge, M., Capetti, A., & Celotti, A., “The HST view of FR I radio galaxies: evidence for non-thermal nuclear sources”, The HST view of FR I radio galaxies: evidence for non-thermal nuclear sources, Astronomy and Astrophysics, v.349, p.77-87 (1999).

100. Pietsch, W., Bischoff, K., Boller, T., et al., “New active galactic nuclei detected in ROSAT All Sky Survey galaxies. I. Verification of selection strategy”, Astronomy and Astrophysics, v.333, p.48-62 (1998).

101. Saikia, D. J., Subrahmanya, C. R., Patnaik, A. R., et al., “Radio observations of the S0 galaxy NGC 1218 (3C 78)”, Monthly Notices of the Royal Astronomical Society (ISSN 0035-8711), vol. 219, p. 545-553, (1986).

102. Sparks, W. B., Golombek, D., Baum, S. A., et al., “Discovery of an Optical Synchrotron Jet in 3C 78”, Astrophysical Journal Letters v.450, p. L55, (1995).

103. Trussoni, E., Vagnetti, F., Massaglia, S., et al., “X-ray observations of low-power FR I radio galaxies”, Astronomy and Astrophysics, v.348, p.437-445 (1999).

104. Miller N. A., & et al., “Redshifts for a Sample of Radio-selected Poor Clusters”, The Astronomical Journal, Volume 123, Issue 6, pp. 3018-3040, (2002).

105. Fanti, C., Fanti, R., de Ruiter, H. R., & Parma, P., “VLA Observations of Low Luminosity Radio Galaxies. III. the A-Array Observations”, Astronomy and Astrophysics Supplement, Vol.65, NO. 1/JUL, P. 145, (1986).

106. Giovannini, G., Cotton, W. D., Feretti, L., Lara, L., & Venturi, T., “VLBI Observations of a Complete Sample of Radio Galaxies: 10 Years Later”, The Astrophysical Journal, Volume 552, Issue 2, pp. 508-526, (2001).

107. Hewitt, A., & Burbidge, G., “An optical catalog of extragalactic emission-line objects similar to quasi-stellar objects”, Astrophysical Journal Supplement Series (ISSN 0067-0049), vol. 75, p. 297-356, (1991).

108. Jorstad, S. G., Marscher, A. P., et al., “Polarimetric Observations of 15 Active Galactic Nuclei at High Frequencies: Jet Kinematics from Bimonthly Monitoring with the Very Long Baseline Array”, The Astronomical Journal, Volume 130, Issue 4, pp. 1418-1465, (2005).

109. Kadler, M., et al., “The Trails of Superluminal Jet Components in 3C 111”, The Astrophysical Journal, Volume 680, Issue 2, article id. 867-884, pp. (2008).

110. Eracleous M., Halpern J. P., “Accurate Redshifts and Classifications for 110 Radio-Loud Active Galactic Nuclei”, The Astrophysical Journal Supplement Series, Volume 150, Issue 1, pp. 181-186, (2004).

111. Danziger I. J., Fosbury R. A. E., Penston M. V., “Optical observations of Pictor A”, Monthly Notices of the Royal Astronomical Society, vol. 179, p. 41P-45P, (1977).

112. Perley R. A., Roeser H. J., Meisenheimer K., “The radiogalaxy PictorA -- a study with the VLA”, Astronomy and Astrophysics, v.328, p.12-32 (1997).

113. Hardcastle M. J., Croston J. H., “The Chandra view of extended X-ray emission from Pictor A”, Monthly Notices of the Royal Astronomical Society, Volume 363, Issue 2, pp. 649-660, (2005).

114. Gentry et al., “Optical Detection of the Pictor A Jet and Tidal Tail: Evidence against an IC/CMB jet”, The Astrophysical Journal, Volume 808, Issue 1, article id. 92, 10 pp. (2015).

115. Brown, A. M., & Adams, J., “Discovery of γ-ray emission from the broad-line radiogalaxy Pictor A”, Monthly Notices of the Royal Astronomical Society, Volume 421, Issue 3, pp. 2303-2309, (2012).

116. Hough, D. H., & Readhead, A. C. S., “A complete sample of double-lobed radio quasars for VLBI tests of source models - Definition and statistics”, Astronomical Journal (ISSN 0004-6256), vol. 98, p. 1208-1225, (1989).

117. Sambruna, R. M., Gambill, J. K., Maraschi, L., et al., “A Survey of Extended Radio Jets with Chandra and the Hubble Space Telescope”, The Astrophysical Journal, Volume 608, Issue 2, pp. 698-720, (2004).

118. Hough, D. H., Vermeulen, R. C., Readhead, A. C. S., et al., “Parsec-Scale Radio Structure and Broad Optical Emission Lines in a Complete Sample of 3CR Lobe-dominated Quasars”, The Astronomical Journal, Volume 123, Issue 3, pp. 1258-1287, (2002).

119. Aars, C. E.; Hough, D. H.; Yu, L. H.; Linick, J. P.; Beyer, P. J.; Vermeulen, R. C.; Readhead, A. C. S., “Optical Spectrophotometry of a Complete Sample of 3CR Lobe-dominated Quasars”, The Astronomical Journal, Volume 130, Issue 1, pp. 23-46, (2012).

120. Gilbert, G. M., Riley, J. M., Hardcastle, M. J., et al., “High-resolution observations of a complete sample of 27 FR II radio galaxies and quasars with $0.3 < z < 0.6$”, Monthly Notices of the Royal Astronomical Society, Volume 351, Issue 3, pp. 845-890, (2004).

121. Cheung, C. C., Wardle, J. F. C., & Chen, T., “Discovery of Optical Emission in the Hot Spots of Three 3CR Quasars: High-Energy Particle Acceleration in Powerful Radio Hot Spots”, The Astrophysical Journal, Volume 628, Issue 1, pp. 104-112, (2005).

122. Crawford, C. S., & Fabian, A. C., “Extended X-ray emission around four 3C quasars at $0.55 < z < 0.75$ observed with Chandra”, Monthly Notice of the Royal Astronomical Society, Volume 339, Issue 4, pp. 1163-1169, (2003).

123. Fanti, R., Fanti, C., et al., “On the nature of compact steep spectrum radio sources”, Astronomy and Astrophysics (ISSN 0004-6361), vol. 231, no. 2, p. 333-346, (1990).

124. Papageorgiou A., Cawthorne T. V., Stirling A, Gabuzda D, Polatidis A. G., “Space very long baseline interferometry observations of polarization in the jet of 3C380”, Monthly Notices of the Royal Astronomical Society, Volume 373, Issue 2, pp. 449-456, (2006).

125. O’Dea C. P., de Vries W., Biretta J. A., Baum S. A., “Hubble Space Telescope and VLA Observations of Two Optical Continuum Knots in the Jet of 3C 380”, The Astronomical Journal, Volume 117, Issue 3, pp. 1143-1150, (1999).

126. Kameno S., Inoue M., Fujisawa K., Shen Z.-Q., Wajima K., “First-Epoch VSOP Observation of 3C 380: Kinematics of the Parsec-Scale Jet”, Publications of the Astronomical Society of Japan, v.52, p.1045-L1053, (2000).

127. Junor, W., & et al., “VLA polarimetry of two extended radio galaxies”, Astronomy and Astrophysics Supplement, v.143, p.457-464, (2000).

128. Ekers R.D., Fanti R., Lari C., Parma R., “NGC326 - A radiogalaxy with a precessing beam”, Nature, vol. 276, p. 588-590, (1978).

129. Burbidge, G. R., & Burbidge, E. M., “Red-shifts of Quasi-stellar Objects and Related Extragalactic Systems”, Nature, volume 222, pp.735–741, 7351969, (1969).

130. Zhang et al, “Are there two engines at the center of 3C 286?”, Astronomy and Astrophysics (ISSN 0004-6361), vol. 287, no. 1, p. 32-37, (1994). The Astrophysical Journal Letters, Volume 824, Issue 2, article id. L20, 8 pp. (2016).

131. de Vries, W. H., O’Dea, C. P., Baum, S. A., et al., “Hubble Space Telescope Imaging of Compact Steep-Spectrum Radio Sources”, The Astrophysical Journal Supplement Series, Volume 110, Issue 2, pp. 191-211, (1997).

132. An, T., Hong, X.-Y., & Wang, W.-H., “The Kiloparsec-scale Structure of 3C 286”, Chinese Journal of Astronomy & Astrophysics, Vol. 4, p. 28-36, (2004).

133. Lüdke, E., Garrington, S. T., & Spencer, R. E., et al., “MERLIN polarization observations of compact steep-spectrum sources at 5 GHz”, Monthly Notices of the Royal Astronomical Society, Volume 299, Issue 2, pp. 467-478, (1998).

134. Cotton, W. D., Fanti, C., & Fanti, R., et al., “VLBA polarimetric observations of 3C 286 at 5 GHz”, Astronomy and Astrophysics, v.325, p.479-483, (2010).

135. Hynes R. I., Roche P., Haswell C. A., “XTE J1806-246”, IAU Circ., No. 6905, #2 Edited by Green, D. W. E., (1998).

136. Law-Green, J. D. B., Leahy, J. P., Alexander, P., et al., “VLA observations of DRAGNs in the 3CR and 6C/B2 '2-Jy' surveys”, Monthly Notices of the Royal Astronomical Society, Volume 274, Issue 3, pp. 939-963, (1995).

137. Yuan W. M., et al., “A Population of Radio-Loud Narrow-Line Seyfert 1 Galaxies with Blazar-Like Properties?”, The Astrophysical Journal, Volume 685, Issue 2, article id. 801-827, pp. (2008).

138. Dallacasa D., Stanghellini C., Centonza M., Fanti R., “High frequency peakers. I. The bright sample”, Astronomy and Astrophysics, v.363, p.887-900 (2000).

139. Orienti M., D’Ammando F., Giroletti M., “High resolution radio observations of gamma-ray emitting Narrow-Line Seyfert 1s”, eprint arXiv:1205.0402, (2012).

140. Ackermann, M., Anantua, R., & et al., “Minute-timescale >100 MeV γ-Ray Variability during the Giant Outburst of Quasar 3C 279 Observed by Fermi-LAT in 2015 June”, The Astrophysical Journal Letters, Volume 824, Issue 2, article id. L20, 8 pp. (2016).

140. Drinkwater, M. J., Webster, R. L., Francis, P. J., et al., “The Parkes Half-Jansky Flat-Spectrum Sample”, Monthly Notices of the Royal Astronomical Society, Volume 284, Issue 1, pp. 85-125, (1997).

141. Oshlack, A., Webster, R., & Whiting, M., “A Very Radio Loud Narrow-Line Seyfert 1: PKS 2004-447”, The Astrophysical Journal, Volume 558, Issue 2, pp. 578-582, (2001).

142. Massaro, E., Tramacere, A., Perri, M., Giommi, P., & Tosti, G., “Log-parabolic spectra and particle acceleration in blazars. III. SSC emission in the TeV band from Mkn501”, Astronomy and Astrophysics, Volume 448, Issue 3, pp.861-871, (2006).

143. Nolan, P. L., Abdo, A. A., Ackermann, M., et al., “Fermi Large Area Telescope Second Source Catalog”, The Astrophysical Journal Supplement, Volume 199, Issue 2, article id. 31, 46 pp. (2012).

144. Ghisellini, G., Maraschi, L., & Tavecchio, F., “The Fermi blazars' divide”, Monthly Notices of the Royal Astronomical Society: Letters, Volume 396, Issue 1, pp. L105-L109, (2009).

145. Bonnoli, G., Ghisellini, G., Foschini, L., Tavecchio, F., & Ghirlanda, G., “The γ-ray brightest days of the blazar 3C 454.3”, Monthly Notices of the Royal Astronomical Society, Volume 410, Issue 1, pp. 368-380, (2011).

146. Dyrda, M.; Wierzcholska, A.; Hervet, O. et al., “Discovery of VHE gamma-rays from the radiogalaxy PKS 0625-354 with H.E.S.S”, In Proceedings of the 34th International Cosmic Ray Conference (ICRC2015), eprint arXiv:1509.06851, (2015)

147. Baghmanyan, V., Tumanyan, M., Sahakyan, N., & Vardanyan, Y., "High-Energy γ–ray Emission from PKS 0625-35", Astrophysics, in press.

148. Abdo, A. A., Ackermann, M., & et al., "Fermi/Large Area Telescope Discovery of Gamma-Ray Emission from a Relativistic Jet in the Narrow-Line Quasar PMN J0948+0022", The Astrophysical Journal, Volume 699, Issue 2, pp. 976-984 (2009).

149. Baghmanyan, V. & Sahakyan, N., "X-ray and γ-ray emissions from NLSy1 galaxies", International Journal of Modern Physics D, Volume 27, 1844001, 9 pp., (2018).

150. Abramowski, A., Acero, F., & et al., "The 2010 Very High Energy γ-Ray Flare and 10 Years of Multi-wavelength Observations of M 87", The Astrophysical Journal, Volume 746, Issue 2, article id. 151, 18 pp. (2012).

151. Aharonian, F., Akhperjanian, A. G., & et al., "Fast Variability of Tera-Electron Volt γ Rays from the Radiogalaxy M87", Science, Volume 314, Issue 5804, pp. 1424-1427 (2006).

152. Pedlar, A., Ghataure, H. S. et al., "The Radio Structure of NGC1275", Monthly Notices of the Royal Astronomical Society, Vol. 246, NO. 3, P. 477, (1990).

153. Asada, K., Kameno, S., et al., "The Expanding Radio Lobe of 3C 84 Revealed by VSOP Observations", Publications of the Astronomical Society of Japan, Vol.58, No.2, pp. 261-270, (2006).

154. Churazov, E., Forman, W. et al., H., "XMM-Newton Observations of the Perseus Cluster. I. The Temperature and Surface Brightness Structure", The Astrophysical Journal, Volume 590, Issue 1, pp. 225-237, (2003).

155. Brown, A. M. & Adams, J., "High-energy γ-ray properties of the Fanaroff-Riley type I radiogalaxy NGC 1275", Monthly Notices of the Royal Astronomical Society, Volume 413, Issue 4, pp. 2785-2790, (2011).

156. Aleksi′c, J., Alvarez, E. A. et al., "Detection of very-high energy γ-ray emission from NGC 1275 by the MAGIC telescopes", Astronomy & Astrophysics, Volume 539, id.L2, 4 pp., (2012).

157. Aleksi′c, J., Alvarez, E. A. et al., “Contemporaneous observations of the radiogalaxy NGC 1275 from radio to very high energy γ-rays”, Astronomy & Astrophysics, Volume 564, id.A5, 13 pp. (2014).

158. Walker, R. C., Romney, J. D. and Benson, J. M., “Detection of a VLBI counterjet in NGC 1275: A possible probe of the parsec-scale accretion region”, The Astrophysical Journal, Part 2 - Letters, vol. 430, no. 1, p. L45-L48, (1994).

159. Baghmanyan, V., “Gamma-ray variability NGC 1275”, AIP Conference Proceedings, Volume 1792, Issue 1, id.050007 (2017).

160. Pivato, G., Buson, S., “Fermi LAT detection of increasing gamma-ray activity from NGC 1275 and B3 0908+416B”, The Astronomer's Telegram, No.8219, (2015).

161. Mirzoyan, R. et al., “MAGIC detection of a giant flaring activity from NGC 1275 at very-high-energy gamma rays”, The Astronomer's Telegram, No. 9929, (2017).

162. Lucarelli, F., Pittori, C. et al., “AGILE confirmation of enhanced gamma-ray activity from NGC 1275”, The Astronomer's Telegram, No. 9934, (2017).

163. Mac′ias-Ram′irez, O., Gordon, C., Brown, A. M., et al., “Evaluating the gamma-ray evidence for self-annihilating dark matter from the Virgo cluster”, Physical Review D, vol. 86, Issue 7, id. 076004, (2012).

164. Aleksi′c, J., et al., “Rapid and multiband variability of the TeV bright active nucleus of the galaxy IC 310”, Astronomy & Astrophysics, Volume 563, id. A91, 9 pp., (2014).

165. Kirk, J., Rieger, F., and Mastichiadis, A., “Particle acceleration and synchrotron emission in blazar jets”, Astronomy and Astrophysics, v.333, p.452-458 (1998).

166. Li, H., & Kusunose, M., “Temporal and Spectral Variabilities of High-Energy Emission from Blazars Using Synchrotron Self-Compton Models”, The Astrophysical Journal, Volume 536, Issue 2, pp. 729-741, (2000).

168. Giannios, D., Uzdensky, D., and Begelman, M., “Fast TeV variability in blazars: jets in a jet”, Monthly Notices of the Royal Astronomical Society: Letters, Volume 395, Issue 1, pp. L29-L33, (2009).

169. Giannios D., Uzdensky D. A., Begelman M. C., “Fast TeV variability from misaligned minijets in the jet of M87”, Monthly Notices of the Royal Astronomical Society, Volume 402, Issue 3, pp. 1649-1656, (2010).

170. Beilicke, M. for the H.E.S.S. collab., “Observation of the Giant Radiogalaxy M87 at TeV Energies with H.E.S.S.”, Proceedings of the 22nd Texas Symposium on Relativistic Astrophysics at Stanford, Stanford California, p.650-653, (2004).

171. Mariotti M. et al., “Discovery of Very High Energy Gamma-Ray Emission from NGC1275 by MAGIC”, The Astronomer's Telegram, No.2916, (2010).

172. Ekers et al., “A complete sample of radio galaxies. I - The radio data”, Monthly Notices of the Royal Astronomical Society (ISSN 0035-8711), vol. 236, p. 737-777, (1989).

173. Bloom, S. D., & Marscher, A. P., “An Analysis of the Synchrotron Self-Compton Model for the Multi--Wave Band Spectra of Blazars”, Astrophysical Journal v.461, p.657, (1996).

174. Ghisellini, G., Maraschi, L., Treves, A., “Inhomogeneous synchrotron-self-Compton models and the problem of relativistic beaming of BL Lac objects”, Astronomy and Astrophysics (ISSN 0004-6361), vol. 146, no. 2, p. 204-212, (1985).

175. Inoue, S., & Takahara, F., “Electron Acceleration and Gamma-Ray Emission from Blazars”, Astrophysical Journal v.463, p.555, (1996).

176. Zabalza, V. 2015, “Naima: a Python package for inference of particle distribution properties from nonthermal spectra”, Proceedings of the 34th International Cosmic Ray Conference (ICRC2015), (2015).

177. Aharonian, F. A., Kelner, S. R., & Prosekin, A. Y., “Angular, spectral, and time distributions of highest energy protons and associated secondary gamma rays and neutrinos propagating through extragalactic magnetic and radiation fields”, Physical Review D, vol. 82, Issue 4, id. 043002, (2010).

178. Aharonian F. A., Atoyan A. M., “Compton scattering of relativistic electrons in compact X-ray sources”, Astrophysics and Space Science, vol. 79, no. 2, p. 321-336, (1981).

179. Mingo, B., Hardcastle, M. J., Croston, J. H., et al., “An X-ray survey of the 2 Jy sample–I. Is there an accretion mode dichotomy in radio-loud AGN?”, Monthly Notices of the Royal Astronomical Society, Volume 440, Issue 1, Pages 269–297, (2014).

180. Zhou, H., et al., “A NARROW-LINE SEYFERT 1–BLAZAR COMPOSITE NUCLEUS IN 2MASX J03243410”, The Astrophysical Journal, 658:L13–L16, (2007)

181. Angelakis, E., Fuhrmann, L., et al., “Radio jet emission from GeV-emitting narrow-line Seyfert 1 galaxies”, Astronomy & Astrophysics, Volume 575, id. A55, 22 pp., (2015).

182. Wajima, K., Fujisawa, K., Hayashida, M., et al., “Short-term Radio Variability and Parsec-scale Structure in a Gamma-Ray Narrow-line Seyfert 1 Galaxy 1H 0323+342”, The Astrophysical Journal, Volume 781, Issue 2, article id. 75, 12 pp. (2014).

183. Fuhrmann L., et al., “Inner jet kinematics and the viewing angle towards the γ-ray narrow-line Seyfert 1 galaxy 1H 0323+342”, Research in Astronomy and Astrophysics, Volume 16, Issue 11, article id. 176 (2006).

184. Foschini L. et al., “The first gamma-ray outburst of a narrow-line Seyfert 1 galaxy: the case of PMN J0948+0022 in 2010 July”, Monthly Notices of the Royal Astronomical Society, Volume 413, Issue 3, pp. 1671-1677, (2011).

185. Giroletti, M., Paragi, Z., Bignall, H., et al., “Global e-VLBI observations of the gamma-ray narrow line Seyfert 1 PMN J0948+0022”, Astronomy & Astrophysics, Volume 528, id. L11, 4 pp, (2011).

186. Zhou, H.-Y., & et al., “SDSS J094857.3+002225: A VERY RADIO LOUD, NARROW-LINE QUASAR WITH RELATIVISTIC JETS?”, The Astrophysical Journal, 584:147–152, (2003)

187. Foschini, L., Angelakis, E., Fuhrmann, L., et al., “Radio-to-γ-ray monitoring of the narrow-line Seyfert 1 galaxy PMN J0948+0022 from 2008 to 2011”, Astronomy & Astrophysics, Volume 548, id.A106, 14 pp, (2012).

188. Zhang, J., Zhang, H., Zhu, Y., & al., “Multiple-wavelength Variability and Quasi-periodic Oscillation of PMN J0948+0022”, The Astrophysical Journal, Volume 849, Issue 1, article id. 42, 7 pp. (2017).

189. D'Ammando F., et al., "The most powerful flaring activity from the NLSy1 PMN J0948+0022", Monthly Notices of the Royal Astronomical Society, Volume 446, Issue 3, p.2456-2467, (2015).

190. Ghisellini G. and F. Tavecchio, "Fermi/LAT broad emission line blazars", Monthly Notices of the Royal Astronomical Society, Volume 448, Issue 2, p.1060-1077, (2015).